STUDIES OF LOW CYCLE FATIGUE AND CREEP-FATIGUE-OXIDATION INTERACTION OF MATERIAL AND CONSTITUTIVE MODELING

A Thesis Submitted
In Partial Fulfilment of the Requirements
for the Degree of

DOCTOR OF PHILOSOPHY

by
NEHA MEHANI
(2017MSZ0002)



DEPARTMENT OF MECHANICAL ENGINEERING INDIAN INSTITUTE OF TECHNOLOGY ROPAR

June, 2025

Neha Mehani: Studies of low cycle fatigue and creep-fatigue oxidation interaction of material and constitutive modeling
Copyright © 2024, by Indian Institute of Technology Ropar
All Rights Reserved
ii

This thesis is dedicated to

Gurbaksh Lal Arora

Your endless love, trust, and genuine smile motivate and encourage me. I miss you a lot on the day, and I hope I made you proud. Please always be there with me, forgive all my mistakes, and show me the right path.

Rajni Arora

Luck is bestowed upon me, as rightly said by someone, to have all the love and support of 3 mothers.

Sumit Arora

Getting to know you as a person and husband is the best gift I can ever ask for. Thank you for always being there, listening to my endless ranting, and still supporting me

D. P. Mehani

I just wanted to thank you for working too hard, always believing and supporting me, forgiving me, and being there whenever needed. Please be there like always.

Naresh Mehani

I love you a lot Ma, and admire you more for being the amazing woman that you are. Your teachings inspire me. I always want to be like you and Di so always be there to hold my hand and show me the right path.

Shweta Mehani, Saurabh Awasthi, and my little niece and nephew

Sibling cum friend, many have, but you have always acted like a small mother. Thank you for being the bestest of best and so amazing Di and JiJu for being there and guiding me the right way to do everything. My little chutkus to bring smiles on tough days.



INDIAN INSTITUTE OF TECHNOLOGY ROPAR

CERTIFICATE

This is to certify that the thesis entitled "Studies of low cycle fatigue and creep-fatigue oxidation interaction of material and constitutive modeling" submitted by Neha Mehani to the Department of Mechanical Engineering, Indian Institute of Technology Ropar for the award of the degree of Doctor of Philosophy is a record of bona fide research work carried out by him under our supervision.

The thesis has reached the standards fulfilling the requirements of the regulations relating to the degree. The work contained in this thesis has not been submitted to any other university or institute for the award of any degree or diploma.

Dr. Samir Chandra Roy

Assistant Professor,

Department of Mechanical Engineering

Indian Institute of Technology Ropar, India

Rupnagar, Punjab 140001, India

Date:



INDIAN INSTITUTE OF TECHNOLOGY ROPAR

DECLARATION OF ORIGINALITY

I, Neha Mehani, hereby declare that the work presented in the thesis, entitled "Studies of low cycle fatigue and creep-fatigue-oxidation interaction of material and constitutive modeling" in partial fulfillment of the requirements for the award of the degree of Doctor of Philosophy and submitted to the Department of Mechanical Engineering, Indian Institute of Technology Ropar is an authentic record of my research work carried out by me under the supervision of Dr. Samir Chandra Roy.

The matter presented in this thesis has not been submitted elsewhere for the award of any other degree of this Institute or any other University/Institute.

Date: NEHA MEHANI

(Signature of the candidate)

This is to certify that the above statement made by the candidate is correct to the best of my knowledge.

Dr. SAMIR CHANDRA ROY

Supervisor

Department of Mechanical Engineering

Indian Institute of Technology Ropar

Rupnagar, Punjab 140001, India

ACKNOWLEDGEMENTS

I would like to express my deepest gratitude to my supervisor, Dr. Samir Chandra Roy, for his invaluable guidance and encouragement throughout this research work. Despite his busy schedule, I thank him for bestowing overwhelming trust, cultivating independent thinking, and having time for those long research-related discussions whenever needed. His work ethics, sincerity, and humility will always be a source of inspiration throughout my life.

I warmly thank my Doctoral Committee members, Dr. Dhiraj K. Mahajan, Dr. Amar Nath Chowdhury, Dr. Ravi Mohan Prasad, and, Dr. Navin Kumar for continuously monitoring the progress of work and providing valuable suggestions and encouragement. I am very thankful to the Indian Institute of Technology Ropar for providing the necessary infrastructure and financial support. I am also thankful to the Ministry of Human Resources and Development, Government of India, for providing the scholarship to conduct this research work. I also would like to express my gratitude to Mr. J. Veerababu, Scientific officer, and Dr. A. Nagesh, Head, Fatigue Studies Section, Indira Gandhi Centre for Atomic Research, for allowing us to conduct the LCF tests on 304L SS.

I thank my colleagues, who have supported my work and stimulated my interest in research in various ways: Dr. Sanjeev Singh Yadav, Himanshu Markanday, Rajat Dhiman, Subha Nath, Nikhil Suman, Manish Kumar, and Ashish Singh. I would like to thank my friends Ankit Chauhan, Vansha Kher, Nahida Rasool, Aman Arora, Ridhima Verma, Radhika Raina, Jitendra, Vishal Aggarwal, Ajay goyal, and Tushita Rohilla for their constant support and for making my time at IIT Ropar a truly memorable experience.

Finally, my deepest gratitude goes to my family for their constant love, patience, and support through all these years.

The structural materials used in power plants can exhibit initial hardening/softening, prolonged softening/ hardening, saturation, and secondary hardening behavior before the final fracture under cyclic loading. The cyclic deformation of materials also causes the hysteresis loop to show Masing/non-Masing behavior. In the open literature, the non-Masing behavior is recently classified into Type-I (only isotropic stress changes with strain amplitude) and Type-II (both isotropic stress and strain hardening rate changes with strain amplitude). Constitutive models in the literature deal with material fatigue behavior without regard for the Masing/non-Masing behavior. Thus, the constitutive modeling of the above four phenomena with accurate prediction of Masing, non-Masing Type-I, and Type-II is essential for successfully designing and developing components and structures. The constitutive models available in the open literature are primarily developed by modifying the isotropic and kinematic hardening laws. The classical and modified models developed to date cannot predict the material's behavior exhibiting significant secondary hardening, as shown by some structural steels undergoing low cycle fatigue loading. Moreover, no article in the literature has demonstrated (or validated) any constitutive model for simulating materials' Type-I and Type-II non-Masing behavior.

A modified constitutive model is proposed to consider all the cyclic features mentioned above as exhibited by the material under cyclic loading. A new non-dimensional function, ζ (representing cyclic hardening or cyclic softening rate), is introduced in the isotropic and kinematic hardening equations to account for the significant change in softening and hardening behavior with strain amplitude through maximum plastic strain range memory (q). Moreover, to take into account the Masing and non-Masing behavior of Type-I and Type-II, another function, φ_{KH} (representing the dependence of maximum back stress on strain amplitude), is introduced.

The components of power plants undergo creep-fatigue loading at high temperature every day, causing the material to undergo a combination of creep, fatigue, and oxidation damage. In open literature, many methods are available to predict the life of the material. Most of these methods predict the life of material considering creep and fatigue loading without any consideration of oxidation damage. Moreover, most of these methods use data from pure fatigue, creep-fatigue, and pure creep tests. To overcome

these problems, the tensile hysteresis strain energy density method (THSED) is investigated, and a modified THSED method is proposed that takes into account the parameter γ_d that depends on oxidation damage, temperature, strain rate of cyclic loading, and hold time.

Further, the proposed modified isotropic and kinematic hardening laws are coupled with the unified Chaboche viscoplastic flow rule to predict the time-dependent creep effect. The developed viscoplasticity model further takes into account the complex microstructural degradation effect due to a synergistic combination of creep, fatigue, and oxidation through the incremental scalar damage lifetime rule, which can predict the component's mechanical state and the material's behavior under creep-fatigue loading.

The proposed constitutive models are implemented in ABAQUS as user subroutines (UMAT) for simulating the LCF behavior of 304L SS and 321 SS materials and the creep-fatigue behavior of 304L SS material under peak tensile and peak compressive hold for 60sec. The excellent agreement between experimental data and simulated results suggests that the proposed model works well in predicting the cyclic deformation behavior of the materials.

Keywords: Constitutive modeling, Low cycle fatigue, Secondary hardening, Non-Masing: Type-I and Type-II, Creep-fatigue interaction, Creep-fatigue-oxidation interaction.

TABLE OF CONTENTS

(CERTIFICATE	v
Ι	DECLARATION OF ORIGINALITY	vii
A	ACKNOWLEDGEMENTS	ix
A	ABSTRACT	xi
7	TABLE OF CONTENTS	xiii
I	IST OF TABLES	xvii
I	IST OF FIGURES	xix
S	SYMBOL AND ABBREVIATIONS	xxv
Ch	apter 1: Introduction	1
1	.1. Background	1
1	.2. Motivation of the work	2
1	.3. Objectives	5
1	.4. Organization of the thesis	6
Ch	apter 2: Literature review	11
2	2.1. Introduction	11
2	2.2. Basic concepts of modeling	16
	2.2.1. Yield criterion	16
	2.2.2. Flow rule	17
	2.2.3. Consistency condition	17
2	2.3. Yield surface expansion and translation	18
	2.3.1. Yield surface expansion (isotropic hardening)	18
	2.3.2. Translation of yield surface (kinematic hardening)	19
	2.3.3. Expansion and translation of yield surface (combined isotropic and kinematic	
	hardening behavior)	20
	2.3.4. Time-dependent cyclic plasticity	21
	2.3.4.1. Unified model	22
	2.3.4.2. Non-unified model	22

2.4. Continuum damage mechanics-based model	23
2.4.1. Damage models	24
2.4.1.1. Empirical models	24
2.4.1.2. Continuum damage models	26
2.5. Numerical implementation of the constitutive model	28
Chapter 3: Modified isotropic and kinematic hardening equation	ns for 304L SS
under low cycle fatigue.	33
3.1. Introduction	33
3.2. Cyclic behavior	36
3.2.1. Cyclic peak stress	36
3.2.2. Microstructural deformation	38
3.3. Modified constitutive laws	38
3.3.1. Isotropic hardening	38
3.3.2. Kinematic hardening	42
3.3.3. Plastic strain range memory effect	44
3.4. Material parameter identification	46
3.4.1. Isotropic hardening parameters	47
3.4.2. Kinematic hardening parameters	48
3.5. Simulation details	49
3.6. Results and discussion	50
3.6.1. Variation in cyclic peak stress	50
3.6.2. Hysteresis loop shape	51
3.6.3. Fatigue life prediction	52
3.7. Conclusions	54
Chapter 4: Type-I and Type-II non-Masing behaviors of material	ls under low
cycle fatigue: constitutive modeling and simulation	55
4.1. Introduction	55
4.2. Experimental details	62
4.2.1. Cyclic peak stress variation	64
4.2.2. Yield surface expansion and translation with cycling	65
4.2.3. Strain range dependence behavior	67
4.2.4. Transient back stress effect	69
4.3. Constitutive model	70

4.3.1. Modeling yield surface expansion and translation with cycling	70
4.3.2. Modeling of strain range dependence behavior	71
4.3.3. Modeling of transient back stress effect	73
4.4. Identification and calibration of material parameters	75
4.5. Comparison of experimental and simulation results	78
4.5.1. Accuracy of the model	79
4.5.1.1. Cyclic peak stress	79
4.5.1.2. Hysteresis loop shape	79
4.5.2. Prediction capability of the model	84
4.6. Conclusions	87
Chapter 5: Quantification of the creep, fatigue, and oxidation dame	ige and life
prediction	89
5.1. Introduction	89
5.2. Life prediction methods	93
5.2.1. THSED method for axial loading	93
5.2.2. THSED method extended to H-CFI	95
5.2.3. Modified SEDE method	96
5.3. Oxidation damage above	97
5.3.1. Proposed damage index	97
5.4. Results and discussion	99
5.4.1. Oxidation damage model	99
5.4.2. Implementation of modified THSED model and lifetime prediction	101
5.4.3. Life prediction factor	107
5.5. Conclusion	107
Chapter 6: Continuum damage mechanics based unified model for	creep-
fatigue-oxidation	109
6.1. Introduction	109
6.2. Experimental details	111
6.2.1. Cyclic peak stress variation	111
6.2.2. Yield surface expansion and translation with cycling, hold time and hold	position 112
6.2.3. Stress relaxation with cycling	113
6.2.4. Damage accumulation and creep-fatigue life	114
6.3. Damage coupled unified constitutive model	116

6.3.1. Main equations	116
6.3.2. Modeling yield surface expansion and translation with cycling	117
6.3.3. Modification in kinematic hardening rule due to variation in stress relaxat	ion behavior
with cycling	117
6.3.4. Damage evolution	118
6.4. Identification and calibration of material parameters	119
6.5. Comparison of experimental and simulation results	121
6.5.1. Validation of model accuracy	122
6.5.2. Prediction capability of the model	123
6.6. Conclusions	124
Chapter 7: Conclusions and scope of future work	127
7.1. Conclusions	127
7.2. Future scope	128
Chapter 8: Publications	131
Chapter 9: References	133

LIST OF TABLES

Table 2.1 Chronological development of damage models for creep-fatigue interaction	1.
2.	4
Table 2.2 Continuum damage mechanics models for creep-fatigue interaction. 2	7
Table 3.1. Material parameters for 304L SS	9
Table 4.1 Cyclic behavior of some materials used in nuclear and thermal power plant.	S
and their constitutive model. 5	7
Table 4.2. The chemical composition (in % wt.) of the materials.6.	3
Table 4.3. Fatigue life of the materials tested at different strain amplitudes.6-	4
Table 4.4. Summarized framework of the equations used in the modified constitutive	e
model. 7-	4
Table 4.5. Material parameters for 304L SS and 321 SS	8
Table 5.1: Estimated values of material parameters for damage index, Eq. (5.24)	9
Table 5.2: Estimated parameters of the oxidation damage equations and comparison of	f
parameter γd 100	0
Table 5.3: Creep-fatigue data of the materials10-	4
Table 5.4: Parameters used for the THSED method and modified THSED method 10-	4
Table 5.5: Parameters used for the THSED method and modified THSED method 10-	4
Table 5.6: Parameters for modified SEDE method10.	5
Table 5.7: Parameters for modified SEDE method 100	6
Table 6.1 Material parameters required for creep-fatigue simulations for 304L SS a	ıt
650° C.	1

LIST OF FIGURES

Figure 1.1. (a) Electricity demand in (kW) with time period of day (b)	Reactor
operational mode with time in (hrs) [5].	2
Figure 1.2. Cyclic peak stress variation with cycle number for different materi	als (a, b)
ferritic -martensitic steel [10,11] (c, d) Ni-based superalloy [12,	13] (e, f)
Austenitic steel.	3
Figure 1.3. Stress-strain loops at material's half-life showing (a) Masing [13]	(b) Non-
Masing Type-I [16] (c) Non-Masing Type-II behavior [16].	4
Figure 2.1. Classification of the cyclic plasticity constitutive models [18,33].	12
Figure 2.2 Expansion of yield surface under tensile loading and corresponding	ıg stress-
strain curve [80].	19
Figure 2.3 Shifting of yield surface and the resulting non-linear kinematic h	ardening
stress-strain curve [80].	20
Figure 2.4 Combined non-linear kinematic and isotropic hardening [80].	21
Figure 2.5 Flowchart of radial-return implicit integration scheme for implen	nentation
of $UMAT$	29
Figure. 3.1. Peak stress variation with cycle number.	37
Figure. 3.2. Translated stress vs. plastic strain loops of 304L at half-life to n	natch the
linear elastic portions.	38
Figure. 3.3. Peak stress vs. accumulated plastic strain curves.	39
Figure. 3.4. Peak effective stress vs. accumulated plastic strain curves.	41
Figure. 3.5. Variation of ϕ with accumulated plastic strain is fitted with Eq. ((3.10) (a)
for material 304L SS (b) for 316H (data were extracted from So	ong et al.
[13]).	43
Figure. 3.6. Variation of φ with accumulated plastic strain is fitted with Eq ((3.11) (a)
for material 304L SS (b) for 316H (data were extracted from So	ong et al.
[13]).	44
Figure. 3.7. Variation of ζ with maximum plastic strain range (%).	45
Figure. 3.8. Variation of φ KH with maximum plastic strain range (%).	46
Figure. 3.9. Schematic diagram showing the determination of elastic modulus	s E, yield
stress ($\sigma y0$), peak effective stress ($\sigma 0$) and maximum back stress	(xmax).
	47

Figure. 3.10. Determination of isotropic hardening material parameters for different
strain amplitudes by fitting Eq. (3.9).
Figure. 3.11. The 3D model used for the simulation.
Figure. 3.12. Comparison of peak stress variation with cycle number. 50
Figure. 3.13. Comparison of experimental and simulated hysteresis loops for different
strain amplitudes: (a) $\pm 0.4\%$, (b) $\pm 0.6\%$, (c) $\pm 0.8\%$, and (d) $\pm 1.0\%$. The
hysteresis loops for the second cycle (\circ), initial hardening region (\Box),
softening (∇), saturation (\Diamond), and secondary hardening (\times) regions are
shown. The actual cycle numbers are highlighted in the figures. 51
Figure. 3.14. Comparison of the cyclic plastic strain energy densities (CPSEDs) of the
experimental and simulated hysteresis loops for strain amplitudes of (a)
$\pm 0.4\%$, (b) $\pm 0.6\%$, (c) $\pm 0.8\%$, and (d) $\pm 1.0\%$. The error percentages are
shown above the bars. 52
Figure. 3.15. Comparison of half-life hysteresis loops of different strain amplitudes. 53
Figure. 3.16. Experimental cyclic plastic strain energy density (CPSED) is estimated
from the data in Figure. 3.15 is plotted with fatigue life (Nf, exp). 53
Figure. 3.17. Comparison of experimental and simulated fatigue lives. 54
Figure 4.1. LCF test specimens: (a) 304L SS [126] and (b) 321 SS. (All dimensions are
63
Figure. 4.2. Peak stress variation with number of cycles for (a) 304L SS and (b) 321SS.
65
Figure. 4.3. Linear stress variation in different cyclic hardening/softening regions of
(a) 304L SS and (b) 321 SS, highlighted with translated (at origin) hysteresis
loops from different regions. 65
Figure. 4.4. Peak effective stress variation with accumulated plastic strain (a) 304L SS
(b) 321 SS. 66
Figure. 4.5. Peak back stress vs. accumulated plastic strain for (a) 304L SS and (b) 321
SS at different strain amplitudes. 67
Figure. 4.6. Variation of φ mod with accumulated plastic strain (p) at different strain
amplitudes for (a) 304L SS and (b) 321 SS. 67
Figure. 4.7. Translated stress-strain loops at common tensile yield point (a) 304L SS
(b) 321SS at half-life.
Figure. 4.8. Comparison of the monotonic tensile curve and shifted reverse stress-strain
(%) curves for (a) 304L SS and (b) 321 SS.

Figure. 4.9. Back stress vs. plastic strain (%) curve for (a) 304L SS and (b) 321	SS
obtained from the loading branches of the 2^{nd} cycle	70
Figure. 4.10. Variation of ζS with maximum plastic strain range (%) for (a) 304L	SS
and (b) 321 SS	72
Figure. 4.11 Variation of ζH with maximum plastic strain range (%) for (a) 304L	SS
and (b) 321 SS	72
Figure. 4.12. Variation of φKH with maximum plastic strain range (%) (a) 304L SS	(b)
321 SS.	74
Figure. 4.13. Flowchart for identification and calibration of material parameters	77
Figure. 4.14. 3D model used for the simulation. R denotes rotational degrees	of
freedom, and U denotes displacement.	79
Figure. 4.15. Comparison of peak stress variation with cycle number obtained by	the
proposed model for (a) 304L SS and (b) 321 SS.	79
Figure. 4.16. Comparison of half-life hysteresis loops obtained at different str	ain
amplitudes for (a) 304L SS and (b) 321 SS.	80
Figure. 4.17. Type-I non-Masing behavior of 304L SS at 7% life fraction.	80
Figure. 4.18. Comparison of experimental and simulated hysteresis loops for 304L	SS
$at\pm1.0\%$ strain amplitude.	81
Figure. 4.19. Comparison of experimental and simulated hysteresis loops for 304L	SS
at $\pm 0.4\%$ strain amplitude.	82
Figure. 4.20. Comparison of experimental and simulated hysteresis loops for 321 SS	s at
$\pm 0.8\%$ strain amplitude.	83
Figure. 4.21. Comparison of experimental and simulated hysteresis loops for 321 SS	s at
$\pm 0.4\%$ strain amplitude.	84
Figure. 4.22. Comparison of simulated and experimental results for cyclic peak str	ess
variation at strain amplitudes of $\pm 0.25\%$ for 304L SS and $\pm 0.45\%$ for $\pm 0.45\%$	321
SS.	85
Figure. 4.23. Comparison of experimental and simulated hysteresis loops for 304L	SS
$at \pm 0.25\%$ strain amplitude.	86
Figure. 4.24. Comparison of experimental and simulated hysteresis loops for 321 SS	s at
$\pm 0.45\%$ strain amplitude.	87
Figure 5.1. Shaded area represents THSED for U-CFI loading (a) tension hold and	(b)
compression hold	Q_{Δ}

Figure 5.2. Shaded area represents THSED for H-CFI loading (a) tension stress hold
and (b) compression stress hold.
Figure 5.3. Oxygen content (wt.%) variation with depth (mm) [221,229–231] (Note: for
P91 steel, to determine the material parameters (D' and A), the saturated
value of oxygen concentration is assumed to be 80% at the surface). 98
Figure 5.4. Experimental creep-fatigue life Nexp vs. Δwt 103
Figure 5.5. Comparison between experimental and predicted life of austenitic steels:
(a) 304SS and (b) 304L SS.
Figure 5.6. Comparison between experimental and predicted life of ferritic-martensitic
steels: (a) Modified 9Cr-1Mo steel and (b) P92 steel.
Figure 5.7. Life prediction factor for different materials plotted with (a) strain
amplitude (%) and (b) hold time (hrs.).
Figure. 6.1 Creep-fatigue test specimen.
Figure. 6.2 Peak stress variation with the number of cycles normalized by failure cycles
112
Figure. 6.3 (a) Peak effective stress variation with accumulated inelastic strain (p) (b)
Variation of φ mod with accumulated inelastic strain (p) at different hold
times and hold position.
Figure. 6.4 Stress relaxation with cycle number 114
Figure 6.5 Creep-fatigue life with hold time
Figure 6.6 Accumulated tensile strain energy density (wtotal) with maximum plastic
strain range (%).
Figure 6.7 Stress relaxation vs. accumulated inelastic strain
Figure 6.8 Damage evolution with normalized cycle number 119
Figure 6.9. Schematic diagram showing the determination of elastic modulus E, yield
stress ($\sigma y0$), peak effective stress ($\sigma 0$), peak back stress ($xmax$), and
viscous stress (σv) . 120
Figure 6.10 3-D model for creep-fatigue simulation. R denotes rotational degrees of
freedom, and U denotes displacement.
Figure 6.11. Comparison of experimental and simulated results (a) Peak stress
variation with normalized cycle number (b) Stress relaxation with hold time
for 2 nd and half-life cycle

Figure 6.12. Comparison of experimental and simulated hysteresis loops	of 304L SS
under creep-fatigue interaction loading with peak tensile hold	l of 60 sec.
Plotted for (a) 5^{th} cycle and (b) 500^{th} cycle.	123
Figure 6.13. Comparison of experimental and simulated results: (a) Peak	stress with
cycle number (b) Stress relaxation with hold time for 2 nd and ha	ılf-life cycle
	124
Figure 6.14. Comparison of experimental and simulated hysteresis loops for	· 304L SS at
peak compression hold 60sec	124

SYMBOL AND ABBREVIATIONS

Symbol	Description
p	Accumulated effective plastic strain
$a_2 - a_9$	Additional kinematic hardening parameters in the proposed model
Q_1 , b_1 , a_1	Additional isotropic hardening parameters in the proposed model
Δp_{PSH}	Accumulated plastic strain in the secondary hardening region
Δp_S	Accumulated plastic strain in the softening region
x	Absolute value of x
α , q	Center and radius of the memory surface in plastic strain space
$\Delta\sigma_{PSH}$	Change in peak stress in the secondary hardening region
$\Delta\sigma_{PS}$	Change in peak stress in the softening region
D_c	Creep damage
w_f	Creep fracture strain energy density
$arepsilon_c$	Creep strain
w	Creep strain energy density rate
σ_{min}	Compressive peak stress
n'	Cyclic hardening exponent
F	Control function of the plastic strain memory (represents hypersphere)
D_{cfo}	Damage due to creep-fatigue and oxidation
D_{index}	Damage index
β	Damage index constant
$\int DE$	Dissipated hysteretic energy
x_i	Distance of any point in the material from the oxidized surface
D	Damage variable in continuum damage mechanics theory

σ_e	Effective stress or Von-Mises stress or equivalent stress
ψ̈́	Effective plastic stain
E	Elastic modulus
$arepsilon_e$	Elastic strain
Δw^e	Elastic strain energy density
$N_{f,exp}$	Experimental fatigue life of the material
σ^{exp}_{max}	Experimental peak stress at reference points for calibration
σ_d	Fatigue damage stress
D_f	Fatigue damage
\widetilde{w}_f	Function of inelastic strain energy density
x_w	Geometric length of the material
σ_{hyd}	Hydrostatic stress
Δd_N	Incremental damage per cycle
dD	Increment in total damage
Δp	Increment in effective plastic strain
σ_{y0}	Initial yield stress
$arepsilon_{in}$	Inelastic strain
$\dot{arepsilon}_{in}$	Inelastic strain rate
\dot{w}_{in}	Inelastic strain energy density rate
$\dot{\varepsilon}^p$	Increment in plastic strain tensor
r(p)	Isotropic stress
b, Q	Isotropic hardening parameters of the conventional model
b,Q,b_1,Q_1	Isotropic hardening parameters with cycling
$\sigma_{{ m y}0}$	Initial yield stress
r(p)	Isotropic stress
C_i, γ_i	Kinematic hardening parameters
$a_2 - a_9$	Kinematic hardening parameters with accumulated plastic strain

$darepsilon_p$	Magnitude and direction of plastic straining
$b_1 - b_5$	Material parameters for static recovery
$\sigma^*,\dot{arepsilon}^*,m^*$	Material parameters for creep strain rate in Song's method.
$C_c, \ell_c, \varkappa, \hbar$	Material parameters for Coffin's fatigue damage method
$\gamma_l, \Omega_l, \beta_l, \alpha_l$	Material parameters for Lemaitre and Chaboche method
A_m, q_m, r_m, κ_m	Material parameters for Liu and Murakami method
a_f, ℓ_f	Material parameters for Ostergen's fatigue damage
A_p, ψ_p, β_P	Material parameters for Pandey et al. method
\mathcal{L}_p, ℓ_p	Material parameters for Priest's creep damage method
r_r, λ_r, α_r	Material parameters for Rabotnov-Kachanov method
\mathcal{L}_r, ℓ_r	Material parameters for Robinson's creep damage
$a_a, a_b b_a, b_b$	Material parameters for Song's creep damage method.
C, δ, n'	Material parameters for Song's fatigue damage method
b_1 to b_5	Material parameters for static recovery term of backstress
C_m, ℓ_m	Material parameters for Halford and Saltsman's creep damage method.
$\emptyset, \delta, \widetilde{w}_{f0}$	Material parameters for Takahashi's creep damage method.
P, Q, \emptyset , δ , E, \widetilde{w}_{f0}	Material parameters for Wang's creep damage method.
B, κ	Material parameters for failure energy density (temperature-independent parameters) used in Song's method
a, b	Material parameters for THSED and modified THSED method
$W_{f,max}$	Maximum creep fracture strain energy density.
δ_{max}	Maximum displacement
$arepsilon_{max,eq}$	Maximum equivalent strain
σ_I	Maximum principal stress
σ_m	Mean stress

D', A, r	Modified damage index constants
$arphi_{mod}$	Modified equation of φ
D_0^{mod}	Modified oxidation damage dependent on strain rate
$ ilde{\sigma}^0$	Modified peak effective stress
γ^{mod}	Modified parameter
$W_{f,min}$	Minimum creep fracture strain energy density
R_{v}	Multiaxial factor
ζ_i	Non-dimensional parameter that represents the estimate of cyclic hardening or cyclic softening rate
$arphi_{KH}$	Normalized maximum back stress at half-life for different strain amplitudes
$a_{16} - a_{18}$	Normalized back stress parameters
N	Number of cycles to failure
D_O	Oxidation damage
k_p	Oxidation rate constant
γa	Parameter represents the ratio of 'fatigue damage stress' to 'means stress'
ν	Poisson's ratio
$N_{f,pre}$	Predicted fatigue life of the material
σ^0	Peak effective stress
σ_1	Peak effective stress at the end of initial hardening and start of softening
σ_2	Peak effective stress at the end of softening and the start of secondary hardening
σ^o_{IH}	Peak effective stress in the initial hardening region
$\sigma_{\!S}^o$	Peak effective stress in softening region
σ^o_{SH}	Peak effective stress in the secondary hardening region
$\Delta \varepsilon^p$ or $\Delta \varepsilon_p$	Plastic strain range
Δw^p	Plastic strain energy density

ε^p or ε_P	Plastic strain
λ	Plastic multiplier
N_{pre}	Predicted life
σ^{pre}_{max}	Predicted peak stress at reference points for calibration
q	Radius of memory surface or Maximum plastic strain range
K, m	Rate-dependent viscous material parameters
arphi	Ratio of the maximum back stress at any cycle to the maximum back stress at 1^{st} cycle
t_r	Rupture time
J_2	Second invariant of deviatoric stresses
$\tau(p)$	Static recovery temperature dependent material parameter
\mathcal{E}_f	Strain at fracture/rupture
σ	Stress
$\Delta\sigma$	Stress amplitude
С	Stiffness matrix
Δw^c	Strain energy density due to creep
$R_{arepsilon}$	Strain ratio
Ė	Strain rate of cyclic loading
$a_{10} - a_{12}$	Strain range memory-dependent softening parameter
$a_{13} - a_{15}$	Strain range memory dependent secondary hardening parameter
σ_r	Stress relaxation
$\sigma(t)$	Stress relaxation rate
σ^0	Size of the yield surface
t	Time
σ^{tr}	Trial stress
f_t , f_c	Tension and compression frequency factor
σ_{max}	Tensile peak stress

T or T_{abs} Temperature Δw^t Tensile hysteresis strain energy density Thermal recovery temperature dependent material parameter. $\tau(p)$ Threshold stress σ_{th} Total back stress $\sum_{i=1}^{n} x^{i}$ $\boldsymbol{\chi}$ $\Delta \varepsilon$ Total strain range w^{total} Total tensile strain energy density σ^{tr} Trial stress Ultimate displacement under monotonic loading δ_u n^* Unit normal to the memory surface Unit normal to the yield surface n \widetilde{w}_{f0} Upper bound of \widetilde{w}_f (function of inelastic strain energy density) Weight factor β_{ap} f Yield function \vec{x} Represents vector (Voigt notation of tensor quantity)

 $x \text{ or } x_{ij}$ Represents tensor x' Represents deviatoric component

Abbreviations Description

Abagus material subroutine (UMAT) Advanced ultra-supercritical **AUSC AISI** American Iron and Steel Institute **ASTM** American Society for Testing and Materials CCCreep strain in both tension and compression CP Creep strain in tension and plastic strain in compression **CPSED** Cyclic plastic strain energy density CFI/U-CFI Uniaxial creep-fatigue test

IN Inconel

PC Plastic strain in tension and creep strain in compression

SEDE Strain energy density exhaustion

THSED Tensile hysteresis strain energy density

H-CFI Hybrid creep-fatigue loading

NU Non-unified model

SS Stainless steel

1.1. Background

The world's demand for electricity has increased by 2.2% in 2023 [1] and is expected to rise further in the coming decade. While nuclear power plants produce clean energy, coal-fired thermal power plants are the major source of energy production in developing countries. To meet the outrageous energy demand and reduce greenhouse gas emissions, developing countries are looking towards electricity generation from nuclear power plants and advanced ultra-supercritical (AUSC) power plants. With respect to the conventional coal-fired power plant, the AUSC power plant is expected to enhance the efficiency from <35% to >47%, with overall CO₂ emission reduction by ~10%-35%, for an increase in stream temperature from 600-650 °C to 700-760 °C [2]. However, the increase in steam temperature requires the development of new materials and an understanding of their performance under service conditions.

The AUSC power plant components are designed to withstand an average steam temperature of (700-725°C) for ~11.5 years (~10⁵ hours) with an average stress to rupture of 25-35 MPa [3]. In contrast, fast-breeder nuclear reactors undergo high temperatures of up to 700 °C for 40-60 years with high peak neutron doses of more than 100 dpa [4]. Moreover, with modernization, the electricity demand varies throughout the day, consisting of 2 hours of intermediate demand followed by 8 hours of low demand, 7 hours of intermediate demand, and 7 hours of peak demand [5], as depicted by Figure 1.1(a). This fluctuation in demand is met by maneuvering the power plant, i.e., operating the reactor under different operational modes [5]. As depicted by Figure 1.1(b), the temperature rises or drops during maneuvering or due to the intermittent nature of cyclic start and stop operation schedules [2,5]. The components exposed to high temperatures try to expand or contract, but due to structural constraints, thermal stresses are developed. Such thermal stresses developed due to cyclic start-up and shut-down operations cause low cycle fatigue in components like main heat transport piping, reactor vessels, boilers, and heat exchangers used in power plants. The low cycle fatigue is known to cause surface crack formation [6]. When electricity demand is constant, the power plants are operated under constant load and thus undergo creep loading, which appears as intergranular or grain boundary cavitation [6]. Therefore, the components in the powerplant undergo creep-fatigue loading at a high

temperature every day.

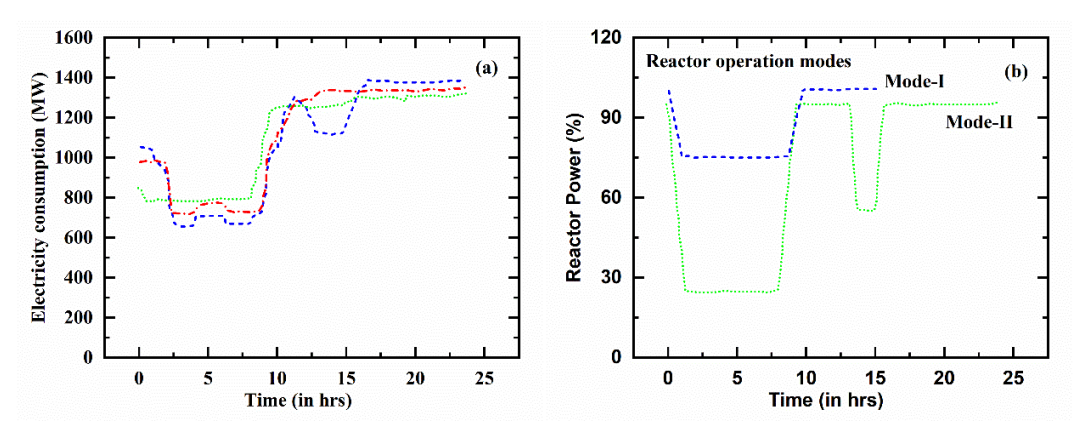


Figure 1.1. (a) Electricity demand in (kW) with time period of day (b) Reactor operational mode with time in (hrs) [5].

The AUSC and fast-breeder nuclear power plant components operating at such high temperatures interact with the environment, causing the oxidation of materials. It is reported that the interaction of oxidation phenomenon with creep and fatigue phenomena shortens the crack initiation period [6–8], and the combined effect causes the material to fail faster. Hence, to analyze the component behavior accurately in the laboratory, the materials are tested under various loading conditions (such as pure fatigue (PF), uniaxial creep-fatigue (U-CFI), etc.) to study materials' cyclic response, microstructural evolution, and life.

Because of the complexities and economic constraints involved in the experimental analysis of these materials on a large scale, the field of computational modeling has emerged significantly with the advancement of computers. Simulation has reduced extensive experimentation and physical modeling in everyday engineering applications [9]. A similar trend has also been observed in the field of structural analysis. Constitutive models (a mathematical relationship between stress and strain) have been extensively used to simulate and predict responses to different mechanical and thermal loading conditions.

1.2. Motivation of the work

Materials like austenitic stainless steel (e.g., AISI 304L, 304LN, 316L, 316LN, 321), ferritic steels (e.g., P91, 2.25CR-1Mo), and Ni-based superalloys (e.g., Alloy 617, IN 750H) are considered to be suitable candidates for different components in fast-breeder reactors and advanced ultra-supercritical power plants to withstand the complex loading undergone by power plant components [10–13]. These materials possess high-temperature strength, phase stability, and excellent resistance to aqueous corrosion [3]. Under low-cycle

strain-controlled fatigue loading, different structural steels exhibit different behaviors. Ferritic-Martensitic steel (e.g., 9Cr-1Mo, 2.25Cr-1Mo steel) shows continuous softening or softening followed by saturation behavior, respectively [10,11]; Ni-based superalloy 617 shows hardening behavior, while IN 750H shows continuous softening [12,13], Many austenitic steels such as 304L SS, shows cyclic initial hardening, softening, saturation, and secondary hardening behavior, and 321 SS show cyclic softening followed by hardening behavior (as per our experimental data), Figure 1.2. shows the cyclic stress variation of the different materials stated above.

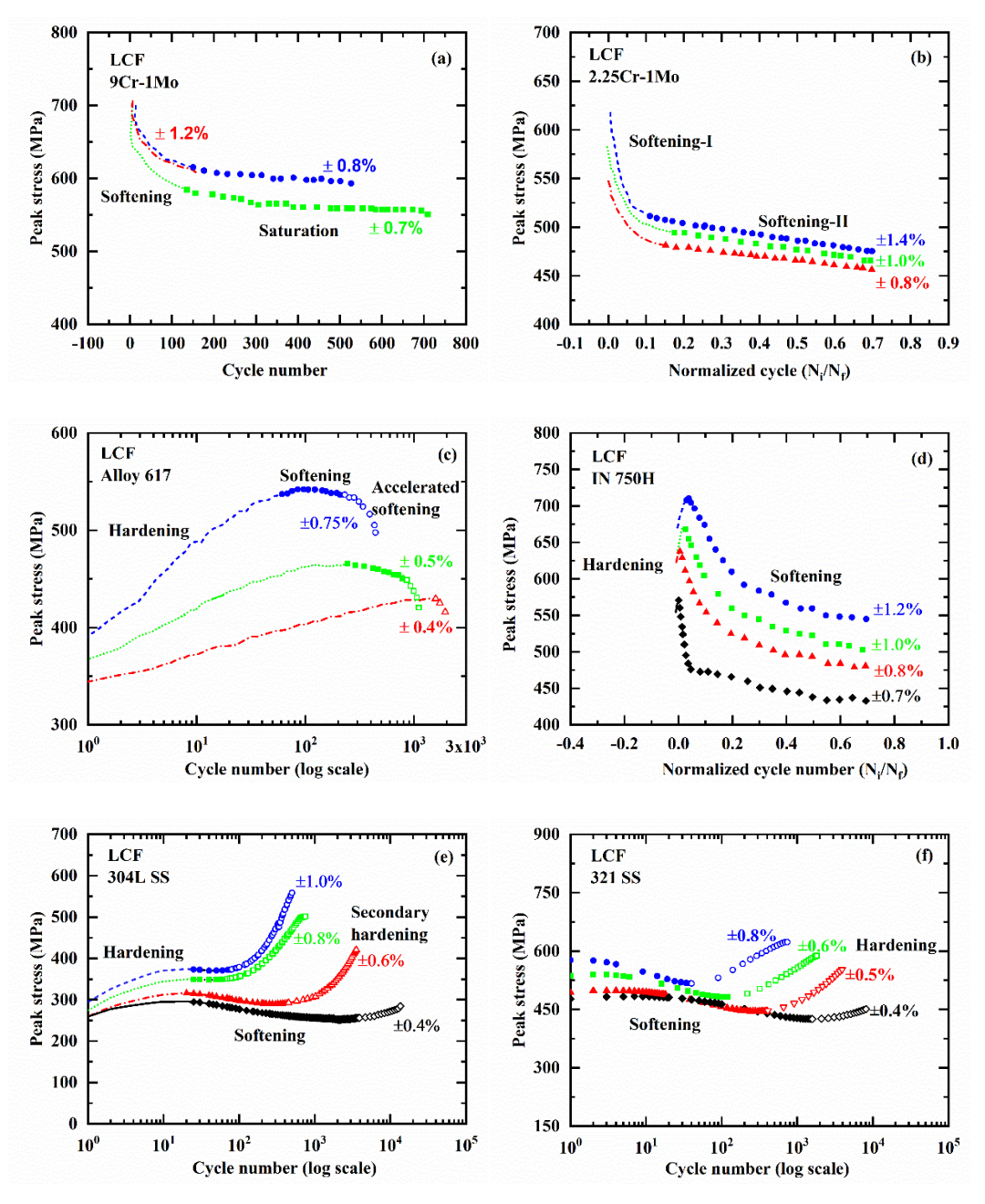


Figure 1.2. Cyclic peak stress variation with cycle number for different materials (a, b) ferritic -martensitic steel [10,11] (c, d) Ni-based superalloy [12,13] (e, f) Austenitic steel.

The cyclic deformation behavior of materials ultimately causes the hysteresis loop to show Masing/non-Masing behavior [14,15]. Yadav et al. [16] have recently classified the non-Masing behavior into Type-I and Type-II. According to their definitions, for Masing behavior, the linear elastic stress limit ($2\sigma^0$) and strain hardening rate behavior (*i.e.*, loop shape) of hysteresis loops do not change with strain amplitudes, as shown in Figure 1.3. However, for non-Masing Type-II, only the linear elastic stress limit changes with strain amplitude, and for non-Masing Type-II, both the linear elastic stress limit and strain hardening rate change with strain amplitude, as shown in Figure 1.3. More details about the Masing/non-Masing behavior of materials can be found in the review article [17]. Most constitutive models available in literature deal with material fatigue behavior without any reference to the Masing/non-Masing behavior. Although the Masing behavior is well defined and modeled in the literature [18]. There is still a need to investigate the influence of Type-I and Type-II non-Masing behavior on the strain range memory effect and, subsequently, to develop a constitutive model for LCF behavior.

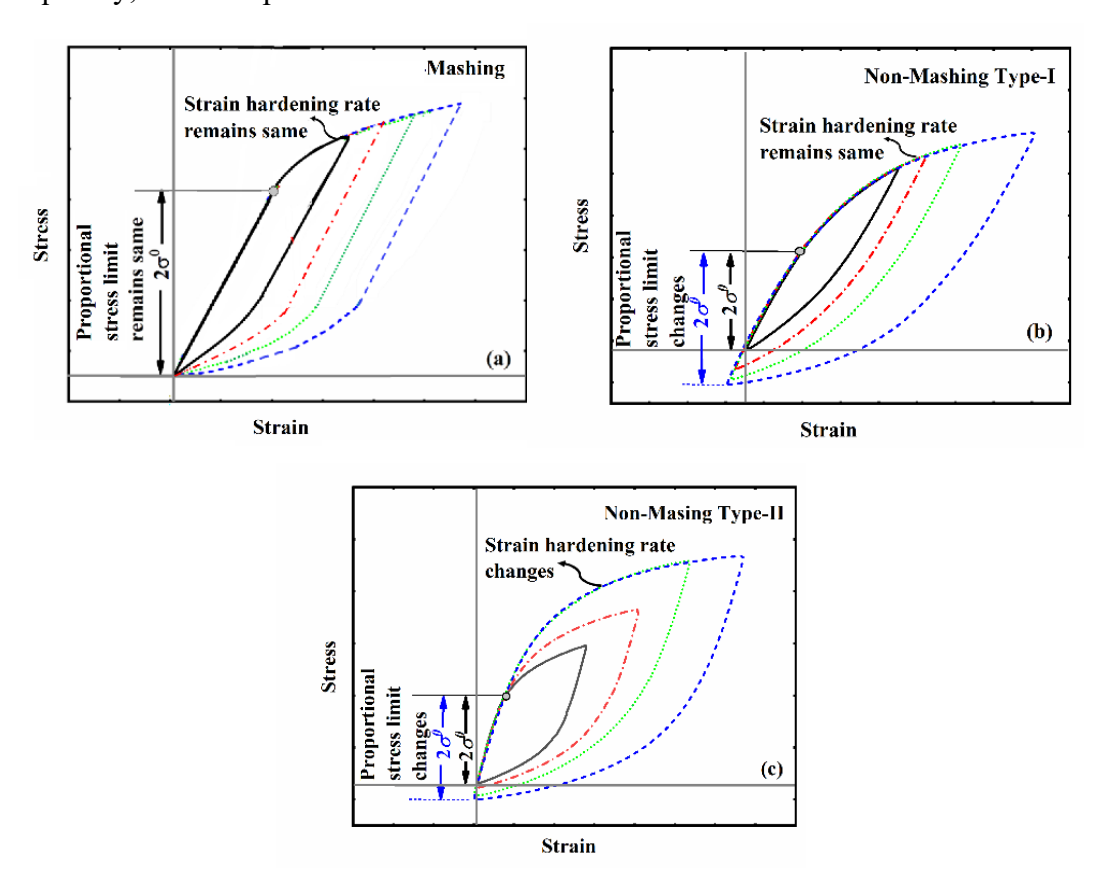


Figure 1.3. Stress-strain loops at material's half-life showing (a) Masing [13] (b) Non-Masing Type-I [16] (c) Non-Masing Type-II behavior [16].

The components in the powerplant undergo creep-fatigue loading at a high temperature every day. The synergistic combination of the creep-fatigue-environment effects at high temperatures leads to accelerated failure of the components [19–22]. The oxidation damage can be, in general, summarized as the factor that degrades the material performance and is considered a surface and sub-surface phenomenon that depends on time and temperature [21,23–27]. The accurate life prediction considering creep, fatigue, and oxidation under different loading conditions and strain paths is critical and necessary for prognostic and health management of the actual components at elevated temperatures. According to the open literature, the prediction of material life at high temperatures depends on the loading, strain waveform, and environmental conditions. Different methodologies have been suggested to predict material life [28]. Most of these methods used for creepfatigue life prediction use complicated fitting prType equation here occdures with many model parameters without considering the effect of oxidation. Thus, a robust life prediction method that eases complicated fitting procedures with the inclusion of the effect of oxidation damage is still required.

The interaction of complex time-dependence (oxidation and creep) and time-independent (fatigue) phenomena causes difficulties in identifying the damaged locations in real structures. Numerically, the key locations/areas where material degradation is likely to occur, can be done by analyzing the maximum state of stress or strain accumulation developed in the material. In this regard, the continuum damage mechanics theories combined with constitutive laws help to establish the material's microstructural degradation through the cumulative damage state. In literature, many constitutive laws based on unified and non-unified theories of strain decomposition exist in the constitutive modeling field that predicts the mechanical behavior of materials subjected to creep and fatigue loading. In contrast, limited models are available in the literature that combines the continuum damage mechanics theory with constitutive laws[29]. Thus, the field of constitutive modeling still needs to be enriched to take into account the interaction of damage (time-dependent and time-independent phenomena) for high reliability and accuracy to simulate the experimental behavior of the materials.

1.3. Objectives

Based on the above insights, the main objectives of the present thesis are defined as:

1. To develop a constitutive model based on modification of the hardening laws to predict the initial hardening, softening, saturation, and secondary hardening behavior shown by the material under strain-controlled low-cycle fatigue loading.

- 2. To investigate the influence of Type-I and Type-II non-Masing behaviors on the strain range memory effect and develop a constitutive model that can accurately predict the material's Type-I and Type-II Non-Masing behaviors.
- 3. To quantify the creep, fatigue, and oxidation damage and life prediction of different materials under various loading conditions such as uniaxial creep-fatigue (U-CFI) and hybrid creep-fatigue (H-CFI).
- 4. To develop a unified constitutive model for creep-fatigue loading incorporating physical degradation, *i.e.*, damage and generalized constitutive response.

1.4. Organization of the thesis

The research work performed in the present thesis is organized into seven chapters. A chapter-wise breakup of the thesis work is as follows,

Chapter 1: Introduction

This chapter briefly reviews the loading scenario in AUSC and fast breeder reactors and the associated damage phenomena. Subsequently, the macroscopic behavior (*i.e.*, hysteresis stress-strain loop shape and cyclic peak stress variation) of various structural steel that can be used in different components of AUSC and fast breeder reactor components is discussed. Based upon the discussion, the objectives of the present study are outlined

Chapter 2: Literature review

This chapter covers the literature review on the chronological development of various constitutive models used to predict steel's fatigue and creep-fatigue behavior. Thereby, the enrichment needed in the field of constitutive modeling to incorporate the different cyclic behavior shown by various structural steel, creep-fatigue model to incorporate the damage mechanics theory, and stress-relaxation behavior with cycling, is justified. Also, in brief, the basic theory of the constitutive model is discussed.

Chapter 3: Modified isotropic and kinematic hardening equations for 304L SS under low cycle fatigue

The 304L stainless steel exhibits cyclic behavior characterized by initial hardening, softening, saturation, and secondary hardening. Existing classical and modified models have struggled to accurately capture all four of these features. To address this limitation, this chapter introduces modified kinematic and isotropic hardening laws based on accumulated plastic strain. The significant influence of secondary hardening is incorporated through a newly introduced non-dimensional function, which depends on the memory of

the maximum plastic strain range (q). Additionally, another function, φ_{KH} , is introduced to account for the dependence of the maximum back stress on strain amplitude. The proposed constitutive model is implemented in ABAQUS as a user subroutine (UMAT) and validated using strain-controlled low-cycle fatigue test data for 304L stainless steel.

Chapter 4: Type-I and Type-II non-Masing behaviors of materials under low cycle fatigue: Constitutive modeling and simulation

The cyclic deformation behavior of materials ultimately causes the hysteresis loop to show Masing/non-Masing behavior [14] [15]. Yadav *et* al. [16] have recently classified the non-Masing behavior into Type-I and Type-II. Thus, here we investigate the influence of Type-I and Type-II non-Masing behavior on the strain range memory effect and addressed the constitutive modeling of LCF behavior. In a previous chapter, we proposed modified isotropic and kinematic hardening laws to simulate the cyclic hardening, softening, saturation, and significant secondary hardening behavior of 304L SS under LCF at room temperature. The strain range memory effect was only considered for the secondary hardening (SH) behavior. The modifications proposed predict secondary hardening well. However, the modifications aim to further improve the modeling of overall cyclic behavior. These are specifically important for materials like 321 SS that show significant variation in the cyclic softening rate with strain amplitude.

The proposed model in this work considers the strain range memory effect for both the cyclic hardening and softening behavior, thus enhancing its applicability for various materials. The proposed model considers the strain range memory effect for the translation and expansion of the yield surface with the help of a non-dimensional function, ζ . Also, the identification of material parameters and optimization methods are highlighted to improve cyclic prediction. The proposed constitutive model is implemented in ABAQUS as a user subroutine (UMAT) for simulating the LCF behavior of 304L SS and 321 SS materials. The experimental and simulated results show that the prediction of non-Masing Type-I and Type-II is done accurately. Also, the peak stress with cycling shows good accuracy.

Chapter 5: Quantification of the creep, fatigue, and oxidation damage and life prediction

In literature, many methods are available to predict the creep-fatigue life of a material. Most of the methods mentioned in the literature use complicated fitting procedures and many model parameters to predict the life of the material under creep-fatigue conditions. The open literature has proposed the net tensile hysteresis energy density method (THSED) to overcome this difficulty. The method uses the model

parameter (γ_d), which is said to be found by the hit and trial method. In this chapter, the oxidation kinetics approach is considered to predict damage due to oxidation as surface and sub-surface phenomena. It is observed that the model parameter (γ_d) used by Wang et al. [40] for P91 steel at 550 °C, Haynes 230 at 850 °C, Alloy 617 at 850 and 950 °C, and Inconel 625 at 815 °C, is proportional to the ratio of oxidation damage with strain rate. Thus, here we propose the modified THSED considering the γ_d as the model parameter rather than numerical constant determined by hit and trial method. The THSED method is extended for uniaxial creep-fatigue (U-CFI) and hybrid creep-fatigue (H-CFI) loading conditions. The model is validated for the austenitic, ferritic stainless steel, and Ni-based superalloy for different loading conditions. Experimental data for validating the modified THSED method is collected from various papers. The prediction capability of the proposed modified THSED model is compared with modified strain energy density exhaustion method (SEDE) (that considers oxidation damage) [28] and existing THSED [30] methods available in the open literature.

Chapter 6: Continuum damage mechanics based unified model for creep-fatigueoxidation

The continuum damage mechanics-based constitutive models help establish the deterioration in components through the cumulative damage state, which can predict the microstructural degradation and crack propagation. Thus, in this chapter, Chaboche's viscoplastic model [32] is used to take into account creep and fatigue together with modified hardening laws (to develop a generalized fatigue model). The modified unified model is coupled with damage to predict a component's mechanical state and the material's behavior under creep-fatigue loading. The tests are performed at a temperature of 650 °C, at a strain amplitude of $\pm 0.6\%$ with a strain rate of 1×10^{-3} and a peak tensile hold of 60 sec, 180 sec, and 300 sec and peak compression hold of 60 and 180 sec. The experiment and simulated results are compared, *i.e.*, variation of peak stress with cycle number and stress-strain loops and stress-relaxation with hold time for selected cycles. The results show good agreement.

Chapter 7: Conclusions and future scope

The final chapter summarizes the key findings of the research. The chapter will discuss this study's implications, its contributions to the field, and suggest avenues for future research.

**Note

The thesis has been written based on the articles published (or under review/to be submitted) in different journals. All the results, discussions, and conclusions published in those articles were part of the research work. Each chapter of the thesis contains the results of a particular article; however, some modifications were made to get continuity in the story and avoid repetitions. Each chapter represents a part of the story and can be read independently.

Neha Mehani

Email: 2017msz0002@iitrpr.ac.in

Date:

Place: Rupnagar, Punjab, India

2.1. Introduction

Constitutive modeling is the development of mathematical models to describe a material's or system's constitutive behavior to external stimuli like mechanical/thermal loading. It is a numerical approach used to capture the behavior of materials under different loading conditions. The mathematical models used in constitutive models represent the relationship between two or more physical variables like stress, strain, temperature, etc. In the context of fatigue and creep-fatigue behavior of materials, the constitutive models usually represent how the material would respond to externally applied cyclic loading in terms of stress or strain responses. Ultimately, based on those stress and strain responses, the damage accumulation and life of a material or component are predicted.

As reported in the literature, the cyclic plasticity models can be classified into two broad categories based on whether they explicitly use the internal variables to predict the elastic-plastic behavior of material or they consider the path-dependent strain or stress integrals over time (such as endochronic theory models), as shown in Figure 2.1 [18,33]. Furthermore, internal variable concept considers that the state of material at any point depends on the evolution of the internal variables, which depends on the both current state and history of material. [18,34].

Most models nowadays are based on the internal variable concept due to their reduced complexity and more straightforward implementation [18]. The internal variable-based models are further classified as subloading surface models (i.e., the expansion of loading surface) and kinematic hardening models (i.e., translation of yield surface), as shown in Figure 2.1 [18,33]. This classification is based upon how they incorporate the transition from elastic to plastic state. The initial sub-loading model hypothesizes two surfaces: yield surface and subloading surface. The plastic strain rate can develop in the material even when the stress state is elastic, i.e., there exists no purely elastic domain. The subloading surface always passes through the current state of stress, which evolves with plastic deformation until it reaches the yield surface and coincides. The subloading surface is formulated in such a way that it does not expand over the yield surface. Thus, it always provides a smooth transition between elastic and plastic states of material behavior. The model is mainly used for polymers, soils, clay, and geomechanics [33].

While the simplest constitutive model that considers the reduced yield stress on the application of reverse lading is given by Prager to take into account the Bauschinger effect [35–37], it considers that the back stress is linearly proportional to the plastic strain. The main drawback of the model is that stress-strain loops consist of linear segments, while the experiments show that the material exhibits non-linear behavior. To overcome this difficulty, non-linearity is introduced in the constitutive models by considering the translation-based models, which are mainly classified as multi-surface [33] (Besseling model [38] and Mroz model [39]) and two-surface model [33] (Dafalias and Popov[37], Krieg [40], Yoshida and Uemori model [41], *etc.*).

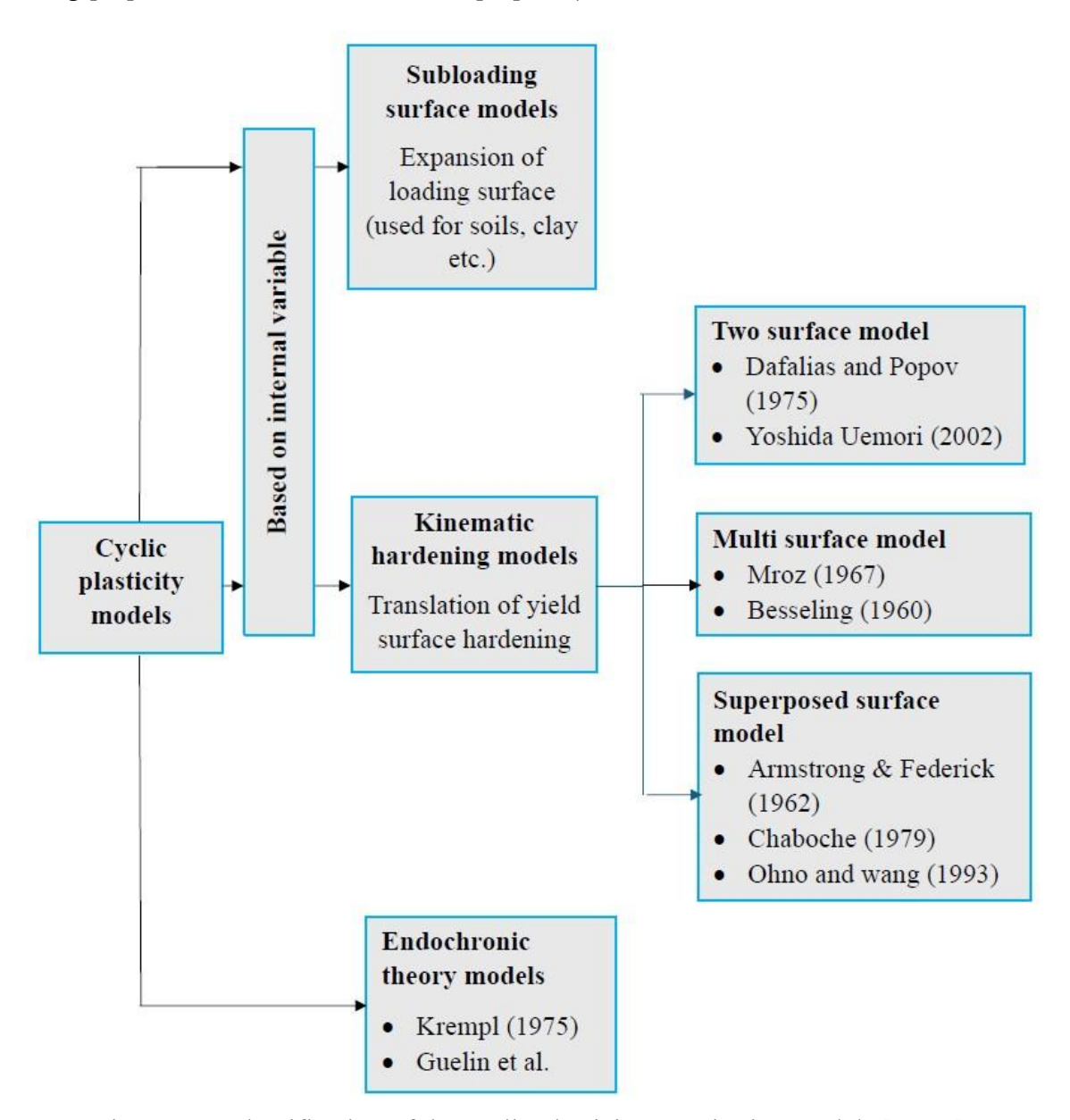


Figure 2.1. Classification of the cyclic plasticity constitutive models [18,33].

The Besseling model [38] theory considers the material to be macroscopically homogeneous but inhomogeneous on the microscopic scale. The model assumes that the

plastic deformation in the material would start at specific locations and spread across the entire volume with increased stress. These phenomena in the model are considered by taking into account many sub-volumes, where each of the sub-volumes can have different yielding strengths despite being subjected to the same overall strain. Thus, each sub-volume shows the hardening phenomena and is considered as the linear function of strain (or plastic strain). Therefore, if sub-layers are considered adequate in number, then the number of linear sections can accurately describe the non-linear stress-strain curve. However, the smooth transition is almost impossible sto occur, and the hysteresis loop will be composed of several linear segments.

Mroz's model [39] used the concept of "field of work-hardening moduli" instead of single modulus "C" and predicted the Bauschinger effect accurately. Thus, the model can predict the non-linearity exhibited by the experimental stress-strain loops. Also, the model can accurately predict cyclic hardening and cyclic softening effects under symmetric loading conditions. However, the model fails to show the cyclic hardening followed by softening or cyclic softening followed by hardening that occurs in a material under asymmetric loading.

One of the main difficulties with the multi-surface model is the large number of surfaces necessary to describe the experimental behavior of the material. Each surface needs the storage of a tensor variable (usually six components) and a scalar one. Several models were then developed to obtain the same specific properties using only two surfaces: the yield surface and the bounding surface (or limit surface). Dafalias-Popov model [37] considers two surfaces: the loading surface and the bounding surface, the same as the combined hardening model. The backstress is regarded as the loading surface, while isotropic stress is the bounding surface. The yield surface in stress space is restricted in these models to move inside an outer surface, denoted by $f(\sigma, \varepsilon) = 0$, also referred to as the bounding surface, loading surface, or memory surface.

Yoshida and Uemori [41] have modified the Dafalias and Popov model [37] and consider the two surfaces: the inner surface (*i.e.*, active surface) and bounding surface (*i.e.*, yield surface). The inner surface translates due to kinematic hardening in stress space to reach the yield surface (*i.e.*, isotropic nature). The model can also consider the 3rd hardening surface to include the memory effect, thereby showing more complex phenomena exhibited by the material (such as hardening followed by saturation). Although the model can simulate cyclic plasticity at large plastic strain ranges for metals exhibiting cyclic hardening

followed by saturation, but cannot predict the accumulation of plastic strain under constant stress amplitude. Moreover, it is experimentally observed that the materials undergoing the cyclic loading can exhibit initial hardening followed by softening or hardening at a decreased or increased rate. The model fails to predict such complex features shown by the material.

Further, the two hypotheses, isotropic and kinematic hardening are superimposed and are considered in combined form to predict the nonlinear hardening regime exhibited by material under cyclic loading. Such models are known as superposed surface models. Chaboche model [18] is one the most used superposed model due to its inherent simplicity and accuracy in simulating the Masing kind of cyclic response shown by various structural materials [17]. The model assumes that kinematic hardening governs the shape of the hysteresis loop, and isotropic hardening governs the change in the maximum/peak stress from one cycle to another [18]. The constitutive laws discussed above could not model cyclic hardening/softening with stabilization or persistent cyclic hardening after stabilization exhibited by some material under cyclic loading. Thus, Chaboche et al. [11] considered the maximum plastic strain range memory effect on isotropic hardening variables to simulate such materials' cyclic stress-strain response. The asymptotic isotropic hardening variable was defined based on the largest plastic strain range history by considering a new index function representing a hypersphere. Many researchers have made several modifications based on the Chaboche et al. [11] plastic strain memory model because of its simplicity and accuracy, to include the combination of hardening /softening behavior exhibited by various steels undergoing low cycle fatigue loading. Such as Ohno and Wang [42] [43], Jiang and Sehitoglu [44], Krishna et al. [45], Nouailhas et al. [46], Khutia et al. [47], Taleb et al. [48], Xu et al. [49], Zhu et al. [50], Zhou et al. [51], Zhang and Jiang [52], Abdel-Karim and Khan [53], etc. Zhou et al. [51] and Song et al. [13] have also modified the Chaboche et al. [11] plastic strain memory model and claimed that their model can simulate the initial hardening, softening, and secondary hardening behavior. However, it should be noted that Zhou et al. [51] have not validated their model for the material that shows secondary hardening. In contrast, Song et al. [13] have validated their model for a material that shows negligible secondary hardening, almost close to the saturated response.

Thus, developing a model that can simulate a significant amount of secondary hardening is still required. As reported in Chapter 2: Section 1.2, the material can demonstrate some (or all) of the cyclic features like initial hardening, softening, saturation,

and secondary hardening. The classical and modified models developed to date cannot address cyclic behavior comprising all four features. Thus, there is still a need for a constitutive model to describe the cyclic behavior of materials irrespective of the sequence of the cyclic features exhibited. Moreover, the constitutive models available in the open literature can predict the cyclic behavior exhibiting either 'Masing' or 'non-Masing Type-I'. However, no article in the literature has demonstrated (or validated) any constitutive model for simulating materials' Type-I and Type-II non-Masing behavior.

Further, the time-dependent phenomena such as stress-relaxation, *i.e.*, decrease in stress under constant strain, is modeled by combining the fatigue constitutive laws with creep constitutive laws using a unified approach [54–57] and a non-unified approach [58–60]. It is reported in the literature that the unified approach predicts the experimental behavior accurately and is easy to implement [61]. Thus, many modified models based on a unified approach exist in the literature that take into account the effect of mean stress, strain rate, strain amplitude, and hold time [54–56]. In the open literature, the effect of change in stress relaxation with cycling is taken into consideration only for 9Cr-1Mo steel (exhibits continuous softening behavior) in articles [57,62]. Moreover, the incorporation of damage is essential (especially for material undergoing complex degradation mechanisms, *i.e.*, fatigue, creep, and oxidation) in constitutive models to improve its numerical prediction and accurate prediction of material deterioration. Thus, in the present study, a damage mechanics-based unified constitutive model that incorporates the change in stress relaxation with cycling is proposed.

As discussed in Chapter 1: Section 1.1, the increasing energy demands call for new advanced material development for extremely high-temperature applications where oxidation damage cannot be avoided. Usually, the damage prediction models for creep-fatigue interaction loading conditions do not take into account the oxidation damage. These models consider the contribution of creep and fatigue damage separately, and the total creep-fatigue damage is often estimated using damage summation rules, such as linear [63], bi-linear [64], and non-linear [65,66] formulations. The pure fatigue damage is predicted using traditional approaches such as Coffin-Manson relationship and its modifications [67–69], while the creep damage is calculated using the time fraction (TF) rule [70] and ductility exhaustion (DE) method [71–73], strain energy density exhaustion method [74,75], and their later modifications [28,76–78]. There is a need to develop a damage model that accurately captures the creep-fatigue and oxidation damages and provides reliable life prediction.

A brief literature review is presented here from the point of view of the historical development of different models in chronological order. A detailed literature review specific to the research objectives is presented in each chapter in the introduction section. A brief review of the fundamental laws of constitutive modeling, which are used in the current investigation for developing the constitutive models, is discussed in Section 2.2.

2.2. Basic concepts of modeling

Modeling of plasticity is based on three main ingredients (*i.e.*, theoretical expressions) that are given as:

- 1. Yield criterion
- 2. Flow rule
- 3. Consistency condition

2.2.1. Yield criterion

The stress below which the material deforms elastically, *i.e.*, it regains its original shape, is known as yield stress, defined for uniaxial loading [79,80]. For the complex 3-dimensional state of stress, the yield criterion determines the stress level at which yielding, *i.e.*, plasticity, is initiated. The plastic behavior of homogeneous, isotropic materials can be represented by a yield function, as shown by Eq. (2.1) [79–81].

$$f(\boldsymbol{\sigma_{ij}}) = \sigma_e - \sigma_{y0} \tag{2.1}$$

$$\sigma_e = \sqrt{\frac{3}{2} \left(\sigma'_{ij} : \sigma'_{ij} \right)} \tag{2.2}$$

Where σ_e represents equivalent stress that depends on the stress tensor (σ_{ij}) and σ_{y0} represents the initial yield stress, *i.e.*, material yield parameter.

The yield criterion comprehends the formation of the yield surface in the stress space, where the yield surface defines the boundary between elastic and plastic region (considering von Mises yield criterion) [79–81].

Mathematically, three possible cases of stress state can occur [79–81] are given as:

- $f(\sigma_{ij}) < 0$: the equivalent stress is lower than material yield $f(\sigma_{ij}) < \sigma_{y0}$. The stress state point is inside the yield surface, and the material behaves elastically (no plastic strain occurs).
- $f(\sigma_{ij}) = 0$: plasticity condition the equivalent stress is equal to the material yield strength σ_{y0} . Stress state point lies on the yield surface.

• $f(\sigma_{ij}) > 0$ plastic behavior of material occurs.

In reality, the third option is not possible at all since it violates the consistency condition. Therefore, the stress state can only lie on the yield surface and the yield surface "moves" or "expands" along if the stress state tends to move outside the surface. The hardening rule describes this phenomenon.

2.2.2. Flow rule

The flow rule gives the magnitude and direction of the plastic straining. It is given by Eq. (2.3) [79–81].

$$d\boldsymbol{\varepsilon_{ij}^p} = \partial \lambda \frac{\partial Q}{\partial \boldsymbol{\sigma_{ii}}} \tag{2.3}$$

Where $\partial \lambda$ is the plastic multiplier that determines the amount of plastic strain increment, Q is the plastic potential function, and $\frac{\partial Q}{\partial \sigma_{ij}}$ is the direction of plastic strain increment

The flow rule is said to be associative if the yield function (f) and the plastic potential function (Q = f) are equal, *i.e.*, plastic strain increment is normal to the yield surface [79–81]. According to Drucker's postulate [79–81], this is valid for stable materials whose yield surfaces are convex (convexity rule) and whose plastic strain increments vector at a smooth yield surface point is given in the direction of the yield surface's normal (normality rule). It guarantees a unique solution for the boundary value problem.

2.2.3. Consistency condition

The consistency condition states that for time-independent plasticity, the load point always remains on the yield surface during plastic deformation [79–81]. It is observed experimentally that the yield stress can increase or decrease and is found to be a function of effective plastic strain, p. Thus, yield function can be given by Eq. (2.4)

$$f(\boldsymbol{\sigma_{ij}}, p) = \sigma_e(\boldsymbol{\sigma_{ij}}) - \sigma_y(p) = 0$$
 (2.4)

$$\dot{p} = \sqrt{\frac{2}{3} \left(\dot{\varepsilon}_{ij}^p : \dot{\varepsilon}_{ij}^p \right)} \tag{2.5}$$

Once the plasticity begins, it must be ensured that stress-state does not move back to elastic region, and it stays on or moves along the yield surface, i.e., Eq. (2.6). Therefore, if the stress state goes beyond the yield surface using the radial return method the stress is updated such that it falls back on yield surface as explained later in Section 2.5.

$$df(\boldsymbol{\sigma}_{ii}, p) \ge 0 \tag{2.6}$$

Engineering materials, *i.e.*, any metals under uniaxial loading, show strain hardening behavior, i.e., yield stress or size of yield surface increases with an increase in plastic strain. However, stress can be more than the yield strength of the material. Thus, if the stresses can surpass the yield strength without being able to exit the yield surface, then the yield surface will need to alter throughout the hardening process. It can be brought about by a combination of concentric expansion, translation, and/or shape change. Which, in turn, is decided by the direction and magnitude of plastic straining [79–81].

It is observed experimentally that the yield stress can increase or decrease and is found to be a function of effective plastic strain, p; thus, the consistency condition is written, for an incremental change in stress and effective plastic strain, as shown by Eq. (2.7) [79–81].

$$f(\boldsymbol{\sigma_{ij}} + d\boldsymbol{\sigma_{ij}}, p + dp) = 0 \tag{2.7}$$

The consistency condition, along with the normality hypothesis and the hardening rules enables us to determine the plastic multiplier, or equivalently, for a von Mises material, the increment in effective plastic strain [79–81].

2.3. Yield surface expansion and translation

2.3.1. Yield surface expansion (isotropic hardening)

The material is loaded below a certain amount of load, *i.e.*, yield point; on unloading, the material regains its original shape and shows elastic behavior. When loaded beyond the yield point (let us say up to load level A), the material shows permanent deformation, i.e., plastic behavior. Now, suppose we unload the material and load it again up to load level A. In that case, the material will again show elastic behavior, *i.e.*, the stress required to introduce further plastic deformation increases as a function of accumulated plastic strain [79–81]. It defines the expansion/contraction of the yield surface in all directions by an equal amount, as shown in Figure 2.2 [79–81].

Mathematically, it can be represented as:

$$\sigma^0 = \sigma_{v0} + r(p) \tag{2.8}$$

Where, σ^0 and σ_{y0} are the size of the yield surface and initial yield surface or initial yield stress, respectively. The isotropic hardening function r(p) describes the increment/decrement in yield surface size from one cycle to another.

$$\sigma^0 = \sigma_{v0} + r(p) \tag{2.9}$$

$$r(p) = Q(1 - e^{-bp}) (2.10)$$

Q and b are isotropic hardening parameters that are obtained from experimental data. Q represents the saturated (i.e., maximum/minimum) value of the function (r), and b represents the rate at which the saturation is achieved by the function (r) [79–81]. Furthermore, p represents the accumulated plastic strain, which is calculated [79–81] as given by Eq. (2.11). i is the cycle number

$$p = (4i - 3)\frac{\Delta \varepsilon^p}{2} \tag{2.11}$$

Here, $\Delta \varepsilon^p$ represents the plastic strain range, which is given as the difference between the total strain range and the elastic strain range. [79–81].

$$\Delta \varepsilon^p = \Delta \varepsilon - \frac{\Delta \sigma}{E} \tag{2.12}$$

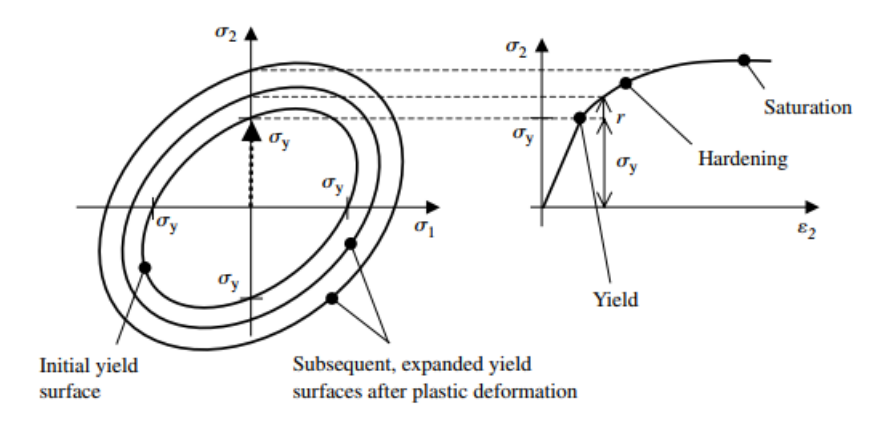


Figure 2.2 Expansion of yield surface under tensile loading and corresponding stressstrain curve [80].

2.3.2. Translation of yield surface (kinematic hardening)

When the material is loaded-unloaded, followed by loading in the reverse direction, the stress required to cause the plastic deformation in the reverse direction is less than the initial yield stress (*i.e.*, Bauschinger effect). It is hypothesized by considering that the yield surface translation takes place like a rigid body motion in stress space rather than

expansion/contraction, as shown in Figure 2.3 [79–81]. During the cyclic loading, it defines the shape of the loop. The shift in the position of the yield surface is denoted by back stress (x). The back stress (x) is given as Eq. (2.13)

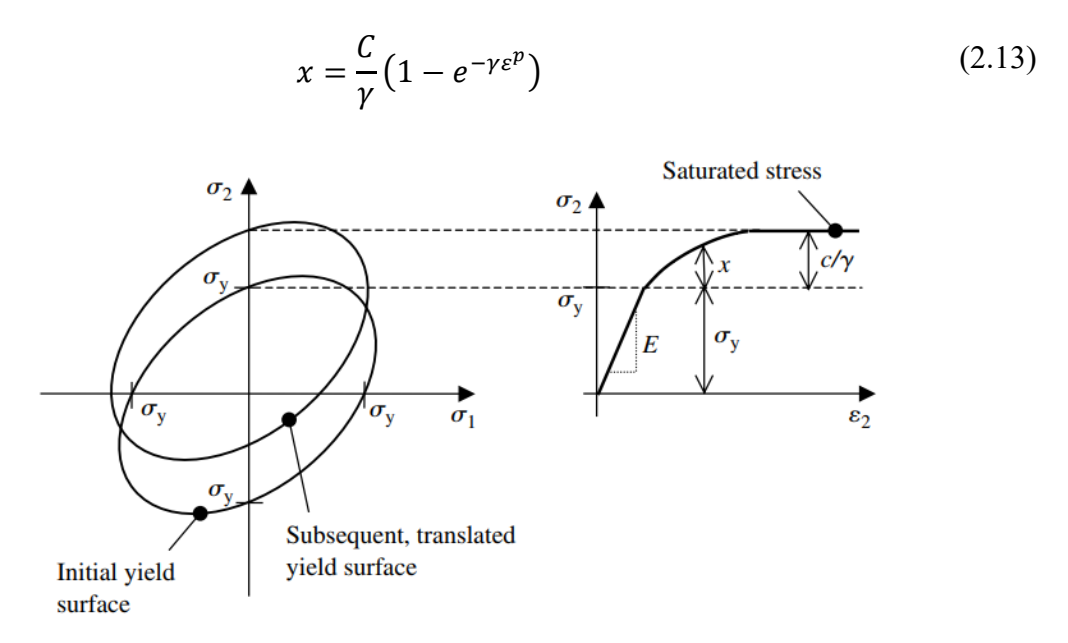


Figure 2.3 Shifting of yield surface and the resulting non-linear kinematic hardening stress-strain curve [80].

Where C and γ are material parameters that are identified from cyclic test data, C is the initial kinematic hardening modulus (rate of increment of back stress at zero plastic strain), and γ is the rate at which kinematic hardening modulus decreases with an increase in plastic deformation (rate of saturation of back stress). C/γ is the saturation value of back stress (α), as shown in Figure 2.3 [79–81].

2.3.3. Expansion and translation of yield surface (combined isotropic and kinematic hardening behavior)

When subjected to cyclic loading conditions, the plastic deformations that occur in materials exhibit several phenomena, such as the Bauschinger effect, cyclic hardening/softening, and ratcheting. The cyclic loading of a material under tension-compression conditions produces hysteresis loops. Furthermore, it is hypothesized that it combines two general hardening theories (i.e., kinematic and isotropic hardening) [79–81]. The Chaboche model [18] is the simplest model that combines two theories for simulating strain-controlled cyclic loading. In which kinematic hardening dominates within a cycle, and with successive cycling, the material also hardens/softens isotopically. As a result, the

peak stress increases/decreases from one cycle to another until saturation is achieved, as shown in Figure 2.4 [79–81].

The combined form of the Chaboche model for proportional monotonic loading is given by Eq. (2.14)

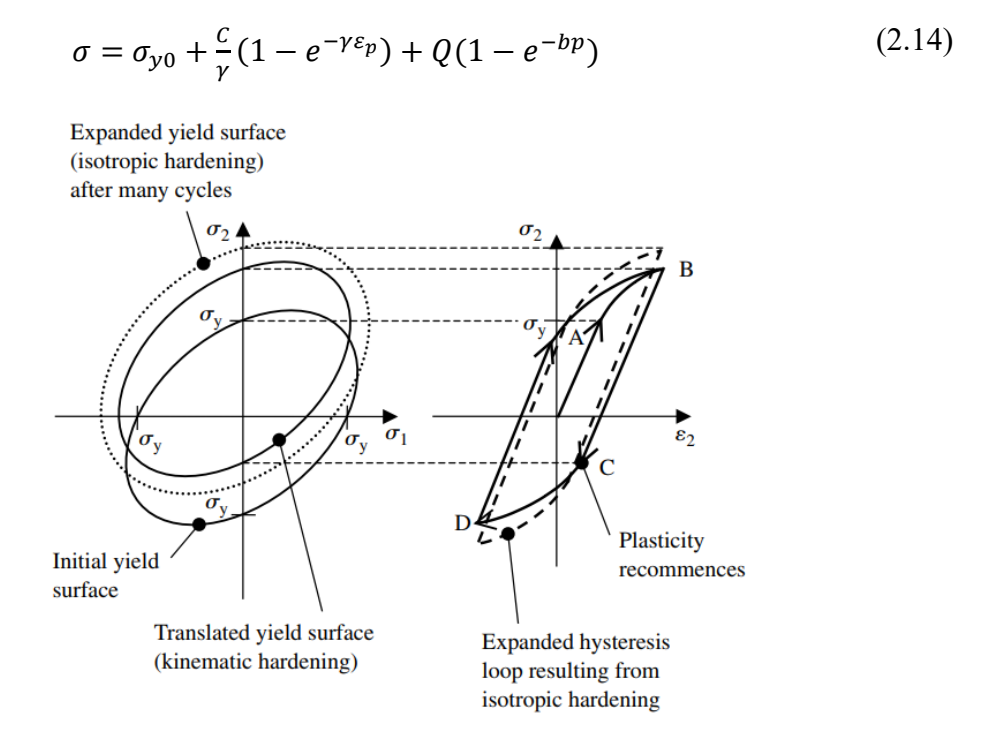


Figure 2.4 Combined non-linear kinematic and isotropic hardening [80].

2.3.4. Time-dependent cyclic plasticity

Irreversible deformation may also happen at stresses below the yield limit if the load is maintained for a long time. This type of deformation is referred to as creep, the magnitude of which is a function of stress, time, and temperature [79–81]. As mentioned in Chapter 1: Section 1.1 and shown in Figure 1.1, the materials used in power plants undergo creep-fatigue loading. The constitutive modeling for this type of loading condition is done through time-dependent plasticity in which the plastic strain and creep strain contribute to the estimate of total strain. The time-dependent constitutive models [79–81] can be classified as

- 1. Unified model
- 2. Non-unified model

2.3.4.1. Unified model

The unified model considers that the total strain is additively decomposed into elastic and inelastic strain [82], where inelastic strain includes both time-dependent (viscous) and time-independent (plastic) strain as a single variable and is given by Eq. (2.15)

$$\boldsymbol{\varepsilon} = \boldsymbol{\varepsilon}_e + \boldsymbol{\varepsilon}_{in} \tag{2.15}$$

The elastic component of the strain tensor obeys Hooke's law [79–81] and is given by Eq. (2.16). The inelastic component of the strain tensor that has time-dependent (creep) and time-independent (plastic) components included together and is given by Eq. (2.17)

$$\boldsymbol{\varepsilon}_{\boldsymbol{\rho}} = \boldsymbol{C}^{-1} : \boldsymbol{\sigma} \tag{2.16}$$

$$\dot{\boldsymbol{\varepsilon}}_{in} = \frac{3}{2} \dot{\lambda} \frac{\sigma' - x}{J_2(\sigma' - x)} \tag{2.17}$$

The inelastic strain rate is given by Eq. (2.18), where K and m are rate dependent viscous material parameters and σ_v is viscous stress, as shown by Eq. (2.19). while $\langle \square \rangle$ is the MaCauley bracket, which means that $\langle y \rangle = 0$, when y < 0 and $\langle y \rangle = y$ when $y \ge 0$.

$$\dot{p} = \left\langle \frac{f}{K} \right\rangle^m \tag{2.18}$$

$$\sigma_v = K \dot{p}^{1/m} \tag{2.19}$$

The Von-Mises yield criteria is given by Eq. (2.20). σ_{y0} is the initial yield stress and $J_2(\sigma' - x)$ is second invariant of the deviatoric stresses.

$$f = I_2(\sigma' - x) - r(p) - \sigma_{v0}$$
 (2.20)

Considering the Chaboche viscoplastic model [32], the non-linear kinematic hardening law (x) with static recovery term, is given by Eq. (2.21) and Voce's [83] isotropic hardening law r(p), is given by Eq. (2.22).

$$\dot{\mathbf{x}} = \frac{2}{3}C\dot{\mathbf{\varepsilon}}^p - \gamma x \,\dot{\mathbf{p}} \tag{2.21}$$

$$r(p) = Q(1 - exp^{-bp}) (2.22)$$

2.3.4.2. Non-unified model

For isothermal loading, the non-unified model considers that the total mechanical strain is additively decomposed into elastic, plastic, and creep strain [82], where plastic

strain includes time-independent effect and creep strain includes time-dependent strain, as given by Eq. (2.23)

$$\varepsilon_m = \varepsilon_e + \varepsilon_p + \varepsilon_c \tag{2.23}$$

2.4. Continuum damage mechanics-based model

In order to simulate the behavior of a material for the whole fatigue process, the material constitutive model could be combined with continuum damage mechanics theory. The damage mechanics theory enables the modeling of the material's strength degradation. Kachanov [84] proposed the "continuing parameter" and stated that a progressive deformation occurs in material that leads to deterioration in the material's mechanical properties.

Lematire [85], Chaboche [32], and many others [86,87] authors in the open literature considered the damage as an intrinsic property of the material, *i.e.*, within the material, the cracks, voids etc, formed and gets oriented in any direction without the effect of any external factors. Thus, they considered the damage variable to be anisotropic fourth-order tensor quantity and simplified the "damage variable (*D*)" as an isotropic, *i.e.*, scalar quantity considering that cracks and voids are distributed equally in all directions. Thus, the elastic coupled damaged law is given by Eq. (2.24).

$$\boldsymbol{\sigma} = (1 - D)\boldsymbol{C}: \boldsymbol{\varepsilon_e} \tag{2.24}$$

 ${\cal C}$ is the elasticity tensor, and ${\varepsilon}_e$ represents the elastic part of the strain.

For high-temperature applications, using the damage D as a scalar variable in the constitutive model combined with the hardening laws is important to predict the material's deterioration. Thus, the evolution of yield criteria is given by Eq. (2.25).

In Eq. (2.25), x represents the back stress, *i.e.*, translation of yield surface. Whereas combined $r(p) + \sigma_{y0}$ shows the expansion of yield surface (σ^0).

$$f = J_2 \left(\frac{\sigma'}{1 - D} - x \right) - r(p) - \sigma_{y0}$$
 (2.25)

The damaged coupled kinematic and isotropic hardening laws are given by Eq. (2.26) and Eq. (2.27), respectively [88]. Eq. (2.27) is proposed by Yaguchi et al. [89] where C and γ are dynamic recovery material parameter while τ and r are static or thermal recovery temperature dependent material parameter. \dot{Y}_i represents the internal variable that

describes the evolution of mean stress. Y_{st} represents the rate/time dependent inelastic deformation.

$$r(p) = Q(1 - exp(-bp))(1 - D)$$
(2.26)

$$\dot{x}_{i} = (1 - D)(\frac{2}{3}C\dot{\varepsilon}_{in} - \gamma(x - Y_{i})\dot{p}) - \tau[J(x)]^{r-1}x$$
(2.27)

where
$$\dot{Y}_i = -\alpha_b (Y_{st} \frac{x_i}{J(x_i)} + Y_{si}) [J(x)]^{r-1}$$
 and $J(x) = \sqrt{\frac{3}{2} x_i : x_i}$

2.4.1. Damage models

2.4.1.1. Empirical models

Many empirical models have been developed to quantify damage under creep-fatigue interaction loading. Most damage prediction models for creep-fatigue interaction loading use the damage summation rule [63–66], which considers the creep and fatigue damages separately. Some of the commonly used models/methods are summarized in Table 2.1.

Table 2.1 Chronological development of damage models for creep-fatigue interaction.

Period	Model / Method	Key equations	Parameter	Data requirement
1950's - 1960's	Ostergren [90]	$D_f = \frac{1}{a_f (\sigma_{max} \Delta \varepsilon^p)^{-\ell_f}}$ $\sigma_{max} \text{ is maximum stress, } \Delta \varepsilon^p \text{ is plastic strain}$	a_f, ℓ_f	Pure fatigue
	Robinson's rule [70]	$D_c = \int_0^{t_h} rac{1}{t_r(\sigma, T_{abs})} dt$ $t_r = \mathcal{L}_r \sigma^{-\ell_r}$	\mathcal{L}_r, ℓ_r	Pure creep
		t_r is rupture time, T_{abs} is temperature, t_h is hold time		

Frequency-based approaches

1970's Coffin [91]
$$D_f = \frac{1}{C_c(\varepsilon_{in})^{\ell_c} f_t^{\varkappa} (f_c/f_t)^{\hbar}} \qquad \begin{array}{c} C_c, \ell_c, \text{ Pure} \\ \varkappa, \hbar & \text{fatigue/} \\ \text{Creep-} \\ \text{fatigue} \\ \text{frequency factor,} \end{array}$$

 ε_{in} is inelastic strain

Halford and Saltsman [92]

$$D = \frac{1}{C_m (\Delta \varepsilon_{in})^{\ell_m}}$$

 C_m ,

Pure fatigue/ Creepfatigue

for (PP, CP, PC, CC) regions

PP is plasticity in both tension compression

CP is creep strain in tension and plastic strain in compression

PP is plastic strain in tension and creep strain in compression

CC creep strain in both tension and compression

Strain-based ductility exhaustion approach

1980's Priest et al. [93]

$$D_{c} = \int_{0}^{t_{h}} \frac{\dot{\varepsilon}_{in}}{\varepsilon_{f}(\dot{\varepsilon}_{in}, T_{abs})} dt$$
$$\varepsilon_{f} = \mathcal{L}_{p} \dot{\varepsilon}_{in}^{\ell_{p}}$$

 \mathcal{L}_p, ℓ_p Creepfatigue

 ε_{in} is inelastic strain, ε_f is strain at rupture, T_{abs} is temperature

Strain energy-based ductility exhaustion approaches

2000's Takahashi *et* al. [75]

Present

$$D_{c} = \int_{0}^{t_{h}} \left(\frac{1}{\widetilde{w}_{f}(\dot{w}_{in}, T_{abs})} - \frac{1}{\widetilde{w}_{f0}(T_{abs})} \right) \dot{w}_{in} dt$$

Pure \emptyset, δ . \widetilde{W}_{f0} fatigue, creepfatigue,

> pure creep

 $\dot{w}_{in} = \sigma \dot{\varepsilon}_{in}$

$$\widetilde{w}_f = \min(\emptyset \dot{w}_{in}^{\delta}, \widetilde{w}_{f0}(T_{abs}))$$

 \dot{w}_{in} is inelastic strain energy density rate, \tilde{w}_f is the function of inelastic strain energy density, \widetilde{w}_{f0} is the upper bound of \widetilde{w}_f , T_{abs} is temperature

Wang et al. [76]

$$D_{c} = \int_{0}^{t_{h}} \left(\frac{1}{\widetilde{w}_{f}(\dot{w}_{in}, T_{abs})} - \frac{1}{\widetilde{w}_{f0}(T_{abs})} \right) \dot{w}_{in,new} dt$$

Pure

fatigue, creepfatigue,

> pure creep

 $\dot{w}_{in,new} = \frac{M}{1+t} - \frac{N}{1+t} \log(1+t)$

$$M = \frac{\sigma_o(Plog(\Delta \varepsilon^p) + Q)}{E.ln10} \left(\frac{\sigma_m}{\sigma_0} + 1\right)$$

$$N = \frac{(Plog(\Delta \varepsilon^p) + Q)^2}{E_e ln 10}$$

 $\dot{w}_{in,new}$ is inelastic strain energy density rate, \tilde{w}_{f0} is the upper bound of \tilde{w}_f , T_{abs} is temperature, σ_o is maximum stress, σ_m is mean stress

Song et al. [78]
$$D_{c} = \int \left(-\frac{A}{(1+t)\ln(10)Ew_{f}} \right) dt \qquad a_{a}, a_{b} \text{ fatigue,}$$

$$-\frac{A}{w_{f,max}(\dot{w},T)} dt \qquad E \qquad \text{fatigue,}$$

$$A = \left(M + \frac{2Nlog(1+t)}{\ln(10)} \right) (\sigma - \sigma_{th}) \qquad \text{creep}$$

$$M = a_{a}\log(\Delta\varepsilon^{p}) + a_{b} \qquad N = b_{a}\log(\Delta\varepsilon^{p}) + b_{b}$$

$$w_{f} \text{ is creep fracture strain energy density,}$$

$$w_{f,max} \text{ is maximum creep fracture strain energy density,}$$

$$w_{f,max} \text{ is maximum creep fracture strain energy density,}$$

$$w_{f,max} \text{ is maximum creep fracture strain energy density,}$$

$$\text{threshold stress, } E \text{ is elastic modulus, } t \text{ is time}$$

Most of these methods rely heavily on extensive data from pure creep, pure fatigue, and creep-fatigue interaction tests and often overlook the impact of oxidation. Since oxidation becomes significant at high temperatures, there is scope for improving these models by incorporating the oxidation effect.

2.4.1.2. Continuum damage models

Although continuum damage mechanics (CDM) models remain more computationally intensive than purely empirical approaches, they have rapidly increased adoption because they account for load history and provide a rigorous description of material deterioration. Many empirical cycle based damage laws, as shown in Table 2.1, can be recast within a CDM framework as long as their evolution laws satisfy the requirement of non-negative energy dissipation (thermodynamic admissibility) [86,94]. In CDM theory, the scalar damage variable (*D*) grows monotonically from 0 (undamaged) to 1 (fully damaged), earning it the name continuum or continuous damage parameter [95–97]. The damage variable *D* is calibrated directly from macroscopic property changes, such as, reductions in elastic modulus, shifts in cyclic plastic response, variations in ultrasonic wave speed, accelerated creep strain rates, micro-hardness loss, or evolution of strain-energy density etc. [95,98–101]. A few of the most widely used constitutive damage models for creep-fatigue interaction are shown in Table 2.2. In the context of creep-fatigue

interaction loading, the damage variable (D) is typically governed by the combined effects of creep and fatigue damages, as explained by Eq. (2.28), (2.29), and (2.30) [85–87,102,103]. Any one of these three equations can be used, where Eq. (2.28) considers one to one mapping of creep and fatigue damage contribution combined, while Eq. (2.29) considers the independent contribution of creep and fatigue damages, and Eq. (2.30) further considers the non-linear mixing of the independent creep and fatigue damages with the addition of f_{cf} term.

$$dD = f_f(\boldsymbol{\sigma}, T, D_c + D_f)dN + f_c(\sigma_e, T, D_c + D_f)dt$$
(2.28)

$$dD = f_f(\boldsymbol{\sigma}, T, D_f)dN + f_c(\sigma_e, T, D_c)dt$$
(2.29)

$$dD = f_f(\boldsymbol{\sigma}, T, D_f)dN + f_c(\sigma_e, T, D_c)dt + f_{cf}(\boldsymbol{\sigma}, \sigma_e, D_f, D_c)dN$$
(2.30)

Table 2.2 Continuum damage mechanics models for creep-fatigue interaction.

Period	Model	Key equations	Parameter
1960's	Rabotnov and Kachanov [104,105]	$f_c = \frac{R_v}{(1-D)^{\alpha_r}} \left(\frac{\sigma_e}{\lambda_r}\right)^{r_r} \dot{p}$ $R_v = \frac{2}{3} (1+v) + 3(1-2v) \left(\frac{\sigma_{hyd}}{\sigma_e}\right)^2$ $R_v \text{ is multiaxial factor, } \sigma_{hyd} \text{ is hydrostatic stress, } \sigma_e \text{ is}$	r_r , λ_r , α_r
1990's	Lemaitre and Chaboche [106]	equivalent stress, ν is Poisson's ratio. $f_f = \frac{R_v}{\Omega_l(\beta_l + 1)} \frac{\left(\frac{\Delta \varepsilon^p}{2}\right)^{\gamma_l + 1}}{(1 - D)^{\alpha_l}}$ $R_v = \frac{2}{3}(1 + \nu) + 3(1 - 2\nu)\left(\frac{\sigma_{hyd}}{\sigma_e}\right)^2$	$egin{aligned} \gamma_l, \ \Omega_l, \ eta_l, \ lpha_l \end{aligned}$
	Liu and Murakami	R_v is multiaxial factor, σ_{hyd} is hydrostatic stress, σ_e is effective stress, $\Delta \varepsilon^p$ is plastic strain $f_c = \frac{A_m (1 - e^{-q_m})}{q_m} [\sigma_d(t)]^{r_m} \exp(q_m D)$	$A_m,$ $q_m,$

$$\sigma_{d}(t) = \kappa_{m} \left(\frac{3}{2}\sigma'_{ij}:\sigma'_{ij}\right)^{1/2} + (1 - \kappa_{m}) \sigma_{I} \qquad \kappa_{m},$$

$$\sigma_{I} \text{ is maximum principal stress}$$

$$2000's \quad \text{Pandey et} \\ - \quad \text{al. [108]} \qquad f_{f} = \frac{A_{p}\left(1 - e^{-\psi_{p}}\right)}{\psi_{p}} \left(\frac{(1 - R_{\varepsilon})\varepsilon_{max,eq}}{2 - (1 - R_{\varepsilon})\varepsilon_{max,eq}}\right)^{\beta_{P}} e^{a_{p}D} R_{v}^{0.5\beta_{P}} \qquad \psi_{p},$$

$$\varepsilon_{max,eq} \text{ is the maximum equivalent strain} \qquad \beta_{P}$$

Although the above models are widely used, these models require a lot of material parameters, which are obtained from pure fatigue, pure creep and creep-fatigue interaction tests. To address this limitation, the inelastic strain energy density based continuum damage variable *D* is proposed in the literature [99–101,109,110]. Based on this, the present thesis adopts a continuum damage variable *D* using modified tensile hysteresis strain energy density method, as discussed in Chapter 6:.

2.5. Numerical implementation of the constitutive model

The constitutive relations are mathematically implemented in the finite element method using an implicit backward or explicit forward integration scheme [79–81]. In the explicit forward scheme, the flow direction is calculated at the start of the incremental step [79–81]. The integration scheme is conditionally stable, *i.e.*, when the time step is kept very small, but it may have convergence issues if the time step or load is increased [79–81], *i.e.*, stress falls outside the yield surface. The implicit integration scheme is used [79–81] to overcome this issue, in which the stress is corrected/updated at the end of the current increment step to fall on the yield surface. Thus, the method is unconditionally stable and does not have any convergence issues [79–81]. However, the accuracy of the results is still dependent on the time step of the incrementation [79–81].

The flow diagram for the return mapping integration scheme for implementation of the (UMAT, *i.e.*, the constitutive model developed in the current study) is depicted in Figure 2.5. The previous step is taken as N while the incrementation is done from N to N+1 step. As stated above, in the flow algorithm, the values needed from the previous incrementation step (*i.e.*, N) are recalled and stored in memory as state variables defined in ABAQUS. (Note: Strain, stress and back stress are shown in Voigt notation, as used for implementation in ABAQUS user subroutine).

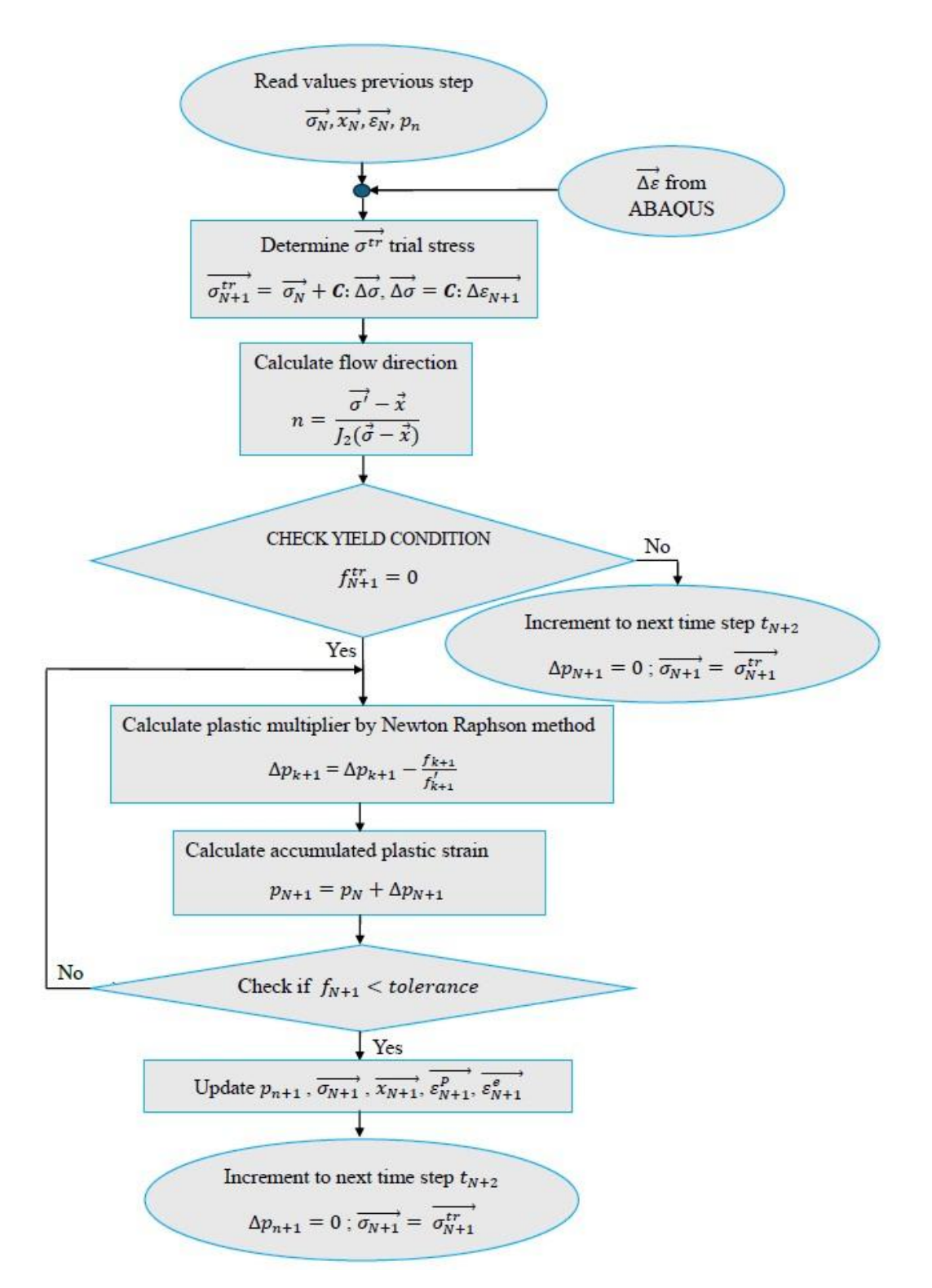


Figure 2.5 Flowchart of radial-return implicit integration scheme for implementation of UMAT

The additive decomposition of strain is considered, which states that total strain is the summation of elastic and plastic strains [80].

$$\overrightarrow{\varepsilon_{N+1}} = \overrightarrow{\varepsilon_{N+1}^e} + \overrightarrow{\varepsilon_{N+1}^p} \tag{2.31}$$

The whole of the total strain at the beginning of an increment is considered as an elastic strain, which is written as elastic strain obtained from the previous step N added with incremental strain ($\Delta \varepsilon$) for step N to N+1[111].

$$\overrightarrow{\sigma_{N+1}^{tr}} = \overrightarrow{\sigma_N} + \mathbf{C} \overrightarrow{\Delta \varepsilon} \tag{2.32}$$

Where $\overrightarrow{\sigma^{tr}}$ represents the trial stress, and \boldsymbol{c} is the elasticity tensor matrix for the material. The incremental strain $(\Delta \varepsilon)$ is obtained from ABAQUS.

$$\overrightarrow{x_{N+1}} = \overrightarrow{x_N} \tag{2.33}$$

Here, x represents the total back stress.

$$\overrightarrow{\varepsilon_{N+1}^p} = \overrightarrow{\varepsilon_N^p} \tag{2.34}$$

 ε^p represents the plastic strain tensor.

$$\Delta p_{N+1} = \Delta p_N \tag{2.35}$$

 Δp_{N+1} represents the increment in effective plastic strain tensor.

The flow direction represented by \vec{n} is given by Wilkins [112] for metals *i.e.* for the associated flow rule, which states the normality condition, plastic strain increment is always normal to yield surface and is given by Eq. (2.36)

$$\vec{n} = \frac{\overrightarrow{\partial f}}{\partial \sigma} \Delta p_{n+1} \tag{2.36}$$

Yield condition (f(p)) is checked for the nonlinear isotropic and kinematic hardening model. The function is given by Eq. (2.37) [80], which states that material is elastic if the state of stress lies inside the yield surface i.e. if f < 0, else the state of material is considered as plastic.

$$f(p) = J_{2}(\vec{\sigma} - \vec{x}) - r(p) - \sigma_{v}$$
 (2.37)

The consistency condition and yield condition together give the increment in the effective plastic strain at the end of the increment step is given as Δp_{k+1} as

$$\Delta p_{k+1} = \Delta p_k - \frac{f(p)}{f'(p)} \tag{2.38}$$

Where f(p) is yield condition at step N+1. and f'(p) represents the derivative of the yield condition at step N+1.

Accumulated plastic strain is given as

$$p_{N+1} = p_N + \Delta p_{N+1} \tag{2.39}$$

Eq. (2.40) gives the increment in the plastic strain tensor.

$$\overrightarrow{\Delta \varepsilon_{N+1}^p} = \vec{n} \Delta p_{N+1} \tag{2.40}$$

If the convergence criterion is met, *i.e.*, the increment in effective plastic strain becomes less than the tolerance value, which is taken as a very small value (1×10^{-10}) than the iteration for calculating the effective increment in plastic strain is stopped. Then, the elastic and plastic strains, back stress, and elastic stress are updated using the closet point projection method, which states that if the state of stress due to incrementation falls outside the yield surface, it is projected back on the yield surface. Thus, the stress state is made to fall back on the yield surface.

Elastic strain is updated as

$$\overline{\varepsilon_{N+1}^e} = \overline{\varepsilon_N^e} - \overline{\Delta \varepsilon_{N+1}^p}$$
(2.41)

Plastic strain is updated as

$$\overrightarrow{\varepsilon_{N+1}^p} = \overrightarrow{\varepsilon_N^p} + \overrightarrow{\Delta \varepsilon_{N+1}^p} \tag{2.42}$$

Stress is updated as

$$\overrightarrow{\sigma_{N+1}} = \overrightarrow{\sigma_{N+1}^{tr}} - C\left(\overrightarrow{\Delta \varepsilon_{N+1}^{p}}\right) \tag{2.43}$$

Chapter 3: Modified isotropic and kinematic hardening equations for 304L SS under low cycle fatigue.

This chapter is on the simulation of the low cycle fatigue behavior of 304L SS that exhibited initial hardening, softening, saturation, and significant secondary hardening. The combined non-linear isotropic and kinematic hardening model has been modified, implemented in ABAQUS, and validated with experimental results. New non-dimensional functions were introduced in the constitutive laws such that both isotropic and kinematic hardening behaviors depend on the accumulated plastic strain and maximum plastic strain range memory. The proposed isotropic hardening equation additively decomposes the cyclic hardening behavior into hardening, softening, and secondary hardening parts and captures well the cyclic peak stress variation throughout the fatigue life. Fatigue life is well predicted from the simulated loops.

3.1. Introduction

The field of computational plasticity has emerged significantly with the advancement of computers. It is widely used for analysis and design in many disciplines. It has reduced extensive experimentation and physical modeling in everyday engineering applications [113]. A similar trend has also been observed in the field of fatigue analysis. Constitutive modeling and simulation have been extensively used for the fatigue analysis of materials and structures.

Generally, two hypotheses considered in combined form to predict the non-linear hardening behavior exhibited by material under cyclic loading are isotropic hardening and kinematic hardening. The isotropic and kinematic hardenings hypothesize the expansion and simultaneous translation, respectively, of the yield surface. It is assumed that kinematic hardening governs the shape of the hysteresis loop, and isotropic hardening governs the change in the maximum/peak stress that varies from one cycle to another [79].

The most commonly used constitutive law to model cyclic plasticity is the Armstrong and Fedrick (AF) model [114]. It considers the non-linearity in the kinematic hardening part using an additional dynamic recovery term in Prager's rule [36]. Further, to capture the transient hardening evolution and ratcheting effects, the back stress in the AF model [114] is decomposed into multiple parts by Chaboche [18]. Ohno and Wang [42] further modified the kinematic hardening equation given by Chaboche [18] to capture the

effect of ratcheting more precisely by introducing a new dynamic recovery term. The dynamic recovery term gets activated when the material reaches a critical state. Further, many modifications were made to the kinematic hardening term to accurately capture the uniaxial and multiaxial ratcheting strain of material by Abdel-Karim and Khan [53], McDowell [115], Jiang and Sehitoglu [44], and Chen *et* al. [43].

The constitutive laws discussed above could not model cyclic hardening/softening with stabilization or persistent cyclic hardening after stabilization exhibited by some material under cyclic loading. Thus, Chaboche et al. [116] considered the maximum plastic strain range memory effect on isotropic hardening variables to simulate the cyclic stress-strain response of such materials. The asymptotic isotropic hardening variable was defined based on the largest plastic strain range history by considering a new index function representing a hypersphere. For the same purpose, Ohno et al. [42] modified the non-hardening region to capture the effect of loading histories. They assumed that isotropic hardening does not occur when plastic strain is located inside a non-hardening range. Nouailhas et al. [46,117] introduced a memory evanescence term in memory surface to consider the anisotropic hardening in multiaxial loading. Khutia et al. [47], Taleb et al. [118], and Zhang and Jiang [52] considered the strain range memory effect on isotropic hardening variables. They modeled the cyclic stress-strain response of materials that undergo hardening followed by softening. They used modified isotropic equations and could capture the variation in peak stress but not the loop shape.

Marquis [81] considered the peak back stress variation with the number of cycles to consider the loop shape change and found that the variation is similar to that of the peak stress amplitude. Tanaka [119], Jiang and Kurath [120,121], and Kang *et* al. [122] have incorporated the plastic strain memory effect in both isotropic and kinematic hardening to capture the hardening and softening effects.

Xu et al. [123] studied the cyclic behavior of low-yield point steel (BLY160) and observed a 'flattening effect,' i.e., the decrease in elastic domain with reduced stress amplitude. To model this 'flattening effect,' they considered the yield surface contraction/expansion and translation through a transformation zone consisting of an S-shaped logistic function. Their model uses 23 material parameters to simulate the cyclic hardening, softening, and saturation behaviors. Later, in [49], they reported that the low yield point steel (BLY160) exhibits non-masing behavior. Hence, the stress-strain loop shape changes with cycling from the 1st to the 100th cycle. Thus, the kinematic hardening

rate and isotropic hardening parameters were considered to be dependent on the strain range memory. The modified model they developed uses a total of 34 material parameters. The kinematic hardening rate was further regarded as dependent on the accumulated plastic strain with an asymptotic function.

Zhu et al. [124] studied the behavior of 316L under thermo-mechanically coupled cyclic loading and proposed a model by considering the strain range memory effect in isotropic hardening. They modified the isotropic part of the basic elastic-viscoplastic Chaboche constitutive model [32] to represent the hardening followed by softening. Xing et al. studied [125] the LCF behavior of 316L comprising of cyclic hardening followed by softening behavior exhibited by the material under different strain amplitudes. They have considered that the change in peak stress i.e., hardening followed by softening occurs with cycling and strain amplitude, is due to isotropic hardening only. They have used the strain range memory-dependent modified isotropic hardening equation to model the material using more than 40 material parameters. Zhou et al. [51] studied the behavior of two austenitic stainless steels (316L-A and 316L-B). The material 316L-A demonstrated initial hardening followed by softening, while the 316L-B demonstrated initial hardening followed by softening and secondary hardening at higher strain amplitude. They claimed to have developed the numerical model to simulate the initial hardening, softening, and secondary hardening by considering a φ term in the kinematic hardening law of the Armstrong-Fedrick model [114]. Their model uses a total of 30 material parameters. The strain range memory dependence is considered in the kinematic hardening part only. The experiment results were compared with the simulation for 316L-A (which shows no secondary hardening). They demonstrated that change in loop shape and variation in peak/valley stress is addressed well for the material. However, their article did not report a similar validation for the 316L-B material that exhibited initial hardening followed by softening and secondary hardening at higher strain amplitude.

Song et al. [13] have modified Chaboche's non-linear isotropic-kinematic hardening rule to develop a constitutive model using 23 material parameters to predict the hardening, softening, and secondary hardening behavior of 316H steel. They modified the isotropic hardening rule with two exponential terms and one linear term and the kinematic hardening rule using ψ and μ terms to incorporate the effect of accumulated plastic stain on back stress. They validated their model by comparing their simulated results with the experimental data. However, it should be noted that the secondary hardening demonstrated

by 316H is almost negligible, close to the saturated response. Thus, developing a model that can simulate a significant amount of secondary hardening is still required.

As reported above, a material can demonstrate some (or all) of the cyclic features like initial hardening, softening, saturation, and secondary hardening. The classical and modified models developed to date lack the ability to address the cyclic behavior comprising all four features. Thus, there is still a need for a constitutive model to describe the cyclic behavior of materials irrespective of the sequence of the cyclic features exhibited. This chapter proposes the modified kinematic and isotropic hardening laws to model the aforementioned cyclic features. A new non-dimensional function, ζ , is introduced in the isotropic and kinematic hardening equations to account for the significant change in the secondary hardening behavior through maximum plastic strain range memory (q). Moreover, another function, φ_{KH} , was introduced to account for the dependence of maximum back stress on strain amplitude. Thus, the proposed model considers the isotropic and kinematic hardening to be dependent on the accumulated plastic strain and maximum plastic strain range memory. The proposed constitutive model is validated with the straincontrolled low-cycle fatigue test data of 304L SS material. The comparison of the experimental and simulated results shows that the developed constitutive model can predict the cyclic behavior of the investigated steel that exhibited initial hardening, softening, saturation, and significant secondary hardening very satisfactorily. The proposed model predicts the variation of the entire stress-strain hysteresis loops, i.e., change in a loop shape and variation in peak & valley stresses with good agreement.

3.2. Cyclic behavior

3.2.1. Cyclic peak stress

The strain-controlled low cycle fatigue test data of 304L SS material were analyzed. The chemical composition (in % wt.) of the material is C: 0.029, Si: 0.46, Mn: 1.74, Ni: 8.17, Cr: 18.16, N: 0.061, P: 0.033, S: 0.004, and balanced Fe. The test specimens with a gauge diameter of 10 mm and a length of 28 mm were prepared as per ASTM E606 [126]. Tests were conducted at room temperature at a constant strain rate of 1×10^{-3} s⁻¹ and strain amplitudes of $\pm 0.4\%$, $\pm 0.6\%$, $\pm 0.8\%$, and $\pm 1\%$. It is observed that the cyclic peak stress shows initial hardening followed by softening and significant secondary hardening at higher strain amplitude. While at lower strain amplitude, the material exhibited initial hardening followed by significant softening, saturation, and secondary hardening, as shown

in Figure. 3.1. This type of behavior of austenitic stainless steel is reported in the open literature [51,116,118]. It is observed that the life spent during the secondary hardening period is almost 73%, 80%, 90%, and 91% at strain amplitudes of $\pm 0.4\%$, $\pm 0.6\%$, $\pm 0.8\%$, and $\pm 1\%$, respectively. Thus, the constitutive modeling of secondary hardening, along with initial hardening, softening, and saturation behavior, has practical importance for materials like 304L SS.

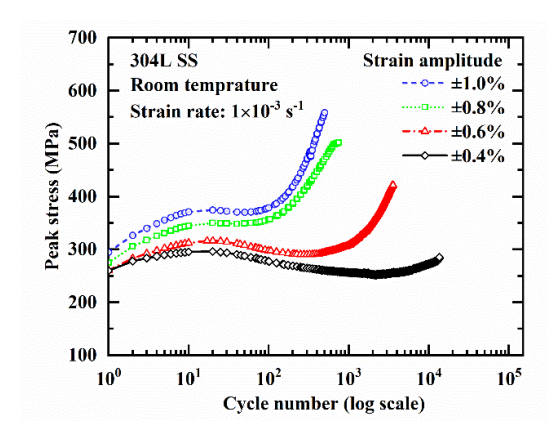


Figure. 3.1. Peak stress variation with cycle number.

The half-life stress-strain (%) loops of 304L SS are translated to match the upper loading portions in Figure. 3.2. As can be seen, despite all efforts, only the linear parts could be matched, not the non-linear parts of all hysteresis loops. The increase in the linear elastic region can be seen in Figure. 3.2, *i.e.*, an increment from AB to AC for the increment of strain amplitude from $\pm 0.4\%$ to $\pm 1\%$. In constitutive modeling, the increase in the elastic domain is taken into account by expanding the yield surface. Thus, the isotropic hardening equation needs to be modified to take care of this behavior [49]. Moreover, the change in loop shape with strain amplitude becomes evident in Figure. 3.2. Such changes in loop shape are taken into account by translation of the yield surface. Thus, the kinematic hardening equation also needs to be modified to take care of this behavior [127]. The modified isotropic and kinematic hardening equations are explained in detail in Section 3.3.

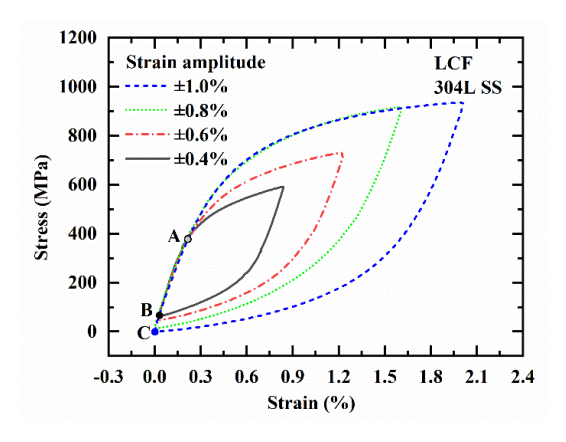


Figure. 3.2. Translated stress vs. plastic strain loops of 304L at half-life to match the linear elastic portions.

3.2.2. Microstructural deformation

During cycling, the initial hardening occurs due to the interaction of dislocations with solute atoms, grain boundaries, other dislocations, and their multiplication [128,129]. The softening (that follows initial hardening) is due to the re-arrangement of dislocation cells or the annihilation of dislocations [129,130]. The secondary hardening occurs due to the increased density of defects like dislocations, stacking faults, twins, and austenite to martensite transformation responsible for the material's non-masing behavior [16,126]. The austenite has a face-centered cubic (FCC) structure, while the martensite can have a bodycentered tetragonal BCT (BCC: body-centered cubic) or hexagonal close-packed (HCP) crystal structure. The conversion of austenite to BCT (BCC) martensite during deformation-induced transformation leads to volume increment [131], which causes the development of back stress in the material. Thus, the yield stress gets reduced in the compressive direction [131]. Hence, the kinematic hardening variables need to be modified to accommodate such an increase in back stress. Also, due to the reduction in the active number of slip systems in BCT and HCP structures than FCC, the martensite phase is harder than austenite [132]. Hence, martensite formation leads to a change in the isotropic hardening. Thus, the strain range of cyclic loading affects both isotropic and kinematic hardening.

3.3. Modified constitutive laws

3.3.1. Isotropic hardening

The isotropic hardening law used in the combined non-linear isotropic and kinematic hardening model [18] to predict the change in peak stress from one cycle to

another is given by Voce's law [133], as shown in Eq. (3.1). This equation predicts either continuous cyclic hardening or cyclic softening with high accuracy. However, a material under fatigue can exhibit different extents and sequences of hardening, softening, saturation, and secondary hardening regions before the final fracture occurs. Thus, the isotropic hardening equation needs to be modified to accommodate such variations commonly found in different materials under fatigue, *e.g.*, Figure. 4.2. shows for 304L SS. Various modifications to the isotropic hardening equation were suggested by Chaboche *et* al. [116], Taleb and Cailletaud [134], Pécheur *et* al. [135], Zhu *et* al. [50], Xu *et* al. [49], Krishna *et* al. [45], and Song *et* al. [13]. These suggested modifications can accommodate only the variation in initial hardening, softening followed by transient stabilization and/or negligible secondary hardening.

The cyclic peak-stress response curves at different strain amplitudes for 304L SS, fatigue tested at room temperature, are shown in Figure. 3.1. The peak stress vs. accumulated plastic strain is plotted in Figure. 3.3. The peak stress vs. accumulated plastic strain plots is split into three parts: initial hardening (R_1) , softening (R_2) , and saturation and/or secondary hardening (R_3) , as shown in Figure. 3.3.

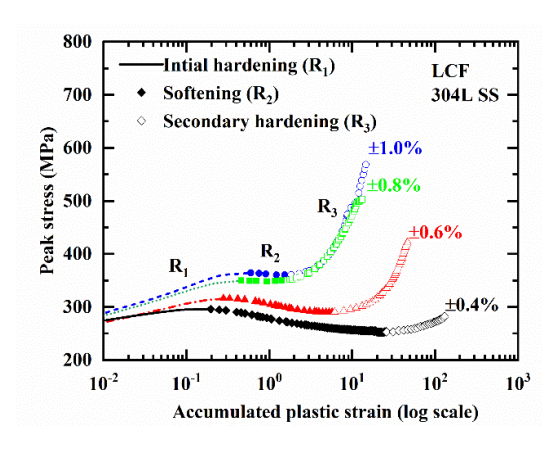


Figure. 3.3. Peak stress vs. accumulated plastic strain curves.

The variation in yield surface size (σ^0) , *i.e.*, the peak effective stress with cycling can be related to isotropic hardening (r(p)) as given by Eq. (3.2) [136–140] for the classical model. The parameter σ_{y0} represents the initial size of the yield surface. The variation in yield surface size with accumulated plastic strain has a similar trend as of peak stress vs. accumulated plastic strain, as seen in Figure. 3.4. Thus, the variation in yield surface size with accumulated plastic strain is also split into three parts: initial hardening (R_1) , softening (R_2) , and saturation and/or secondary hardening (R_3) , as shown in Figure. 3.4.

$$r(p) = Q(1 - exp^{-bp}) (3.1)$$

$$\sigma^0 = r(p) + \sigma_{v0} \tag{3.2}$$

The concept of Eq. (3.2) is applied to the different regions to derive the proposed isotropic hardening equations. The extent of the initial hardening region is approximately up to the initial 20 cycles for different strain amplitudes, as can be seen in Figure. 3.1. This region (R_1) is plotted by lines of different styles in Figure. 3.4. The asymptotic behavior of the initial isotropic hardening region is modeled by using Voce's law [133], as given by Eq. (3.3).

$$r_1(p) = \sigma_{IH}^o - \sigma_{v0} = Q(1 - exp^{-bp}) \tag{3.3}$$

The parameter Q represents the maximum amount of hardening, while b is the rate at which the hardening occurs.

The second part of the isotropic hardening behavior, *i.e.*, the cyclic softening region, is shown by the region R_2 (solid symbol) in Figure. 3.4. We observe that at high strain amplitude ($\pm 1\%$), the softening region of the material is very small. However, it is very long at low strain amplitude ($\pm 0.4\%$), and the peak effective stress decreases exponentially. Thus, the softening behavior (*i.e.*, the second part) of the material is given by Eq. (3.4) in the proposed model.

$$r_2(p) = \sigma_S^o - \sigma_1 = Q_1(1 - exp^{-b_1 p})$$
(3.4)

The transition from initial hardening to the softening region is taken care of by the parameter σ_1 . The parameters Q_1 and b_1 represent the maximum softening and the rate of softening, respectively.

The third part of the isotropic hardening behavior, *i.e.*, the secondary hardening region, is shown by the region R_3 (open symbol) in Figure. 3.4. The peak effective stress varies almost linearly with accumulated plastic strain in this region. It should be noted that the variation apparently looks non-linear because of the linear-log scales used in Figure. 3.4. The secondary hardening region (*i.e.*, the third part) of the material is represented by Eq. (3.5).

$$r_3(p) = \sigma_{SH}^o - \sigma_2 = a_1 p (3.5)$$

The transition from softening to the secondary hardening region is handled by parameter σ_2 . The parameter α_1 represents the rate of the hardening.

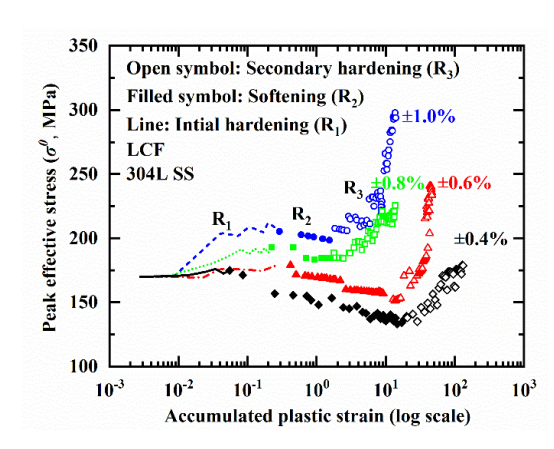


Figure. 3.4. Peak effective stress vs. accumulated plastic strain curves.

It should be noted that the cyclic saturation behavior of the material observed at lower strain amplitude was taken into account by splitting the different regions appropriately and identifying the material parameters accordingly.

The above equations given for initial hardening, softening, and secondary hardening regions are combined to make the single equation (Eq. (3.6)) for isotropic hardening as-

$$r(p) = r_1(p) + r_2(p) + r_3(p) = \sigma_{IH}^o - \sigma_{v0} + \sigma_S^o - \sigma_1 + \sigma_{SH}^o - \sigma_2$$
(3.6)

Which is further rewritten as Eq. (3.7), with an assumption that $\sigma^0 = \sigma_{IH}^o + \sigma_S^o + \sigma_{SH}^o$. The assumption is made because σ_{IH}^o , σ_S^o , and σ_{SH}^o actually represent σ^0 for different regions.

$$r(p) = r_1(p) + r_2(p) + r_3(p) = \sigma^0 - \sigma_{v0} - \sigma_1 - \sigma_2$$
(3.7)

Eq. (3.7) can be rewritten as Eq. (3.8) and Eq. (3.9), which are principally similar to the isotropic hardening (Eq. (3.2)) defined in the non-linear isotropic-kinematic hardening Chaboche model [136–140]. Xing et al. [125] have used an equation similar to Eq. (3.8) to take into account the initial hardening and softening behavior shown by the material. Comparing the equation used by Xing et al. [125] and Eq. (3.8) proposed here, we have included the linear term $r_3(p)$ and σ_2 to consider the secondary hardening region shown by the region R_3 (open symbol) in Figure. 3.4. Also, it should be noted that the equation used by Xing et al. [125] looks similar to Eq. (3.8) proposed here but Eq. (3.8) here takes into account the maximum plastic strain range memory effect differently. This is described in Section 3.3.3.

$$\sigma^0 = r_1(p) + r_2(p) + r_3(p) + \sigma_{v0} + \sigma_1 + \sigma_2 \tag{3.8}$$

$$\sigma^{0} = r(p) + \sigma_{y0} + \sigma_{1} + \sigma_{2} \tag{3.9}$$

3.3.2. Kinematic hardening

The conventional Chaboche [18] model considers the kinematic hardening behavior given by Eq. (3.12), where C_i and γ_i are kinematic hardening material constants, $n=\pm 1$ represents flow direction, $x_{i,0}$ is the backstress obtained at the start of plasticity and Δp is the effective plastic strain increment. The material constants C_i and γ_i in the conventional model [6] remain constant for the whole cyclic life. Thus, the loop shape is assumed to not change from one cycle to another. However, the loop shape changes significantly with cycling for austenitic stainless steels, e.g., 304L SS. Many materials with a similar variation in hysteresis loop shape with cycling have been reported in the articles [126,129,141,142]. Thus, the conventional Chaboche model [18] fails to predict the hysteresis loop shape of all cycles at a particular strain amplitude. Moreover, as explained in Section 3.2 and shown in Figure. 3.2, the change in hysteresis loop shape with strain amplitude due to non-Masing behavior also calls for modification in the kinematic hardening equation. A few researchers have made efforts to model the change in loop shape with cycling [13,51,123,124,127,143], but none of them have demonstrated the applicability of their model to simulate material behavior comprising of all four cyclic features viz-a-viz hardening, softening saturation, and secondary hardening. A significant amount of secondary hardening greatly alters the hysteresis loop shape, as shown in Figure. 3.2. Modeling of such a considerable change in loop shape is highly required to accurately predict the fatigue behavior of austenitic stainless steel or other materials that undergo deformation-induced transformation.

The kinematic hardening is determined by measuring the back stress, which varies with cycling for 304L SS; thus, it depends on the accumulated plastic strain. The dependence of kinematic hardening on accumulated plastic strain is also highlighted by Zhu et al. [124]. They considered the variation of the ratio (φ) of 'maximum back stress at any cycle (x_{max}^N), it is obtained from different stress-strain loops, as explained in Section 3.4.' to the 'maximum back stress at first cycle (x_{max}^1).' with accumulated plastic strain 'p', given by Eq. (3.10). In Eq. (3.10), i represents and M represents total number of region (for example if material shows initial hardening, softening and secondary hardening regions, then M=3). Later, Song et al. [13] also used the same equation (Eq. (3.10)) in their constitutive model to take into account the change in back stress with cycling or accumulated plastic strain.

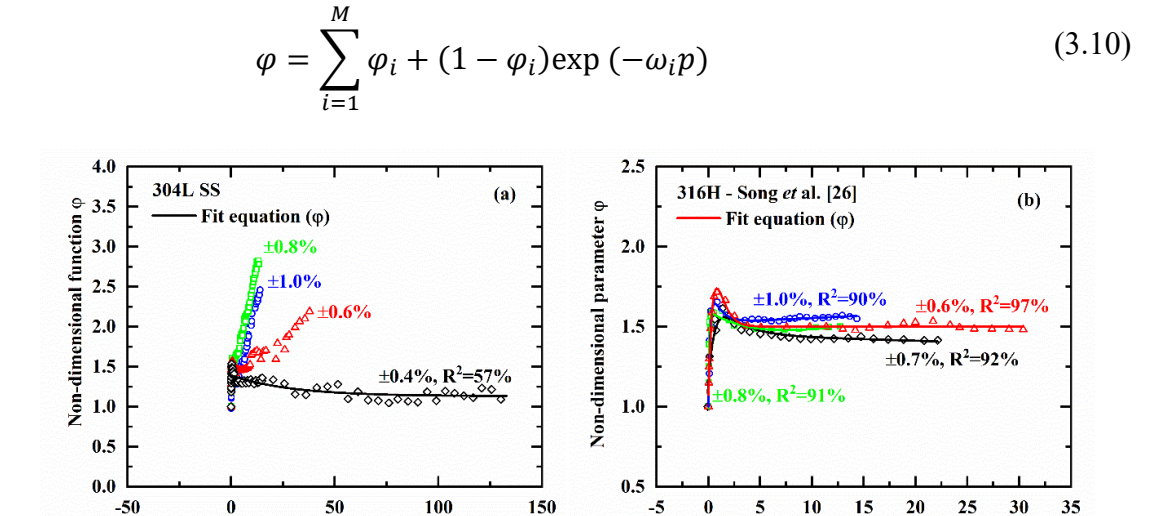


Figure. 3.5. Variation of φ with accumulated plastic strain is fitted with Eq. (3.10) (a) for material 304L SS (b) for 316H (data were extracted from Song *et al.* [13]).

Accumulated plastic strain

Accumulated plastic strain

We tried to fit Eq. (3.10) to the data for 304L SS, but the fit did not converge at higher strain amplitudes, as shown in Figure. 3.5(a). However, the fit converges with 57% of the coefficient of determination (R^2) at a lower strain amplitude ($\pm 0.4\%$). The poor fitting may be attributed to the complex shape of the plots of (φ) caused by the significant amount of secondary hardening, as shown in Figure. 3.5(a). While the 316H material used by Song *et* al. [13] shows negligible secondary hardening (almost like a saturated response) at all strain amplitudes, thereby giving a good fit ($R^2 = 97\%$), as shown in Figure. 3.5(b). The data is plotted in Figure. 3.5 (b) were extracted from the article [13].

Considering the shape of the plots in Figure. 3.5(a), Eq. (3.11) is proposed for φ_{mod} to describe the variation of φ with p. This equation additively decomposes the function into three parts corresponding to the initial hardening, softening, and secondary hardening behaviors. A similar kind of decomposition is used for isotropic hardening as well in Eq. (3.9). As shown in Figure. 3.6 (a & b), the proposed Eq. (3.11) fits well with the data for the 304L SS material used for the current investigation and 316H material used by Song et al. [13] with a coefficient of determination (\mathbb{R}^2) greater than 90%.

$$\varphi_{\text{mod}} = a_2 + a_3(1 - e^{-a_4 p}) + a_5 + a_6(1 - e^{-a_7 p}) + a_8 + a_9 p$$
 (3.11)

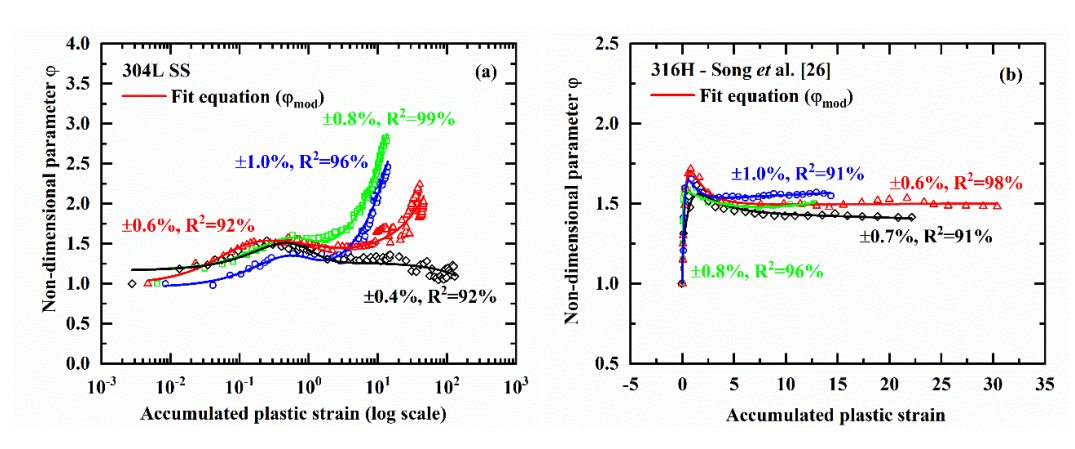


Figure. 3.6. Variation of φ with accumulated plastic strain is fitted with Eq (3.11) (a) for material 304L SS (b) for 316H (data were extracted from Song *et* al. [13]).

Chaboche's non-linear kinematic hardening equation, given by Eq. (3.12), is modified to take into account the dependence of the kinematic hardening law on the accumulated plastic strain, as shown by Eq. (3.13). The increasing value of φ_{mod} with accumulated plastic strain causes hardening, while decreasing value of φ_{mod} causes softening.

$$x = \sum_{i=1}^{3} (\boldsymbol{n} \, C_i / \gamma_i) + \left(\left(\boldsymbol{x}_{i,0} - \boldsymbol{n} \, C_i / \gamma_i \right) e^{-\gamma_i \Delta p} \right)$$
 (3.12)

$$\dot{\mathbf{x}} = \varphi_{mod} \frac{2}{3} C_i \dot{\boldsymbol{\varepsilon}}_p - \gamma_i \mathbf{x} \, \dot{p} \tag{3.13}$$

3.3.3. Plastic strain range memory effect

As shown in Figure. 3.4 and Figure. 3.6(a), the shape of the plot's changes significantly with strain amplitude due to the secondary hardening. And, the linear terms $\sigma_2 + a_1 p$ in Eq. (3.8) for isotropic hardening and $a_8 + a_9 p$ in Eq. (3.11) for kinematic hardening take care of the secondary hardening region that depends on the accumulated plastic strain (p). Thus, these two linear terms or parts of the isotropic and kinematic hardening equations have been modified to incorporate the plastic strain range memory effect such that a single set of material parameters can be used to define the cyclic behavior of the material.

For that purpose, a non-dimensional parameter, ζ , is defined by Eq. (3.14).

$$\zeta_{i} = \left(\frac{\Delta \sigma_{PSH_{i}}}{\left(\left(\sum_{i=1}^{n} \Delta \sigma_{PSH_{i}}\right)/n\right)}\right) / \left(\frac{\Delta p_{SH_{i}}}{\left(\left(\sum_{i=1}^{n} \Delta p_{SH_{i}}\right)/n\right)}\right)$$
(3.14)

Here $\Delta \sigma_{PSH}$ is the change in peak stress due to secondary hardening only (i.e., in the region R_3 in Figure. 3.3), Δp_{SH} is the accumulated plastic strain in the secondary hardening region only, n is the number of tests performed at different strain amplitudes, and the integer i varies from 1 to n. The parameter ζ gives a non-dimensional estimate of the secondary hardening with respect to accumulated plastic strain. Thus, ζ may be called a cyclic secondary hardening rate.

The parameter ζ is estimated for 304L SS from the data given in Figure. 3.3 for different strain amplitudes and plotted as a function of the maximum plastic strain range (q) in Figure. 3.7. Interestingly, the plot is found to follow an S-shaped growth curve, which can be defined by the relationship in Eq. (3.15), in which a_{10} , a_{11} and a_{12} are material parameters.

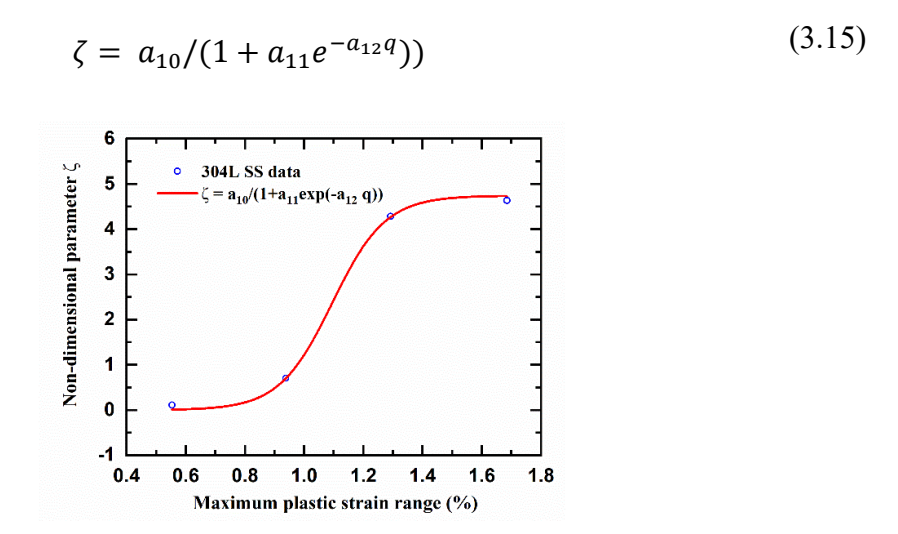


Figure. 3.7. Variation of ζ with maximum plastic strain range (%).

Now, with the help of the parameter, ζ , the isotropic and kinematic hardening equations (Eq. (3.9), Eq. (3.11), and Eq. (3.13)) have been modified to make them maximum plastic strain range memory dependent, as shown by Eq. (3.16), Eq. (3.17) and Eq. (3.18).

$$\tilde{\sigma}^0 = \sigma^0 + (\zeta - 1)a_1 p \tag{3.16}$$

$$\tilde{\varphi} = \varphi_{mod} + (\zeta - 1)a_9p \tag{3.17}$$

$$\dot{\mathbf{x}} = \tilde{\varphi} \frac{2}{3} C_i \dot{\boldsymbol{\varepsilon}}_{\boldsymbol{p}} - \gamma_i \boldsymbol{x} \, \dot{\boldsymbol{p}} \tag{3.18}$$

As shown in Figure. 3.2 and discussed in Section 3.2.13.2.1, the hysteresis loop shape changes significantly with strain amplitude, such that the upper loading branches do

not match with one another. To take into account such changes with strain amplitude, the normalized maximum back stress (denoted by φ_{KH}) is plotted with the maximum plastic strain range (q), as shown in Figure. 3.8. The normalization of the maximum back stress is done by dividing the values with the maximum back stress at the highest strain amplitude. The dependence of φ_{KH} on maximum plastic strain range (q) could be defined by Eq. (3.19) and is implemented in the constitutive model, as shown by Eq. (3.20).

$$\varphi_{KH} = a_{13} + a_{14}e^{a_{15}q} \tag{3.19}$$

$$C_i/\gamma_i = \varphi_{KH}C_i/\gamma_i \tag{3.20}$$

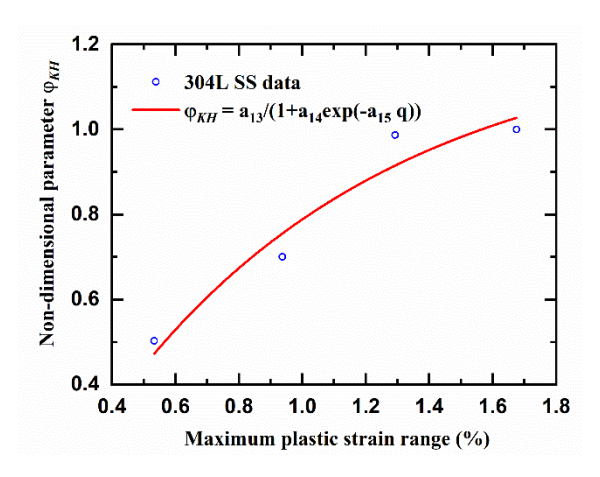


Figure. 3.8. Variation of φ_{KH} with maximum plastic strain range (%).

The modified equations (Eq. (3.15) to Eq. (3.20)) have been implemented in the constitutive model with the help of the plastic strain memorization equations given by Chaboche *et* al. [116].

3.4. Material parameter identification

The yield stress (σ_{y0}) and elastic modulus (E) are calculated from the 1st cycle of the stress-strain hysteresis loops, as shown schematically in Figure. 3.9. The peak effective stress (σ^0) for each cycle is estimated from the linear portion of the stress-strain hysteresis loops. The maximum back stress (x_{max}) is calculated from the peak stress (σ_{max}) by subtracting the peak effective stress (σ^0) . The parameter φ_{mod} is calculated as the ratio of 'maximum back stress at any cycle (x_{max}^N) ' to the 'maximum back stress at first cycle (x_{max}^1) .'

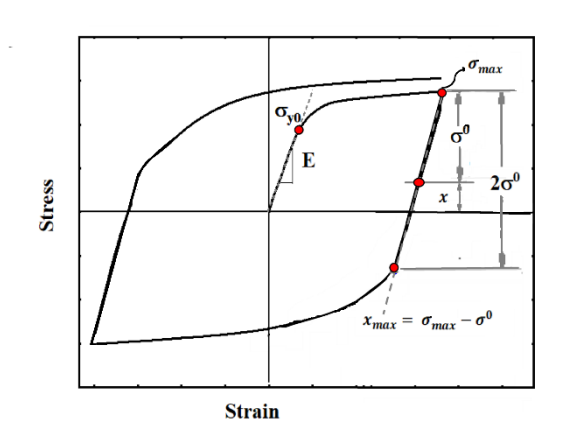


Figure. 3.9. Schematic diagram showing the determination of elastic modulus (E), yield stress (σ_{y0}) , peak effective stress (σ^0) and maximum back stress (x_{max}) .

3.4.1. Isotropic hardening parameters

The isotropic hardening function requires the determination of a total of 11 parameters, out of which three parameters are for initial hardening given by Eq. (3.3), three parameters are for softening given by Eq. (3.4), and another two parameters are for secondary hardening region defined by Eq. (3.5), and three parameters for plastic strain range dependence given by Eq. (3.15). The constant σ_y is the stress at zero plastic strain, *i.e.*, the yield stress. According to their definition, the constants σ_1 and σ_2 , were determined directly from the peak effective stress vs. accumulated plastic strain plots. The remaining parameters of isotropic hardening were determined by fitting Eq. (3.9) to the experimental data, as shown in Figure. 3.10. The isotropic hardening parameters used in the modified non-linear isotropic hardening law were defined as the average values of the parameters obtained at different strain amplitudes. The strain range memory parameters associated with Eq. (3.15) have been determined using the data given in Figure. 3.7. The values of isotropic hardening parameters used are shown in Table 1.

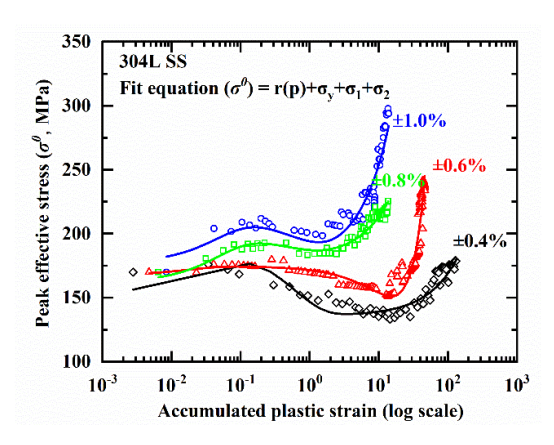


Figure. 3.10. Determination of isotropic hardening material parameters for different strain amplitudes by fitting Eq. (3.9).

3.4.2. Kinematic hardening parameters

As discussed in Section 3.3.2, the change in hysteresis loop shape with cycling is defined by kinematic hardening laws given by Eq. (3.17), Eq. (3.18), Eq. (3.19), and Eq. (3.20) considering 13 parameters. Among these, the C_i/γ_i defines the maximum value of hardening that can be achieved in a cycle, while γ_i gives the rate of hardening. For the conventional Chaboche [18] model, the back stress for the stabilized cycle is given by Eq. (3.21) [144].

$$x^S = \sigma^S \pm \sigma_{v0} \pm Q^S$$
, S represents the stabilized cycle (3.21)

Using the above formula, the back stress x for the N^{th} cycle can be defined as

$$\boldsymbol{x}^{N} = |\boldsymbol{\sigma}^{N}| - \sigma_{y} - \sigma_{1} - \sigma_{2} - r(p)^{N}$$
(3.22)

$$r(p)^{N} = r_{1}(p)^{N} + r_{2}(p)^{N} + r_{3}(p)^{N}$$
(3.23)

Where σ^N is the stress for N^{th} cycle obtained from the experimental data and x^N is the maximum back stress in N^{th} cycle.

The back stresses were calculated from the first hysteresis loop at the largest strain amplitude ($\pm 1.0\%$) using Eq. (3.22). Then the parameter C_i and γ_i were obtained by fitting Eq. (3.12) to the back stress vs. plastic strain data.

To incorporate the loop shape change with cycling, the constants a_2 to a_9 were obtained by fitting Eq. (3.11) to the data plotted in Figure. 3.6(a) for different strain amplitudes. As the strain range memory effect is taken into account by the modified equations (Eq.(3.15), Eq. (3.17), and Eq. (3.20)), the average values of the parameters (a_2)

to a_9) obtained at different stain amplitudes have been used as the single set of parameters defining the kinematic hardening behavior of the material. The values of the material parameters are shown in Table 3.1

To take into account the significant change in loop shape with strain amplitude, as discussed in Section 3.3.3, the material parameters a_{13} , a_{14} , and a_{15} were obtained by fitting Eq. (3.19) to the data shown in Figure. 3.8.

Table 3.1. Material parameters for 304L SS

	$E = 187.609 \text{ GPa}, \nu = 0.3$
Isotropic	$\sigma_{yo} = 170 \text{ MPa}, Q = 34.81 \text{ MPa}, b = 19.96, \sigma_1 = 197.69 \text{ MPa},$
	$Q_1 = -44.57 \text{ MPa}, b_1 = 1.33, \sigma_2 = -204.78 \text{ MPa}, a_1 = 5.233$
ζ	$a_{10} = 4.9332 \ a_{11} = 2.98156 \times 10^5, \ a_{12} = 11139.812$
Kinematic	$C = 57345.81 \text{ MPa}, \ \gamma = 378.9$
Memory surface	$\eta = 0.95$
$oldsymbol{arphi}_{ ext{modified}}$	$a_2 = 1$, $a_3 = 1.157$, $a_4 = 3.326$, $a_5 = 1.527$, $a_6 = -1.057$, $a_7 = 1.654$, $a_8 = -1.369$, $a_9 = 0.106$
$arphi_{\mathit{KH}}$	$a_{13} = 1.2281, \ a_{14} = -1.40281 \ a_{15} = -1160.4116$

3.5. Simulation details

The proposed model has been implemented in the finite element analysis code ABAQUS through a user material subroutine (UMAT) using the radial-return algorithm and the Newton-Raphson iteration algorithm. The radial return integration scheme is used to implement the (UMAT) as explained in Section 2.4.1 and depicted in Figure 2.5. The 3D model with a cubic geometry of 35 mm is used for simulations. A three-dimensional 8-noded linear brick element (C3D8) [145] [146] was considered for the simulation, as shown in Figure. 3.11. The model was subjected to displacement-controlled cyclic loading with a triangular waveform. Displacements of ± 0.14 , ± 0.21 , ± 0.28 , and ± 0.35 mm were applied to induce strain of $\pm 0.4\%$, $\pm 0.6\%$, $\pm 0.8\%$, and $\pm 1.0\%$ of amplitudes, respectively. The displacement was applied on the right surface of the cube, while the opposite (left) surface was constrained to not move along the direction of the applied load. Also, the rotational movement was restricted in all directions. Two adjacent edges on the left surface were

constrained to deform along their lengths only, while the other two edges were left free to move in any direction on that surface. This constraint prevents rigid body translation of the whole model.

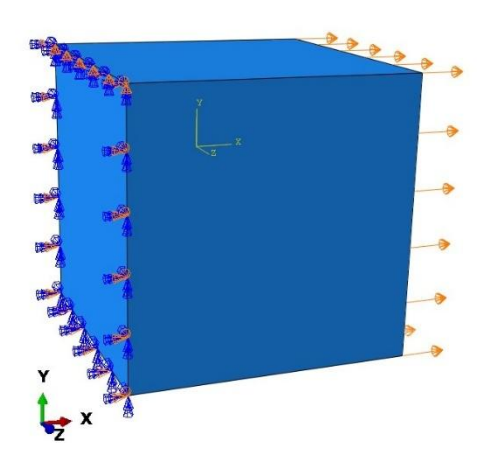


Figure. 3.11. The 3D model used for the simulation.

3.6. Results and discussion

The proposed constitutive model, along with the modified isotropic and kinematic hardening equations, has been implemented in ABAQUS with the help of a user subroutine (UMAT). The model has been validated with the low cycle fatigue test data of 304L SS for $\pm 0.4\%$, $\pm 0.6\%$, $\pm 0.8\%$, and $\pm 1.0\%$ of strain amplitudes.

3.6.1. Variation in cyclic peak stress

The variation in cyclic peak stress with the number of cycles for experimental and simulated results is shown in Figure. 3.12. As can be seen, the model predicts the variation in cyclic peak stress with high accuracy for the initial hardening, softening, saturation, and secondary hardening regions at all strain amplitudes. Thus, the proposed model could accurately predict the cyclic stress response of the material for the whole life.

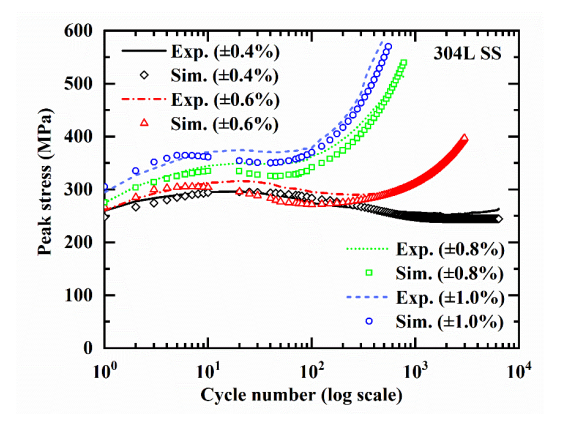


Figure. 3.12. Comparison of peak stress variation with cycle number.

3.6.2. Hysteresis loop shape

The accurate prediction of hysteresis loop shape becomes essential while performing the numerical prediction of material behavior. The comparison between the simulated and experimental loops is shown in Figure. 3.13 for all strain amplitudes. For clarity in visualization, the second cycle is shown, and one loop from each of the primary hardening, softening, and secondary hardening regions is plotted. For ±0.4% strain amplitude, one cycle from the saturation region (3000) is also shown in Figure. 3.13(a). As shown in Figure. 3.13, the prediction of the hysteresis loop shape is considerably good throughout fatigue life. The estimate of cyclic plastic strain energy density (CPSED), *i.e.*, the area inside the hysteresis loop, gives a quantitative measure of the hysteresis loop prediction. The comparison of the CPSEDs of the experimental and simulated hysteresis loops in Figure. 3.13 is demonstrated in Figure. 3.14. As can be seen, the deviation in the CPSEDs is considerably less (<10%) in all the regions at all strain amplitudes, except for ±0.6% strain amplitude in the secondary hardening region.

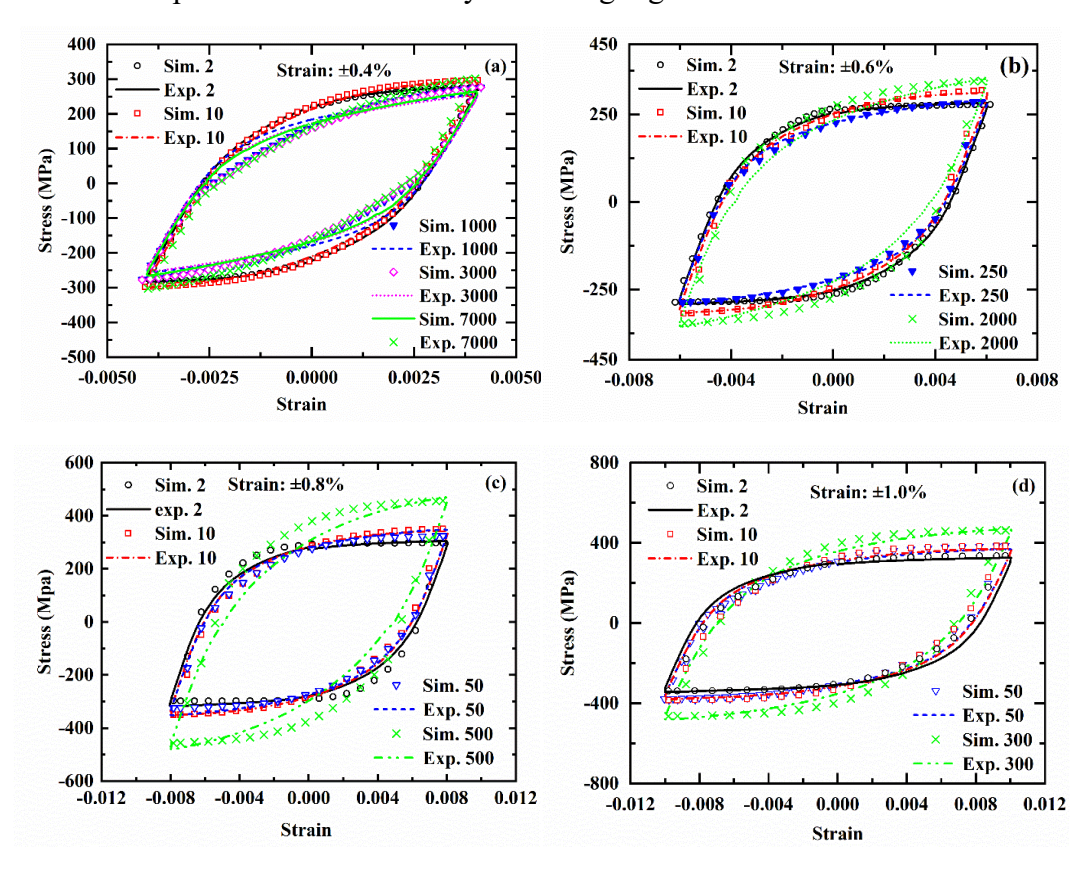


Figure. 3.13. Comparison of experimental and simulated hysteresis loops for different strain amplitudes: (a) $\pm 0.4\%$, (b) $\pm 0.6\%$, (c) $\pm 0.8\%$, and (d) $\pm 1.0\%$. The hysteresis loops for the second cycle (\circ), initial hardening region (\square), softening (\blacktriangledown), saturation (\diamond), and secondary hardening (\times) regions are shown. The actual cycle numbers are highlighted in the figures.

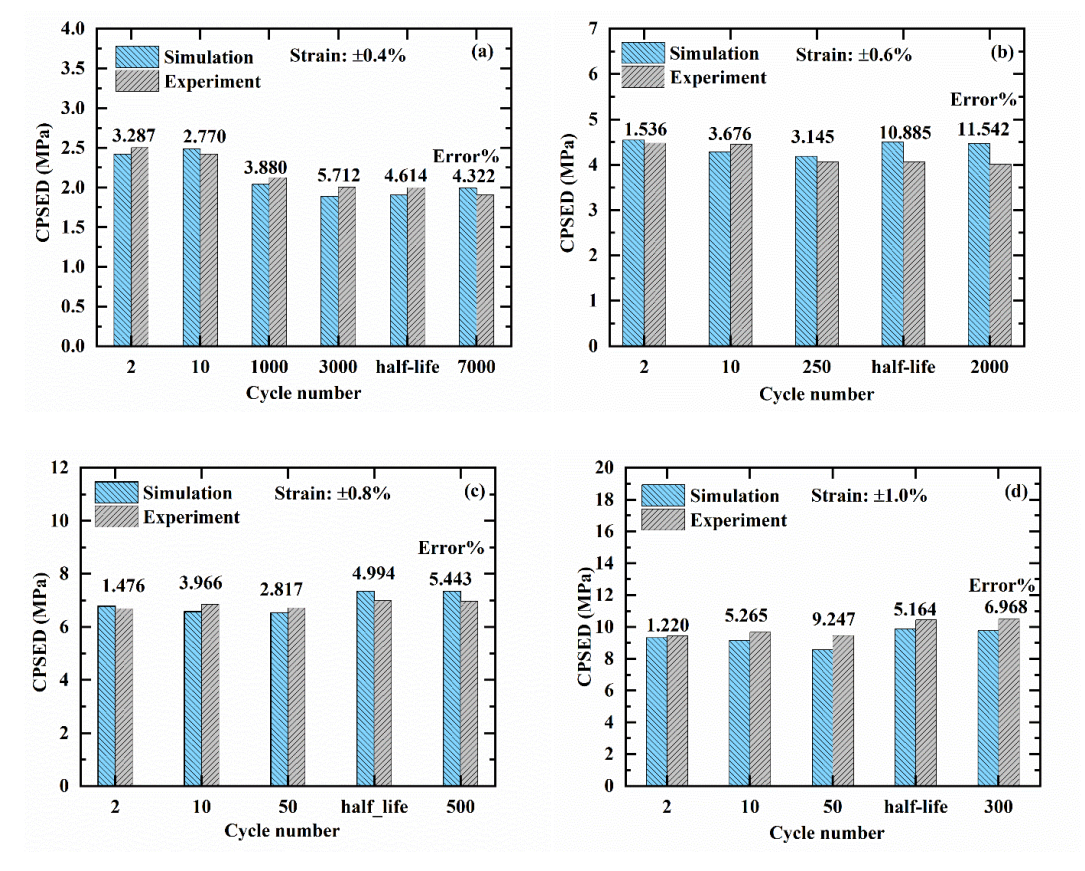


Figure. 3.14. Comparison of the cyclic plastic strain energy densities (CPSEDs) of the experimental and simulated hysteresis loops for strain amplitudes of (a) $\pm 0.4\%$, (b) $\pm 0.6\%$, (c) $\pm 0.8\%$, and (d) $\pm 1.0\%$. The error percentages are shown above the bars.

3.6.3. Fatigue life prediction

The primary objectives of constitutive modeling and simulation are to study the fatigue response of an actual component with complex geometry and predict the life and possible location of damage initiation. Conventionally, the fatigue life prediction is made using empirical relationships proposed by Basquin [147] and Coffin-Manson [148], which utilize the relationship between stress or strain and fatigue life. However, if we consider a material's response under cyclic loading, the strain energy density is a more fundamental parameter as it inherits the effect of both stress and strain. Thus, the estimation of CPSED forms the basis of the strain energy-based fatigue life prediction methods [126,149]. Conventionally, the CPSED of the half-life or stabilized hysteresis loop is considered a representative estimate of the fatigue behavior of a material [150]. Figure. 3.15 shows a comparison of the half-life hysteresis loops of the fatigue tests conducted at different strain amplitudes. It also highlights the ability of the constitutive model to predict the material's cyclic behavior.

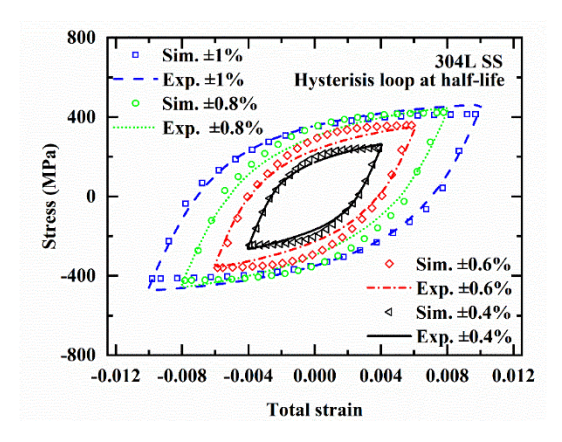


Figure. 3.15. Comparison of half-life hysteresis loops of different strain amplitudes.

For the estimation of fatigue life, various researchers have used the power-law relation between fatigue life (N_f) and CPSED (W) [126,151], which is given by Eq. (3.24)

$$W = K_1(N_f)^{\alpha} \tag{3.24}$$

Where K_1 and α are material constants; are estimated to be 413.841 MPa and -0.580, respectively, for the 304L SS, as shown in Figure. 3.16.

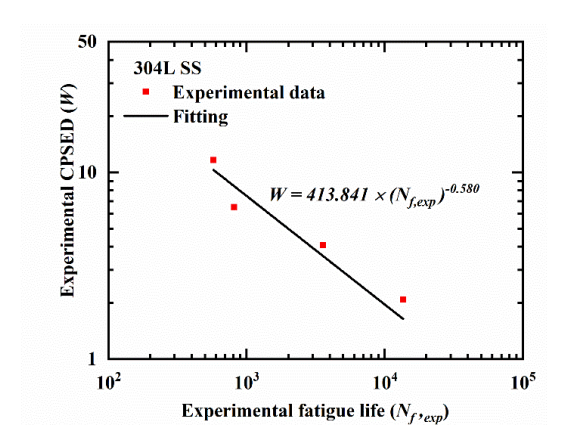


Figure. 3.16. Experimental cyclic plastic strain energy density (CPSED) is estimated from the data in Figure. 3.15 is plotted with fatigue life ($N_{f,exp}$).

Using the power-law relationship (Eq. (3.24)), estimated material constants (K_1 and α), and the CPSEDs of the simulated half-life hysteresis loops, the fatigue lives at different strain amplitudes have been computed and compared in Figure. 3.17. As can be seen, the fatigue life could be predicted within a scatter factor of 1.5.

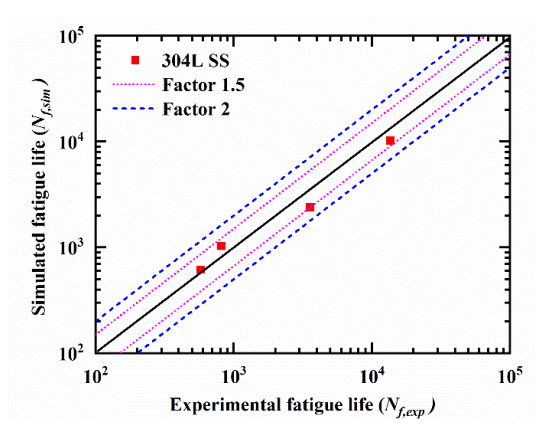


Figure. 3.17. Comparison of experimental and simulated fatigue lives.

3.7. Conclusions

The new modified isotropic and kinematic hardening equations have been proposed to simulate materials' low-cycle fatigue response that exhibits initial hardening, softening, saturation, and secondary hardening behaviors. The proposed model additively decomposes the isotropic hardening equation into cyclic hardening, softening, and secondary hardening parts. The cyclic hardening and softening behaviors were defined by Voce's exponential-type relationship, and the secondary hardening was represented by a linear relationship. For the kinematic hardening, two new non-dimensional functions have been introduced to Choboche's non-linear kinematic hardening equation to account for the loop shape change that occurs with cycling and strain amplitude due to the non-Masing behavior of materials.

The model has been implemented in the commercial finite element analysis code ABAQUS as a user-defined subroutine (UMAT) and validated with the low cycle fatigue test data of 304L SS, fatigue tested at $\pm 0.4\%$, $\pm 0.6\%$, $\pm 0.8\%$, and $\pm 1.0\%$ of strain amplitude at room temperature. The proposed model could predict the whole cyclic deformation behavior of the material with high accuracy. Estimates of the cyclic plastic strain energy densities and comparison of the hysteresis loops at different life fractions highlight the same.

The proposed model uses 26 material parameters to simulate the whole cyclic behavior of the material, *i.e.*, initial hardening, softening, saturation, and secondary hardening. However, most of the models available in the open literature use more than 23 parameters, and up to 32 also, for simulating material behavior consisting of initial hardening, softening, and saturation only. Further, the fatigue life prediction based on the cyclic plastic strain energy densities of the simulated hysteresis loops is found to lie within a scatter factor of 1.5.

Chapter 4: Type-I and Type-II non-Masing behaviors of materials under low cycle fatigue: constitutive modeling and simulation

In Chapter 1: Section 1.2, we have discussed that stainless steels under straincontrolled low cycle fatigue (LCF) exhibit complex cyclic deformation behavior consisting of cyclic hardening, softening, secondary hardening, etc., and have proposed the modified isotropic and kinematic hardening equations that depend on the accumulated plastic strain and maximum plastic strain range memory to numerically predict the aforementioned behaviors. However, this complex cyclic deformation influences the material's Masing/non-Masing behavior. Recent studies classify the non-Masing behavior into Type-I and Type-II. No studies in the literature have demonstrated the applicability of constitutive models for simulating both Type-I and Type-II non-Masing behaviors exhibited by materials. To address the issue, the materials 321 SS exhibiting 'non-Masing Type-I' and 304L SS showing 'non-Masing Type-II' under LCF are selected for this study. In this chapter, we proposed a general constitutive model by modifying the isotropic and kinematic hardening laws to predict the Type-I and Type-II non-Masing behaviors of materials under LCF. The modified constitutive laws include dependence on the strain range memory effect (for the whole life or part of the material's life), accumulated plastic strain, and transient back stress effect. The agreement between experimental data and simulated results suggests that the proposed model works well in predicting the cyclic deformation behavior for both materials. Thus, the proposed model is believed to be applicable in modeling the cyclic deformation behavior of other materials.

4.1. Introduction

Many investigations have been carried out to understand and numerically model/simulate the different behaviors of materials, as highlighted in Table 4.1. The numerical models available in the open literature can predict the cyclic behavior exhibiting either 'Masing' or 'non-Masing Type-I'. No article in the literature has demonstrated (or validated) any constitutive model for simulating materials' Type-I and Type-II non-Masing behaviors. Thus, in this chapter, modified isotropic and kinematic hardening equations are proposed to simulate the Type-I and Type-II non-Masing behaviors of materials under LCF.

The proposed constitutive model has been validated with LCF test data of two materials, 321 SS and 304L SS, which exhibit Type-I and Type-II non-Masing behaviors, respectively.

From the constitutive modeling perspective, the cyclic deformation behavior of the materials fundamentally varies in terms of the changes in loop shape (*i.e.*, kinematic hardening), proportional stress limit (*i.e.*, isotropic hardening), and strain range dependencies. The strain range dependency manifests itself in terms of strain amplitude's effect on the translation and/or expansion of the yield surface under cyclic loading. It is taken into account by the strain range memory effect in constitutive modeling. Chaboche et al. [152,153], Nouailhas et al. [46], and Mc Dowell [154] have considered the strain range memory effect in the expansion of yield surface to model the peak stress variation. Zhou et al. [51], Krishna et al. [45], Song et al. [13], and Kang et al. [155] have considered the same in the translation of yield surface to model the loop shape as well as peak stress variation. Further, Ohno and Kachi [156,157], Xu et al.[49], Das et al. [158], Yang et al. [11], and Wang et al. [12] have considered the strain range memory effect for both translation and expansion of yield surface together.

In a previous article [159], we proposed modified isotropic and kinematic hardening laws to simulate the cyclic hardening, softening, saturation, and significant secondary hardening behavior of 304L SS under LCF at room temperature. The strain range memory effect was considered for the secondary hardening (SH) behavior only. The modifications proposed in [159] predict secondary hardening well. However, the current investigation aims to further improve the modeling of overall cyclic behavior, especially considering the strain range memory effect for the cyclic softening behavior. This is specifically important for materials like 321 SS that show significant variation in the cyclic softening rate with strain amplitude. The proposed model in this article considers the strain range memory effect for both the cyclic hardening and softening behaviors, thus enhancing its applicability for various materials. In open literature, it is reported that many stainless steels under straincontrolled low cycle fatigue (LCF) exhibit strain range dependence behavior throughout their life or for some part of their life [11]. The proposed model considers the strain range memory effect for the translation and expansion of the yield surface with the help of a nondimensional function, ζ . Also, the identification of material parameters and optimization methods are highlighted to improve cyclic prediction. The proposed constitutive model is implemented in ABAQUS as a user subroutine (UMAT) for simulating the LCF behavior of 304L SS and 321 SS materials. The excellent agreement between experimental data and simulated results suggests that the proposed model works well in predicting the cyclic deformation behavior of the materials.

Table 4.1 Cyclic behavior of some materials used in nuclear and thermal power plants and their constitutive model.

S No.	Material and applications	Behavior under strain- controlled fatigue	Constitutive model developed to simulate the same/other materials with similar behavior
1.	304 Pipe structures (elbow) [160]	 At room temperature and low strain amplitude: Stage I: Continuous cyclic softening At high strain amplitude: Stage I: Cyclic hardening Stage II: Saturation [18,121] *Exhibits non-Masing Type-I [121] 	 Chaboche [18] (Only continuous cyclic hardening or softening) Ohno and Kachi [156,157] (Ohno and wang model) Krishna et al. [45] (Modified Chaboche et al. model including stain memory effect. Only peak stress is modeled accurately, not loop shape) Nouailhas et al. [46] (316 SS: Cycling hardening at high strain amplitude and softening at decreasing strain level test. Only peak stress is modeled accurately, not loop shape) Zhang and Jiang [52] (Polycrystalline copper: Cyclic hardening and softening, both peak stress and loop shape are modeled accurately)
2.	SS 316Ti (Alloy D9)	At 600 °C and low strain amplitude: Stage I: Continuous cyclic hardening	• Chaboche and Rousselier [152,153,164]

	Pressurized capsule Clad and wrapper tubes [161,162].	• At high strain amplitude: Stage I: Cyclic hardening Stage II: saturation [163] **Masing/non-Masing: could not be determined	• Xie et al. [165] (316L: Shows cyclic hardening followed by saturation)
3.	316LN Reactor main vessel, inner vessel, and out-core components [161,166]	 At 550 °C and low strain amplitude: Stage I: Continuous cyclic hardening (consists of two distinct regions) At high strain amplitude: Stage I: Cyclic hardening Stage II: Softening [167] * Exhibits non-Masing Type-I [167] 	• Chen et al. [168].
4.	316H High temperature gas cooled reactor [169]	• At 550 °C and ±0.6% to ±1% strain amplitude: Stage I: Cycling hardening Stage II: Softening Stage III: Continued softening/negligible secondary hardening [13] * Exhibits non-Masing Type- I [13]	 Song et al. [13] (Model validated for negligible secondary hardening) Hu et al. [170] (Considering different temperatures, the model is validated with negligible secondary hardening)
5.	304H AUSC- Final stage Super heater tubing/rehea	• At room temperature and ±1% strain amplitude: Stage I: Cycling hardening Stage II: Softening Stage III: Saturation [173]	 Xu et al. [49]. (BLY160: Cyclic hardening and softening followed by saturation) Zhong et al. [174]. (Q235: Cyclic hardening followed by saturation at low strain

	ter tubes [171,172]	**Masing/non-Masing: could not be determined	amplitude and hardening followed by softening at high strain amplitude)
6.	347H AUSC- Superheater/ reheater tubes [175– 177]	 At room temperature and ±0.4% to 1.2% strain amplitude: Stage I: Cycling hardening Stage II: Softening [176,177] **Masing/non-Masing: could not be determined 	 Zhou et al. [51] Yang et al. [11] (316L: Cyclic hardening followed by softening)
7.	316L Condenser tubes and intermediate heat exchanger tubes [161]	• At room temperature and ±0.3% to 1.5% strain amplitude: Stage I: Cycling hardening Stage II: Softening [51] * Exhibits non-Masing Type-I [11,51]	 Zhou et al. [51] Yang et al. [11]
8.	SA 333 Nuclear piping material for primary heat transport [158]	 At room temperature and low strain amplitude: Stage I: Softening Stage II: Softening Stage III: Hardening At high strain amplitude: Stage I: Hardening Stage II: Hardening Stage III: Ha	• Das <i>et</i> al. [158]

9.	Mod. 9Cr- 1Mo AUSC- Boiler membrane wall superheater, reheater tubing[171]	At room and high temperature: Stage I: Cycling softening Stage II: Saturation [179] * Exhibits non-Masing Type-I [179]	 Chaboche and Rousselier [138,152,153] Zhang et al. [57] Wang et al. [62] (P92: Cyclic softening and saturation)
10.	2.25CrMoV AUSC-main steam pipelines, hydrogenate d reactors [11]	 At high (455 °C) temperature: Stage I: Cycling softening Stage II: softening [11] * Exhibits Masing behavior [11] 	• Yang et al. [11]
11.	Inconel 617 AUSC-final stage superheater tubing/rehea ter tubes [171]	 At high (700 °C) temperature and low strain amplitude: Stage I: Continuous cyclic hardening At high strain amplitude: Stage I: Cyclic hardening Stage II: Softening Stage II: Accelerated softening [12] * Exhibits non-Masing Type- I [12] 	• Wang <i>et</i> al. [12]
12.	Inconel 750H	• At high (750 °C) temperature: Stage I: Cyclic hardening	• Song <i>et</i> al. [13]

	AUSC-	Stage II: Softening [13]	
	boiler tubes,	* Exhibits Masing behavior	
	steam	[179]	
	header, and		
	transfer		
	pipes [3]		
13.	316 SS Detector	At room temperature and low strain amplitude:	• Chaboche <i>et</i> al. [116,117] (Cyclic hardening/softening
	sheath	Stage I: Cyclic hardening	and saturation are considered in the model)
	[180], automatic	Stage III: Softening	Ohno and Kachi [156,157] In the above articles, only peak
	droplet dispensing	Stage III: SaturationAnd, at high strainamplitude:	stress variation is modeled accurately, not loop shape.
	system [181]	Stage I: Cyclic hardening	Hormzi [183] (Cyclic hardening and saturation)
		Stage II: Softening/saturation Stage III: Secondary hardening [182]	Xu et al. [49] (BLY160: Cyclic hardening followed by softening and saturation)
		* Exhibits non-Masing Type-I [182]	Mehani and Roy [159] (304L: Strain range memory effect is not considered in cyclic softening)
14.	304LN Colder pipes [166],	• At room temperature and strain amplitude up to 1.2%:	Khutia <i>et</i> al. [185]. (Note: considered only cyclic hardening and softening)
	Safety vessels [161]	Stage I: Cycling hardening Stage II: Softening	Mehani and Roy [159] (304L: Strain range memory effect is not considered in cyclic
		• At higher strain amplitude (>1.2%)	softening)

		Stage I: Cycling hardening Stage II: Softening Stage III: Secondary Hardening [178,184] * Exhibits non-Masing Type- II [178,184]	
15.	304L AUSC- heat exchanger tube shell [186]	• At room temperature and ±0.4% to 1.0% strain amplitude: Stage I: Cycling hardening Stage II: Softening/saturation Stage III: Secondary hardening [159] * Exhibits non-Masing Type-II [159]	 Taleb et al. [48] (Cyclic hardening followed by softening is considered; only peak stress variation is modeled, not loop shape) Mehani and Roy [159] (304L: Strain range memory effect is not considered in cyclic softening)

Note: *Material behavior: 'Masing', 'non-Masing Type-I' or 'non-Masing Type-II' is evaluated from stress-strain loops given in the referred articles.

4.2. Experimental details

The strain-controlled low-cycle fatigue tests were conducted on 304L and 321 austenitic stainless steels. The chemical composition (in % wt.) of the materials is shown in Table 4.2. The LCF samples were prepared with the axis of the specimen in the rolling direction. Highly polished specimens (roughness <0.1 μ m) with tight dimensional tolerances were prepared considering ASTM E606 guidelines. Only uniform gauge section specimens were considered for both materials, as shown in Figure 4.1. The LCF tests were conducted at room temperature with symmetric triangular waveforms.

^{**}Material behavior could not be determined as stress-strain loops are not given in the referred articles

For 304L SS, the specimens were prepared with a gauge diameter of 10 mm and a length of 28 mm. The tests were conducted at strain amplitudes of $\pm 0.4\%$, $\pm 0.6\%$, $\pm 0.8\%$, and $\pm 1.0\%$ under a constant strain rate of 1×10^{-3} s⁻¹ [126]. The tests were conducted on an INSTRON 8862 servo-electric fatigue test machine

For 321 SS, the specimens were prepared with a gauge diameter of 8 mm and a length of 16 mm. The tests were conducted at strain amplitudes of $\pm 0.4\%$, $\pm 0.5\%$, $\pm 0.6\%$, and $\pm 0.8\%$ under a constant strain rate of 3×10^{-3} s⁻¹. The tests were performed on a BISS (UT-20-0100) 100 kN servo-electric fatigue testing machine.

The fatigue life (N_f) of the materials at different strain amplitudes is given in Table 4.3. The fatigue life is considered as the cycle before the peak stress starts dropping rapidly due to fracture, at the end of hardening in 321 SS and secondary hardening in 304L SS.

	C %	Si %	Mn	Р%	S %	Cr%	Ni %	Ti/N	Fe %
			%					%	
304L	0.029	0.46	1.74	0.33	0.004	18.16	8.17	0.061	Balanced
SS								(N)	
321	0.027	0.620	1.80	0.027	0.011	17.630	9.450	0.24	Balanced
SS								(Ti)	

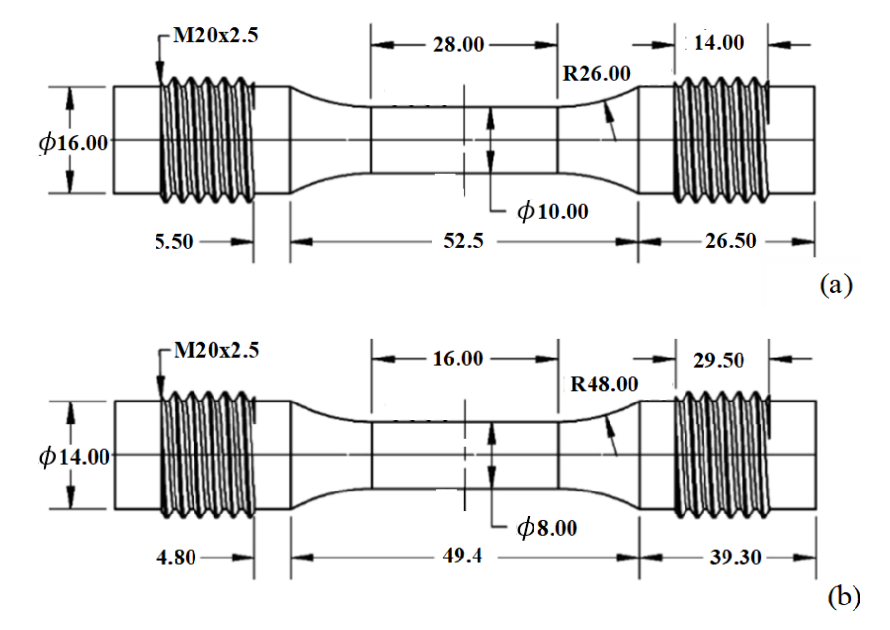


Figure 4.1. LCF test specimens: (a) 304L SS [126] and (b) 321 SS. (All dimensions are in mm)

Table 4.3. Fatigue life of the materials tested at different strain amplitudes.

Strain amplitude	Fatigue life (N_f) of 304L SS	Fatigue life (N_f) of 321 SS
±0.25%	25600	
±0.4%	13600	9000
±0.45%		6962
±0.5%		3500
±0.6%	3000	2000
±0.8%	800	500
±1.0%	500	

Note: Fatigue life (N_f) is considered as the cycle before the peak stress starts dropping rapidly due to fracture.

4.2.1. Cyclic peak stress variation

The cyclic stress amplitude of 304L SS in Figure. 4.2(a) shows initial hardening (R_1) followed by softening (R_2) , and significant secondary hardening (R_3) . However, the material 321 SS shows softening (R_2) followed by hardening (R_3) behavior, as shown in Figure. 4.2(b).

For 304L SS, it is observed that the life spent during the secondary hardening period is almost 73%, 80%, 90%, and 91% at strain amplitudes of $\pm 0.4\%$, $\pm 0.6\%$, $\pm 0.8\%$, and $\pm 1\%$, respectively. For 321 SS, the life spent during the hardening period is 83%, 86%, 92%, and 94% at strain amplitudes of $\pm 0.4\%$, $\pm 0.5\%$, $\pm 0.6\%$, and $\pm 0.8\%$, respectively. As can be seen, 321 SS exhibits more softening (R_2) and less hardening (R_3) compared to 304L SS. In both the materials, the hardening (R_3) becomes more pronounced with increased strain amplitude. This is probably due to an increased amount of deformation-induced martensite formation [126].

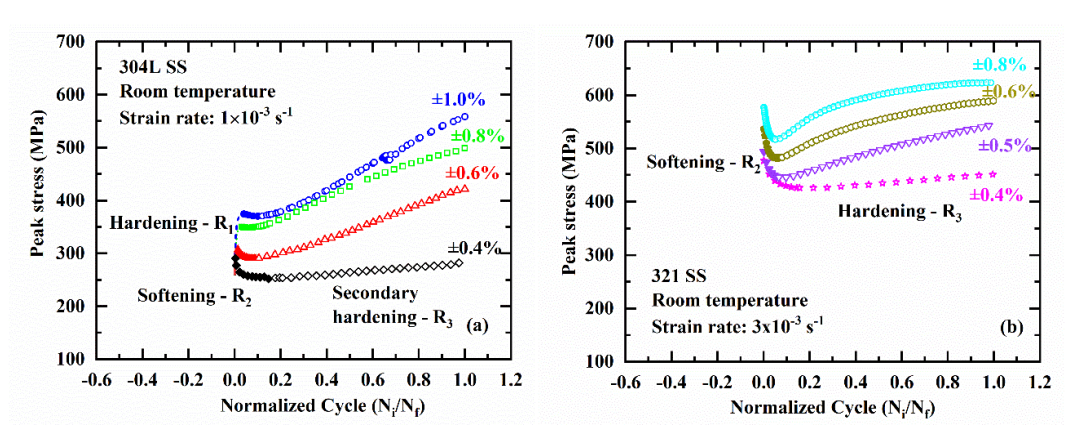


Figure. 4.2. Peak stress variation with number of cycles for (a) 304L SS and (b) 321SS.

4.2.2. Yield surface expansion and translation with cycling

The yield surface expansion in constitutive model is modeled by considering peak effective stress (σ^0), *i.e.*, half of the linear stress of the loading branch of different stress-strain loops as explained in Chapter 3: Section 3.4. Further, the yield surface expansion is analyzed for various regions, *i.e.*, initial hardening (R_1), softening (R_2) and secondary hardening (R_3). For 304L SS at $\pm 0.4\%$ strain amplitude, it is observed that for the initial hardening region (R_1) (*i.e.* $2^{\rm nd}$ cycle to the $10^{\rm th}$ cycle), the linear stress increases. For the softening region (R_2)(i.e. $10^{\rm th}$ cycle to the $3000^{\rm th}$ cycle), the linear stress decreases, and for the secondary hardening region (R_3) ($3000^{\rm th}$ cycle to the $13000^{\rm th}$ cycle), the linear stress again increases, as shown in Figure. 4.3(a). For 321 SS, the linear stress decreases and then increases for softening (*i.e.*, $2^{\rm nd}$ cycle to the $2000^{\rm th}$ cycle) and hardening (*i.e.*, $2000^{\rm th}$ cycle to the $9000^{\rm th}$ cycle) regions, respectively, as shown in Figure. 4.3(b). A similar trend in peak effective stress variation cyclic hardening behavior is observed for other strain amplitudes for both materials.

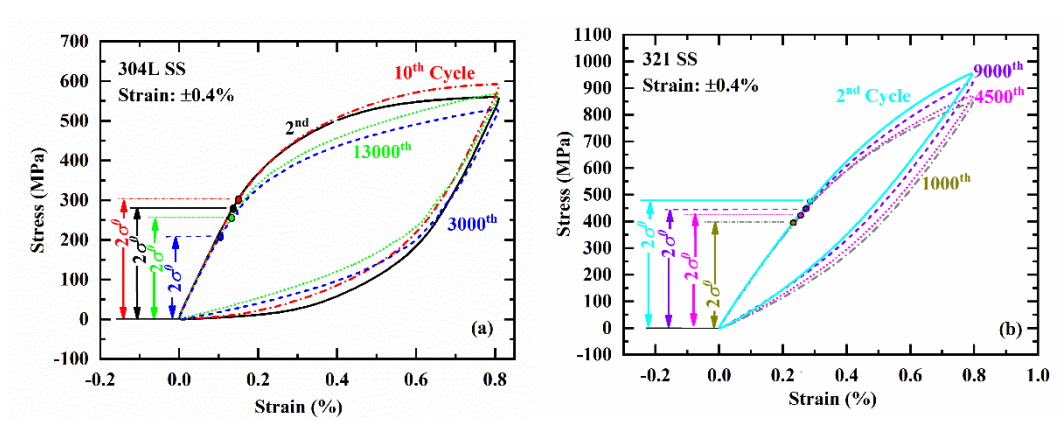


Figure. 4.3. Linear stress variation in different cyclic hardening/softening regions of (a) 304L SS and (b) 321 SS, highlighted with translated (at origin) hysteresis loops from different regions.

Thus, it can be said that for both 304L SS and 321 SS, the peak effective stress (σ^0) is cycle-dependent and increases with hardening and decreases with softening. A MATLAB-based program is written for the calculation of the peak effective stress (σ^0), *i.e.*, (linear stress/2) from different hysteresis loops, and is plotted in Figure. 4.4(a) for 304L SS and Figure. 4.4(b) for 321 SS.

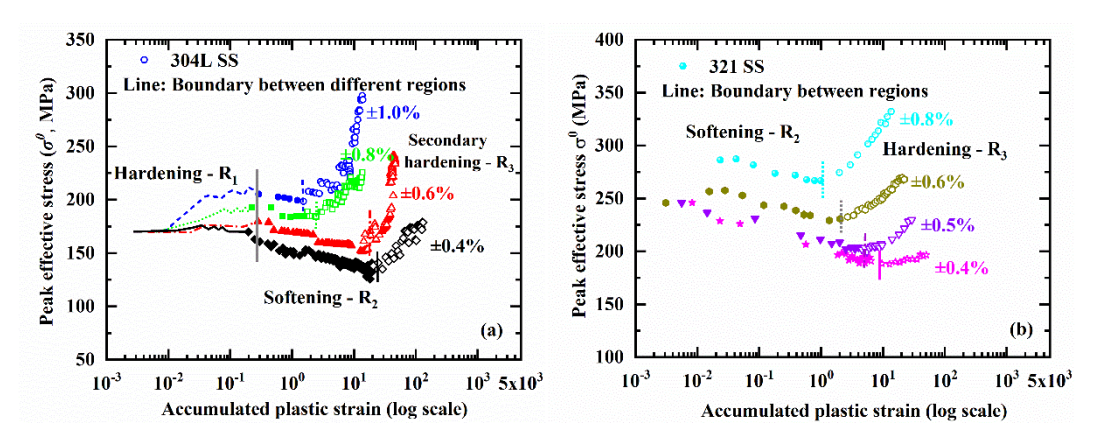


Figure. 4.4. Peak effective stress variation with accumulated plastic strain (a) 304L SS (b) 321 SS.

Also, Figure. 4.3(a) for 304L SS and Figure. 4.3(b) for 321 SS (plotted with different cycles covering the initial hardening, softening, and secondary hardening regions) highlights that the loop shape changes significantly with cycling. In literature, the loop shape variation with cycling is characterized by the evolution of translation of yield surface, *i.e.*, peak back stress with cycling [13,49,51,123,187]. The linear region is eliminated from the stress vs. strain curve to obtain the peak back stress. The peak back stress from different stress-strain hysteresis loops is plotted with accumulated plastic strain for 304L SS and 321 SS, as shown in Figure. 4.5(a) and Figure. 4.5(b), respectively. It is observed that the peak back stress with accumulated plastic strain shows initial hardening, softening, and secondary hardening regions for 304L SS. In comparison, material 321 SS shows softening and hardening only. Thus, the peak back stress variation is similar to the peak tensile stress variation with cycling (Figure. 4.4 and Figure. 4.5).

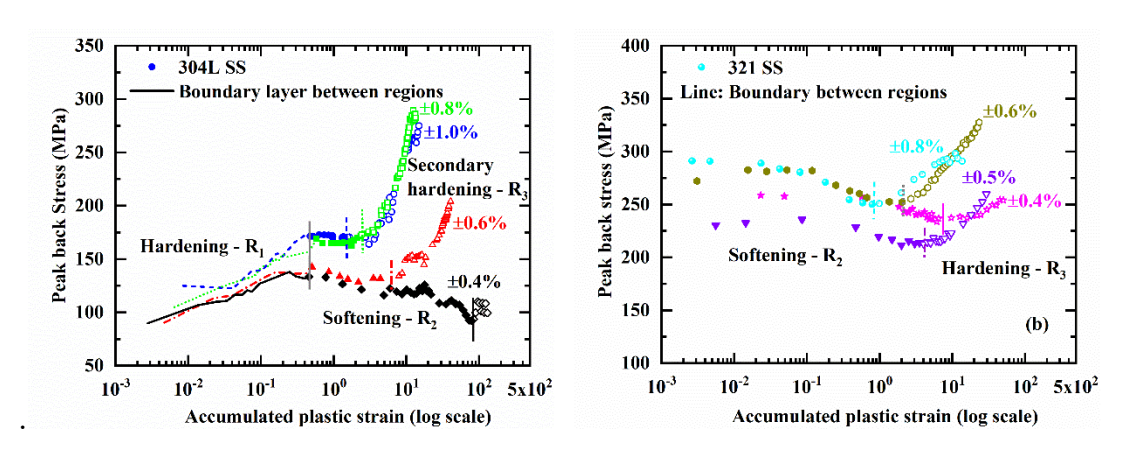


Figure. 4.5. Peak back stress vs. accumulated plastic strain for (a) 304L SS and (b) 321 SS at different strain amplitudes.

To model the loop shape change with cycling, a non-dimensional parameter ($\varphi_{\rm mod}$), defined as the ratio of 'maximum back stress at any cycle' to the 'maximum back stress at the first cycle,' is introduced, considering it to be a function of accumulated plastic strain, 'p' [159]. The same parameter is also used by others [13,51], but they did not validate the applicability of $\varphi_{\rm mod}(p)$ for materials with significant secondary hardening, and changes in the cyclic behavior with strain amplitude. Moreover, the equation used by Song et al. [13] and Zhou et al. [51] could not model significant secondary hardening exhibited by 304L SS; thus, Eq. (4.4) is proposed [159]. In this article, the applicability of $\varphi_{\rm mod}(p)$ is validated with two grades of stainless steels, 304L SS and 321 SS, that show different cyclic behaviors with significant softening and hardening. The variation of $\varphi_{\rm mod}$ with p is plotted for 304L SS in Figure. 4.6(a) and for 321 SS in Figure. 4.6(b).

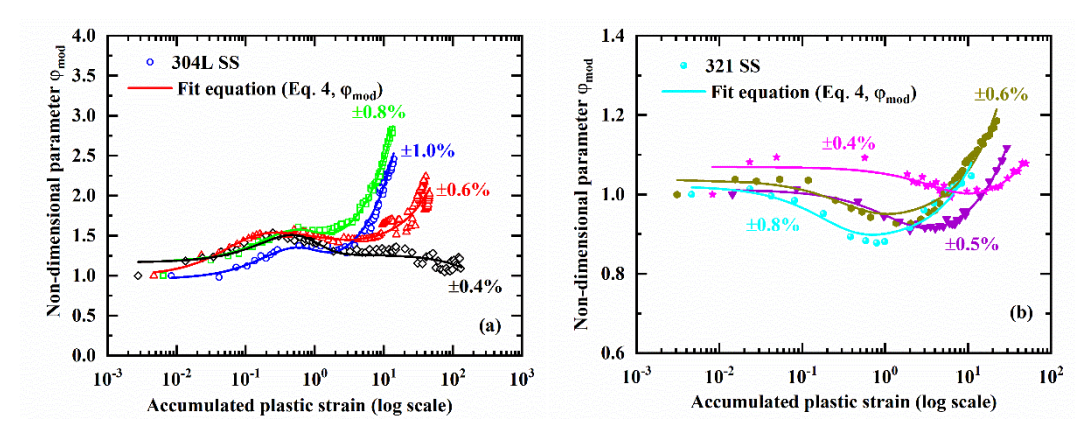


Figure. 4.6. Variation of φ_{mod} with accumulated plastic strain (p) at different strain amplitudes for (a) 304L SS and (b) 321 SS.

4.2.3. Strain range dependence behavior

The half-life stress-strain (%) loops for 304L SS and 321 SS are translated and tied together at a common tensile yield point, as shown in Figure. 3.2(a) and Figure. 3.2(b). The

increase in linear elastic stress $(2\sigma^0)$ with strain amplitude for 304L SS and 321 SS can be seen in Figure. 3.2(a) and Figure. 3.2(b), respectively. The change in linear elastic stress with strain amplitude is considered in constitutive modeling by strain range memory effect in the expansion of the yield surface. The peak effective stress (σ^0) variation with accumulated plastic strain (p) is plotted in Figure. 4.4(a) and Figure. 4.4(b) for 304L SS and 321 SS, respectively.

For 304L SS (Figure. 4.4(a)), it is observed that the initial hardening (R_1) occurs with almost the same amount of plastic strain accumulation (0.2) at different strain amplitudes. However, the softening (R_2) and secondary hardening (R_3) regions at different strain amplitudes result in significant variations in the amount of plastic strain accumulation. For 321 SS also, it is observed that the plastic strain accumulation varies significantly with strain amplitudes in the softening (R_2) and hardening (R_3) regions, as shown in Figure. 4.4(b). Thus, the strain range memory effect in peak effective stress is considered only for the softening (R_2) and secondary hardening (R_3) regions for 304L SS. For 321 SS, the strain range memory effect is considered for the whole life (i.e., R_2 and R_3 regions). Similar considerations for strain range memory effect for different materials (such as 2.2.5Cr 1Mo SS and 316L) are reported in the open literature [11,188]

It can be seen in Figure. 3.2(a) the linear elastic stress limit and strain hardening rate behavior (*i.e.*, loop shape) change with strain amplitude for 304L SS. However, for 321 SS (Figure. 3.2(b)), the linear elastic stress limit only changes with strain amplitude; the loop shape beyond the common yield point (σ_{y0}) remains almost the same. Thus, according to Sanjeev et al. [16], the cyclic behavior of 321 SS and 304L SS can be considered 'non-Masing Type-I' and 'non-Masing Type-II', respectively. More details about Masing/non-Masing behavior can be found in [189]. For Type-I non-Masing behavior of 321 SS, although the strain hardening behavior remains almost the same (as shown in Figure. 3.2(b)), the peak back stress variation with accumulated plastic strain (Figure. 4.5(b)) shows significant changes with strain amplitude. The accumulated plastic strain in different regions varies significantly with strain amplitudes for 321 SS (Figure. 4.5(b)). Similar variation in the accumulated plastic strain with strain amplitudes can be found for 304L SS in the softening and secondary hardening regions (Figure. 4.5(a)).

Thus, the strain range memory effect in kinematic hardening is considered for 304L and 321 SS. It should also be noted that the apparent matching or mismatching of the

hysteresis at different strain amplitudes (as shown in Figure. 3.2) cannot be taken as an indicator to include or exclude the strain range memory effect in kinematic hardening.

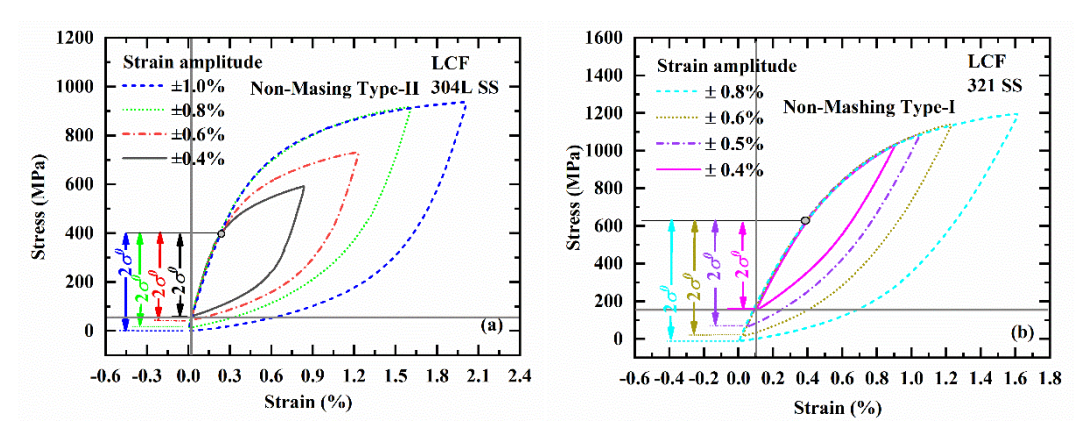


Figure. 4.7. Translated stress-strain loops at common tensile yield point (a) 304L SS (b) 321SS at half-life.

4.2.4. Transient back stress effect

The Transient Bauschinger Effect (TBE) or Transient Back Stress Effect is defined as the change in plastic modulus (or rate of work hardening) of the first reverse loading curve at the initial yield point [11,49,51,165,190], as shown in Figure. 4.8. It is evident that for material 304L SS, the plastic modulus changes significantly, as shown in Figure. 4.8(a), while it is almost the same for 321SS, at the initial yield point, as shown in Figure. 4.8(b). The shifted stress-strain curves of the reverse loading [190] in Fig. 10 were obtained using the following Eq. (4.1) and Eq. (4.2).

$$\sigma_{Shift} = -(\sigma_{reveerse} - \sigma_{max})/2 \tag{4.1}$$

$$\varepsilon_{Shift} = -(\varepsilon_{reveerse} - \varepsilon_{max})/2$$
 (4.2)

Similar to the behavior of 304L SS in Fig. 10(a), Yang et al. [11] have also reported, for 316L SS, that the plastic modulus of reverse loading at initial yield stress is more than that of the monotonic tensile curve. Moreover, the plastic modulus has also been reported to increase with increased strain amplitude due to the same effect. On the contrary, Xu et al. [190] have shown for U20Mn carbide-free bainitic rail steel that the plastic modulus of reverse loading at initial yield stress is less than that of the monotonic tensile curve. Moreover, the plastic modulus has also been reported to decrease with increasing strain amplitude due to TBE. Thus, the change in plastic modulus (or strain hardening rate) from one strain amplitude to another may occur due to TBE.

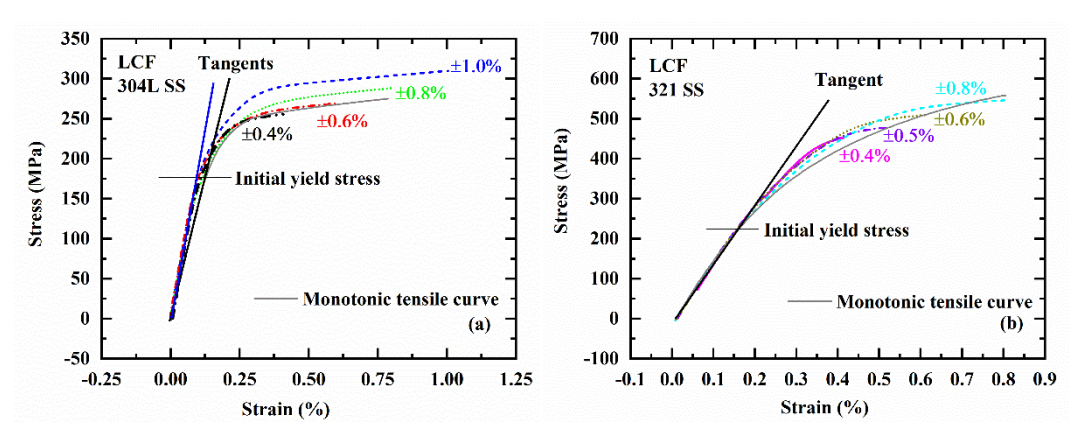


Figure. 4.8. Comparison of the monotonic tensile curve and shifted reverse stress-strain (%) curves for (a) 304L SS and (b) 321 SS.

The back stress is calculated from the 2nd stress-strain loops, *i.e.*, after the first load reversal. It is plotted with plastic strain, as shown in Figure. 4.9. Similar to the TBE of 304L SS, a significant variation in the kinematic hardening rate at different strain amplitudes can be observed in Figure. 4.9(a). Thus, this significant variation in strain hardening rate is also attributed to the transient Bauschinger effect. However, for material 321 SS, the rate of kinematic hardening rate is almost the same as depicted in Figure. 4.9(b) for different strain amplitudes. Thus, the transient back stress effect is considered for 304L SS but not 321 SS.

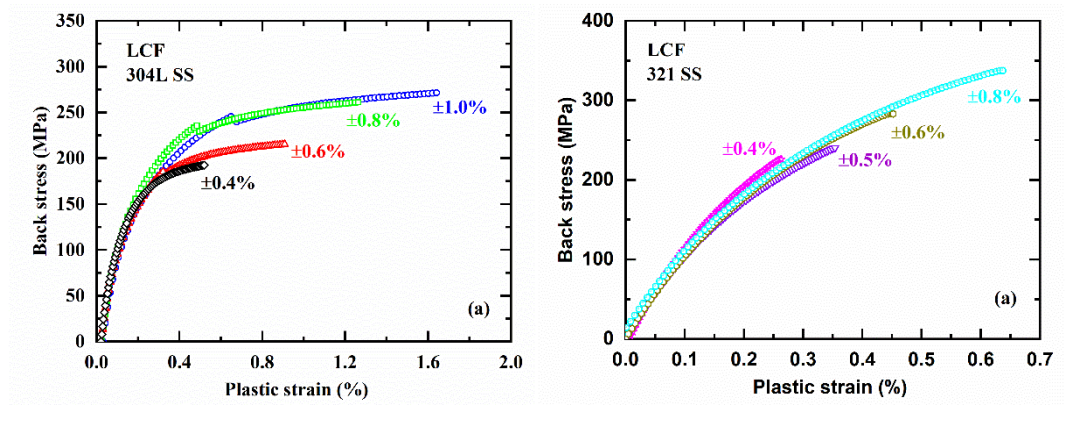


Figure. 4.9. Back stress vs. plastic strain (%) curve for (a) 304L SS and (b) 321 SS obtained from the loading branches of the 2nd cycle

4.3. Constitutive model

4.3.1. Modeling yield surface expansion and translation with cycling

The variation of the isotropic and kinematic hardening, *i.e.*, peak effective stress (σ^0) and non-dimensional parameter (ϕ_{mod}) with cycling, is modeled as an additive decomposition of three terms for cyclic hardening $(1^{st}$ term), softening $(2^{nd}$ term), and

secondary hardening (3rd term) behaviors, as given by Eq. (4.3) and Eq. (4.4) [159]. These equations could be directly used for 304L SS as the material exhibited initial hardening (R_1) , softening (R_2) , and secondary hardening (R_3) behaviors, as shown in Figure. 4.4(a) and Figure. 4.5(a). However, as 321 SS did not exhibit the initial hardening (R_1) behavior (as shown in Figure. 4.4(b) and Figure. 4.5(b)), the value of Q = 0 and $\sigma_1 = 0$ may be considered in Eq. (4.3), and the value of $a_3 = 0$ and $a_5 = 0$ may be considered in Eq. (4.4) to model its cyclic hardening/softening behavior. The parameter σ_1 represents the stress at the end of initial hardening and the start of softening regions. Thus, the absence of the initial hardening region (Q = 0) essentially indicates that σ_1 does not exist; hence, softening starts from a stress level equal to σ_{y0} . A similar explanation goes for considering zero values of a_3 in Eq. (4.4) for 321 SS.

$$\sigma^{0} = [\sigma_{y0} + Q(1 - exp(-bp))] + [\sigma_{1} + Q_{1}(1 - exp(-b_{1}p))] + [\sigma_{2} + a_{1}p]$$

$$1^{\text{st}} \text{ term} \qquad 2^{\text{nd}} \text{ term} \qquad 3^{\text{rd}} \text{ term} \qquad (4.3)$$

$$\varphi_{\text{mod}} = [a_2 + a_3(1 - exp(-a_4p))] + [a_5 + a_6(1 - exp(-a_7p))] + [a_8 + a_9p]$$
(4.4)

4.3.2. Modeling of strain range dependence behavior

The strain range memory effect is considered in both isotropic and kinematic hardening equations for softening (R_2) and secondary hardening (R_3) regions for 304L SS and softening (R_2) and hardening (R_3) region for 321 SS, as discussed in Section 4.2.2. In the constitutive model, the strain range memory effect is incorporated through a non-dimensional parameter, ζ , which gives an estimate of cyclic hardening or cyclic softening rate (depending on the hardening or softening behavior under consideration) with accumulated plastic strain and is given by Eq. (3.14) [159].

$$\zeta_{i} = \left(\frac{\Delta \sigma_{PS_{i}}}{\left(\left(\sum_{i=1}^{k} \Delta \sigma_{PS_{i}}\right)/k\right)}\right) / \left(\frac{\Delta p_{S_{i}}}{\left(\left(\sum_{i=1}^{k} \Delta p_{S_{i}}\right)/k\right)}\right)$$
(4.5)

The non-dimensional parameter, ζ , is generalized here for different regions (softening and hardening/secondary hardening) irrespective of the material's 'non-Masing Type-I' or 'non-Masing Type-II' behavior. For cyclic softening rate (ζ_S), $\Delta\sigma_{PS}$ is calculated as the change in peak stress due to softening only (*i.e.*, in R_2 region), Δp_S is calculated as the accumulated plastic strain associated with the softening region only, k varies from 1 to k, where k represents the different strain amplitude tests. The parameter ζ_S is plotted with the maximum plastic strain range (q), as shown in Figure. 3.7(a) and Figure. 3.7(b), for

304L SS and 321 SS, respectively. It is interesting to note that ζ_S varies exponentially with q for both materials. It is given by the relationship in Eq. (3.15), in which a_{10} , a_{11} and a_{12} are material parameters.

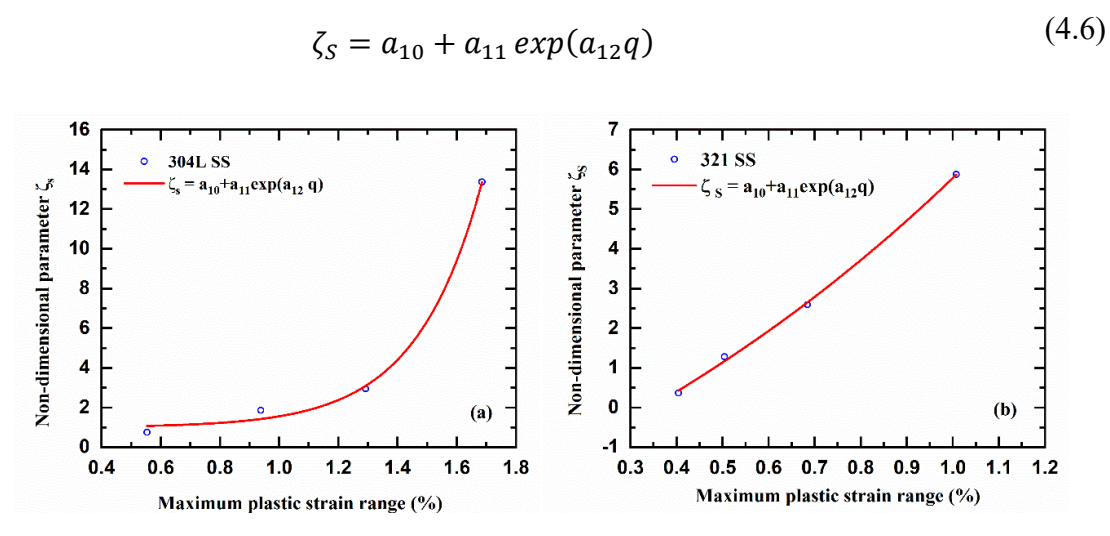


Figure. 4.10. Variation of ζ_S with maximum plastic strain range (%) for (a) 304L SS and (b) 321 SS

Similarly, the cyclic hardening rate, ζ_H , is calculated for 304L SS and 321 SS from the secondary hardening and hardening region, respectively, using Eq. (3.14) and plotted with the maximum plastic strain range (q), Figure. 4.11(a) and Figure. 4.11(b). As can be seen, both materials are found to follow an S-shaped growth curve defined by the relationship in Eq. (4.7), in which a_{13} , a_{14} , and a_{15} are material parameters [159].

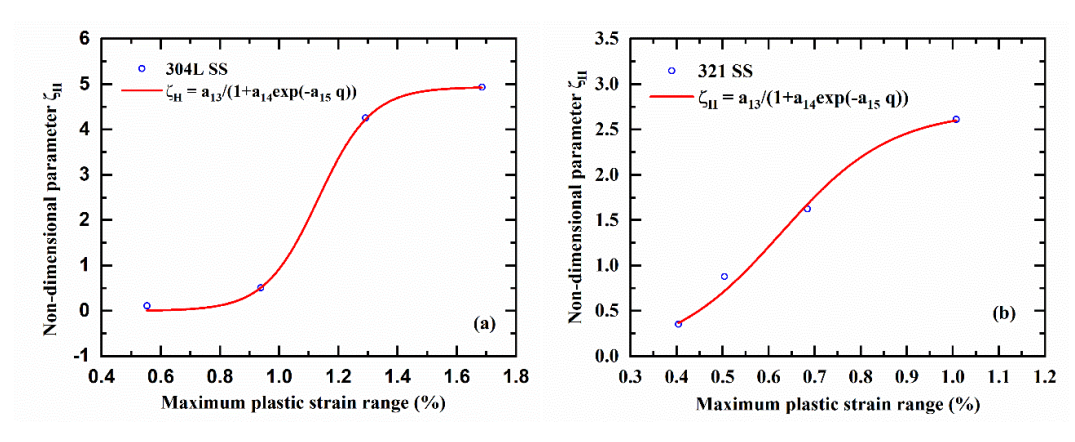


Figure. 4.11 Variation of ζ_H with maximum plastic strain range (%) for (a) 304L SS and (b) 321 SS

$$\zeta_H = a_{13}/(1 + a_{14} \exp(-a_{15}q)) \tag{4.7}$$

Now, with the help of the parameters: ζ_S and ζ_H , the isotropic and kinematic hardening equations, *i.e.*, Eq. (4.3) and Eq. (4.4), are modified to make them maximum plastic strain range memory dependent, as shown by Eq. (3.16), Eq. (3.17), and Eq. (3.18).

$$\tilde{\sigma}^0 = \sigma^0 + (\zeta_H - 1)a_1p + (Q_1 \exp(-b_1p))(1 - \exp(-\zeta_S b_1 p + b_1 p)) \tag{4.8}$$

$$\tilde{\varphi} = \varphi_{mod} + (\zeta_H - 1)a_9p + (a_6 \exp(-a_7p))(1 - \exp(-\zeta_S a_7p + a_7p))$$
(4.9)

$$\dot{\mathbf{x}} = \tilde{\varphi} \frac{2}{3} C \dot{\boldsymbol{\varepsilon}}_{p} - \gamma \boldsymbol{x} \, \dot{p} \tag{4.10}$$

In the above equation, x represents the back stress. It is interesting to note that as the strain range memory effect is not considered for the initial hardening region, which the material 304L SS exhibits, the Eq. (3.16) to Eq. (3.18) can be invariably applied to both 304L and 321 SS materials.

4.3.3. Modeling of transient back stress effect

The material 304L SS exhibiting Type-II non-Masing behavior shows significant variation in plastic modulus with strain amplitude, as shown in Figure. 4.8(a). In the constitutive model, the plastic modulus variation is taken into account through normalized maximum back stress (φ_{KH}) variation as a function of the maximum plastic strain range (q). The parameter φ_{KH} is obtained by dividing the 'maximum back stress at 2nd cycle for different strain amplitudes' by the 'maximum back stress at the highest strain amplitude'. The normalized maximum back stress (φ_{KH}) is plotted with the maximum plastic strain range (q), as shown in Figure. 3.8(a), for 304L SS. The dependence of φ_{KH} on q, could be given by Eq. (3.19) and is implemented in the constitutive model, as shown by Eq. (4.12). For 321 SS material, as the kinematic hardening rate remains almost the same for different strain amplitudes (Figure. 4.9(b)), $\varphi_{KH} = 1$ is considered in Eq. (4.12).

$$\varphi_{KH} = a_{16} + a_{17} exp(a_{18}q) \tag{4.11}$$

$$\dot{\mathbf{x}} = \varphi_{KH} \left(\tilde{\varphi} \frac{2}{3} C \dot{\boldsymbol{\varepsilon}}_{\boldsymbol{p}} - \mathbf{x} \, \dot{\boldsymbol{p}} \right) \tag{4.12}$$

The strain range memory-dependent equations are incorporated into the constitutive model with the help of the plastic strain memorization equations given by Chaboche et al. [116].

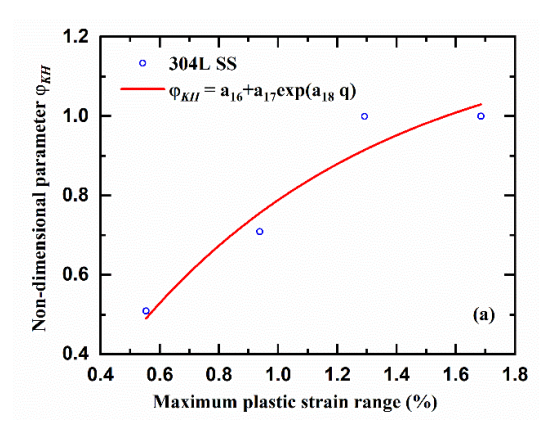


Figure. 4.12. Variation of φ_{KH} with maximum plastic strain range (%) (a) 304L SS (b) 321 SS.

All the equations associated with the proposed constitutive model, as discussed in Section 4.3.1 to Section 4.3.3, along with the strain range memory functions, are summarized in Table 4.4 (strain, stress and back stress are shown in voigt notation, as used for implementation in ABAQUS user subroutine).

Table 4.4. Summarized framework of the equations used in the modified constitutive model.

Basic framework used in the proposed modified constitutive model:

$$\vec{\varepsilon} = \overrightarrow{\varepsilon_e} + \overrightarrow{\varepsilon^p}; \overrightarrow{\sigma^{tr}} = \mathbf{C}: (\vec{\varepsilon} - \overrightarrow{\varepsilon^p}); f = J_2(\vec{\sigma} - \vec{x}) - \tilde{\sigma}^0; \overrightarrow{\dot{\varepsilon}^p} = \frac{3}{2} \lambda \frac{\overrightarrow{\sigma'} - \vec{x}}{J_2(\vec{\sigma} - \vec{x})}$$

Isotropic hardening rule:

$$\sigma^0 = r(p) + \sigma_{y0} + \sigma_1 + \sigma_2; r(p) = Q(1 - exp(-bp)) + Q_1(1 - exp(-b_1p)) + a_1p(-bp) + a_2p(-bp) + a_2p(-bp$$

Non-linear kinematic hardening rule:

$$\vec{x} = \sum_{i=3}^{3} \vec{x_i} ; \vec{x} = \frac{2}{3} C_i \vec{\varepsilon_p} - \gamma_i \vec{x} \ \dot{p}$$

Memory surface equations, including kinematic/isotropic hardening laws:

$$\begin{split} &\zeta_S = a_{10} + a_{11} \exp(a_{12}q); \, \zeta_H = a_{13}/(1 + a_{14} \exp(-a_{15}q)) \\ &\tilde{\sigma}^0 = \sigma^0 + (\zeta_H - 1)a_1p + (Q_1 \exp(-b_1p)) \big(1 - \exp(-\zeta_S b_1 p + b_1 p)\big) \\ &\tilde{\varphi} = \tilde{\varphi}_{mod} = \varphi_{mod} + (\zeta_H - 1)a_9p + (a_6 \exp(-a_7p)) \big(1 - \exp(-\zeta_S a_7 p + a_7 p)\big) \\ &\varphi_{KH} = a_{16} + a_{17} \exp(a_{18}q) \; ; \\ &\vec{x} = \varphi_{KH} \left(\tilde{\varphi} \frac{2}{3} C \overrightarrow{\dot{\epsilon_p}} - \vec{x} \; \dot{p} \right) \end{split}$$

Memory surface model:

$$F(q) = \sqrt{\frac{2}{3}(\vec{\varepsilon}^{\vec{p}} - \vec{\alpha}) : (\vec{\varepsilon}^{\vec{p}} - \vec{\alpha})} - q$$

$$\vec{\alpha} = (1 - \eta)H(F)\langle \vec{n}: \vec{n}^* \rangle \vec{n}^* \dot{p} ; \vec{n}^* = (\vec{\epsilon}^{\vec{p}} - \vec{\alpha}) / \sqrt{(\vec{\epsilon}^{\vec{p}} - \vec{\alpha}): (\vec{\epsilon}^{\vec{p}} - \vec{\alpha})} ;$$

$$\vec{n} = \sqrt{\frac{3}{2}} (\vec{\sigma}' - \vec{x}) / J_2(\vec{\sigma} - \vec{x})$$

$$\dot{q} = \eta H(F)\dot{p} ; H(F) \text{ is Heaviside function}$$

4.4. Identification and calibration of material parameters

In the literature, models are proposed with 23 to 40 parameters for simulating the LCF behavior of materials, e.g., Xu et al. [13] used 34, Xing et al. [125] considered 40, Zhou et al. [51] used 30, and Song et al. [13] used 23 material parameters. Although these models are interesting and make a significant contribution in understanding the complex LCF behavior of different materials, none has taken into account the significant secondary hardening behavior. Moreover, as Type-II non-Masing behavior was identified recently, no model in literature has demonstrated the capability of modeling of Type-II non-Masing behavior, as done in the current investigation. The proposed constitutive model uses a total of 31 material parameters. All parameters are required to be defined to simulate the initial hardening, softening, and secondary hardening behavior of 304L SS that exhibit Type-II non-Masing behavior. However, as 321 SS did not exhibit the initial hardening part, only 21 parameters are required to be defined for simulating its Type-I non-Masing behavior. The material parameters are given in Table 4.5.

Initially, all the material parameters of the constitutive model are determined as per the model description provided through Eq. (4.3) to Eq. (4.12). Then, the parameters have been calibrated as explained in the flowchart given in Figure. 4.13. In step-1, E and σ_{y0} are determined from the initial loading part of the first cycle, as shown in Chapter 3: Section 3.4, Figure. 3.9. In step-2, C_1 and γ_1 are determined from the upper branch of the hysteresis loop (of 2^{nd} cycle) obtained from the highest strain amplitude test. As these parameters are taken from the 2^{nd} cycle, the loop shape of the 1^{st} cycle cannot be compared with the experimental one. In step-3, φ_{mod} is estimated as a function of p (accumulated plastic strain) and the parameters a_2 to a_9 are determined using Eq. (4.4) for different strain amplitudes (as shown in Figure. 4.6). The average values of the parameters determined at different strain amplitudes are used as the initial values for the material parameters calibration. In step-4, σ^0 is determined from the different hysteresis loops of a test and defined as a function of p. Fitting Eq. (4.3) to the σ^0 vs. p data, the isotropic hardening parameters are determined for different strain amplitudes (as shown in Figure. 4.4), and the

average values are used as the initial parameters for calibration. It should be noted that only Q, b, Q_1 , b_1 , a_1 parameters are considered for calibration. The calibration is done stepwise for different regions of the cyclic hardening/softening curves (Figure. 4.2) by comparing the simulated and experimental peak stresses obtained at different strain amplitudes. As shown in Figure. 4.13(a) for 304L SS, the isotropic hardening parameters are calibrated by considering the reference point 1 in the initial hardening region (R_1).

Then, in step 5, ζ_S is estimated according to Eq. (3.14) and defined as a function of q in the form of Eq. (3.15) to determine the parameters a_{10} to a_{12} (shown in Figure. 3.7). In step-6, φ_{KH} is estimated as explained in Section 4.3.3 and defined as a function of q in the form of Eq. (3.19) to determine the parameters a_{16} to a_{18} (shown in Figure. 3.8). As shown in Figure. 4.13(b) for 304L SS, the material parameters (a_{10} to a_{12} and a_{16} to a_{18}) are calibrated by considering the reference point 2 in the cyclic softening region (R_2).

Finally, ζ_H is estimated according to Eq. (3.14) and defined as a function of q in the form of Eq. (4.7) to determine the parameters a_{13} to a_{15} (shown in Figure. 4.11). As shown in Figure. 4.13(c) for 304L SS, the material parameters (a_{13} to a_{15}) are calibrated by considering the reference point 3 in the secondary hardening region (R_3).

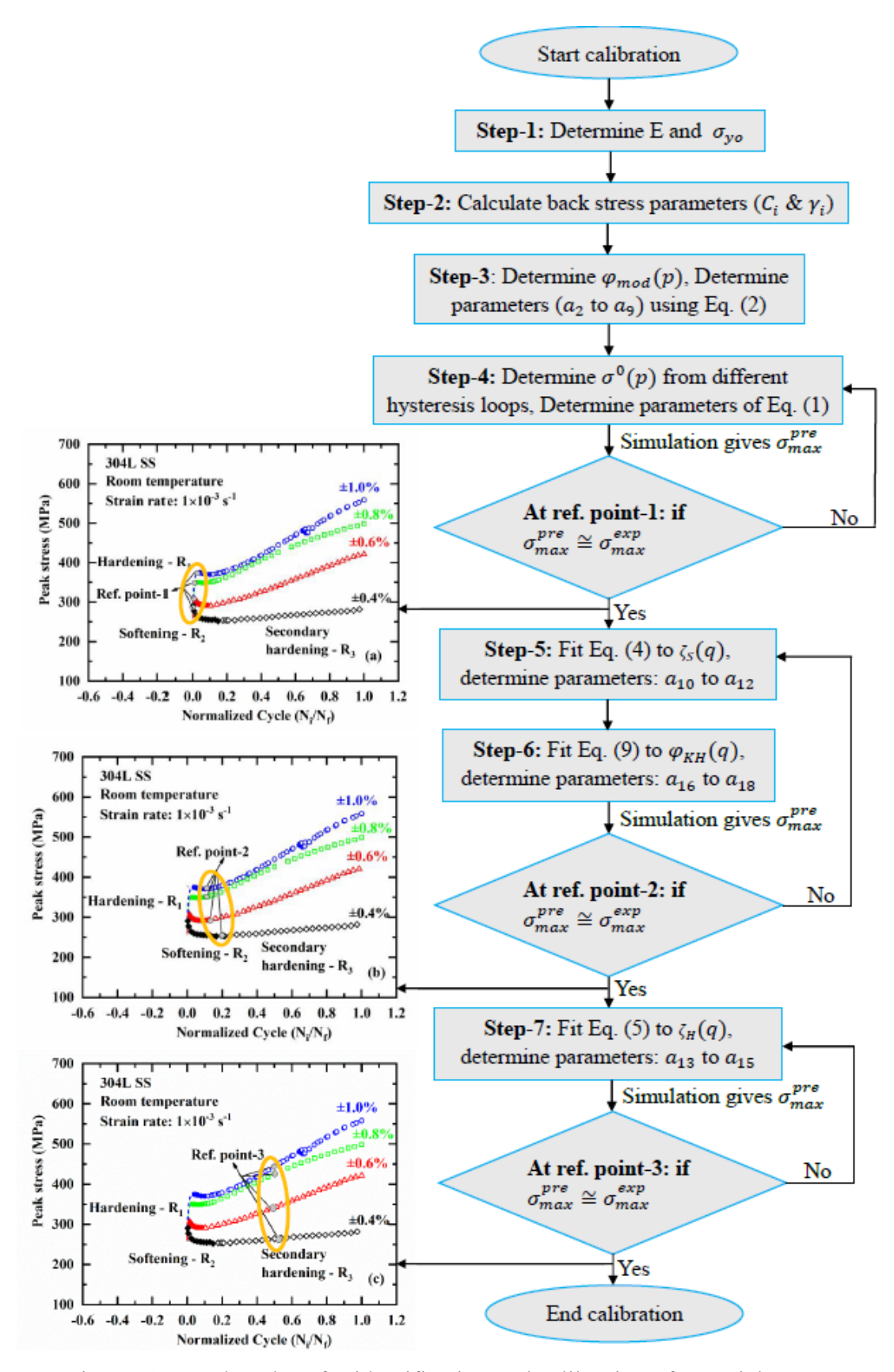


Figure. 4.13. Flowchart for identification and calibration of material parameters

Table 4.5. Material parameters for 304L SS and 321 SS

304L SS	$E = 187.60 \text{ GPa}, \nu = 0.3$
Isotropic	$\sigma_{yo} = 170 \text{ MPa}, Q = 54.81 \text{ MPa}, b = 12.96, \sigma_1 = 197.69 \text{ MPa},$
	$Q_1 = -44.57 \text{ MPa}, b_1 = 1.33, \sigma_2 = -204.78 \text{ MPa}, a_1 = 5.233$
ζ_S	$a_{10} = 1.592, \ a_{11} = -1.52035, \ a_{12} = -538.265$
ζ_H	$a_{13} = 3.003, a_{14} = 91535.51689, a_{15} = 10069.232$
Kinematic	$C = 57345.81 \text{ MPa}, \ \gamma = 378.9$
$arphi_{mod}$	$a_2 = 1, a_3 = 1.157, a_4 = 3.326, a_5 = 1.527, a_6 = -1.057,$
	$a_7 = 1.654, a_8 = -1.369, a_9 = 0.106$
$arphi_{KH}$	$a_{16} = 0.505, \ a_{17} = 0.973, \ a_{18} = 250.06577, \eta = 0.95$
321 SS	$E = 165.6576 \text{ GPa}, \nu = 0.3$
Isotropic	σ_{yo} =248.604 MPa, Q_1 = -64.742 MPa, b_1 = 0.984, σ_2 = 5.531
	MPa, $a_1 = 5.5435$
ζ_S	$a_{10} = -11.53027, a_{11} = 8.2592, a_{12} = 971.49779$
ζ_H	$a_{13} = 2.51506, \ a_{14} = 59.238, a_{15} = 7602.331$
Kinematic	$C = 152681.2 \text{ MPa}, \ \gamma = 436.7$
$arphi_{\mathrm{mod}}$	$a_2 = 1, a_6 = -0.138, a_7 = 0.526, a_8 = 0.021, a_9 = 0.018, \eta = 0.95$

4.5. Comparison of experimental and simulation results

The constitutive model, developed in Section 4.3, is implemented in ABAQUS with the help of a user material subroutine (UMAT). A three-dimensional model with 35 mm × 35 mm × 35 mm dimensions, as shown in Figure. 4.14 (with boundary conditions), is used for simulations. A three-dimensional 8-noded linear brick element (C3D8) is considered for simulations. The model was subjected to cyclic strain with a triangular waveform. The accuracy and prediction capability of the proposed model is verified with the strain-controlled low-cycle fatigue test data of 304L SS and 321 SS at different strain amplitudes.

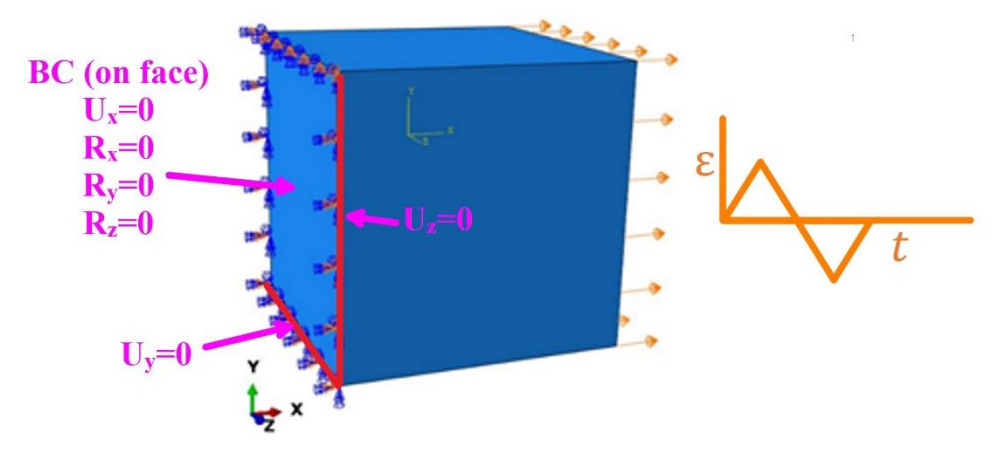


Figure. 4.14. 3D model used for the simulation. R denotes rotational degrees of freedom, and U denotes displacement.

4.5.1. Accuracy of the model

4.5.1.1. Cyclic peak stress

The variation in cyclic peak stress with the number of cycles for the experimental and simulation results is shown in Figure. 4.15. As can be seen, the model predicts the variation in cyclic stress amplitude with high accuracy up to failure. The trend in the material behavior exhibited by the simulated and experimental results remains the same throughout the life of the material.

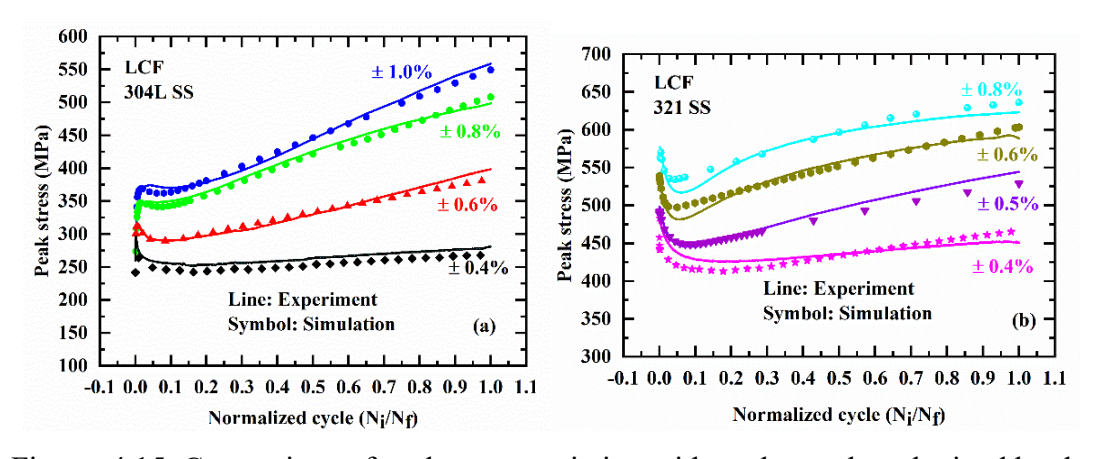


Figure. 4.15. Comparison of peak stress variation with cycle number obtained by the proposed model for (a) 304L SS and (b) 321 SS.

4.5.1.2. Hysteresis loop shape

To verify the ability of the model to retain the 'Type-I non-Masing' behavior of 321 SS and 'Type-II non-Masing' behavior of 304L SS in the simulated results, the half-life hysteresis loops of the simulation and experimental results are plotted together in Figure. 4.16(a-b). As can be seen, the non-Masing behavior of both materials could be

captured well by the proposed constitutive model. It should also be noted that 304L SS shows Type-I non-Masing behavior up to ~10% life fraction, beyond which the behavior changes to Type-II non-Masing, as shown in the article [17]. This transition is also well captured by the proposed constitutive model. Figure. 4.17. shows the Type-I and Figure. 4.16(a) shows Type-II non-Masing behaviors of 304L SS at 7% and 50% life fractions, respectively. Recently, Sanjeev et al. [126] have shown that identifying Type-I and Type-II non-Masing behavior under fatigue is important for accurately estimating cyclic plastic strain energy density and subsequent fatigue life prediction. Thus, the constitutive model used for simulating the fatigue behavior of material (or component) must not lose the characteristics of the material's Type-I and Type-II non-Masing behavior. It should be noted that the conventional non-linear isotropic-kinematic hardening model, commonly available in commercial software like ABAQUS, is defined by a minimum of seven material parameters: σ_{yo} , E, v, Q, b, C and γ , and inherently predict the Masing behavior of materials, as shown in article [17].

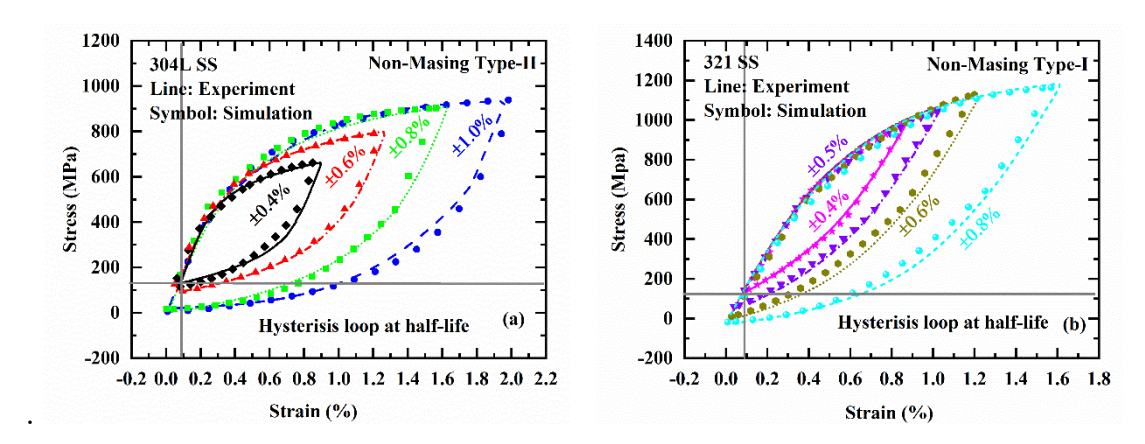


Figure. 4.16. Comparison of half-life hysteresis loops obtained at different strain amplitudes for (a) 304L SS and (b) 321 SS.

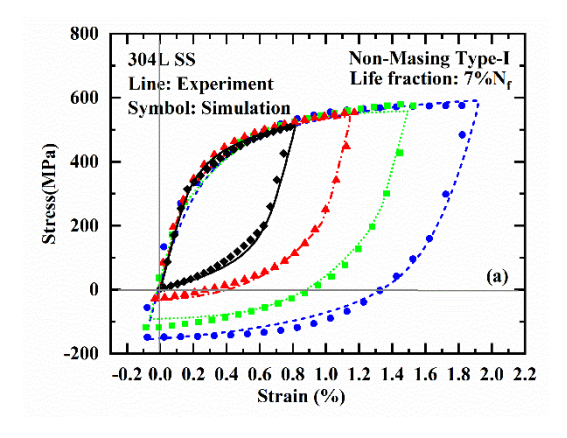


Figure. 4.17. Type-I non-Masing behavior of 304L SS at 7% life fraction.

To show that the hysteresis loop shape is predicted accurately throughout the life, the experimental and simulated loops are plotted together for different cycles at the minimum and maximum strain amplitudes of LCF testing, *i.e.*, $\pm 1.0\%$ and $\pm 0.4\%$ for material 304L SS, as shown in Figure. 4.18 and Figure. 4.19, respectively, and $\pm 0.8\%$ and $\pm 0.4\%$ for material 321 SS, as shown in Figure. 4.20 and Figure. 4.21, respectively. As can be seen in Figure. 4.18 to Figure. 4.21, the hysteresis loop shape prediction for both 304L and 321 SS was consistently good throughout the life.

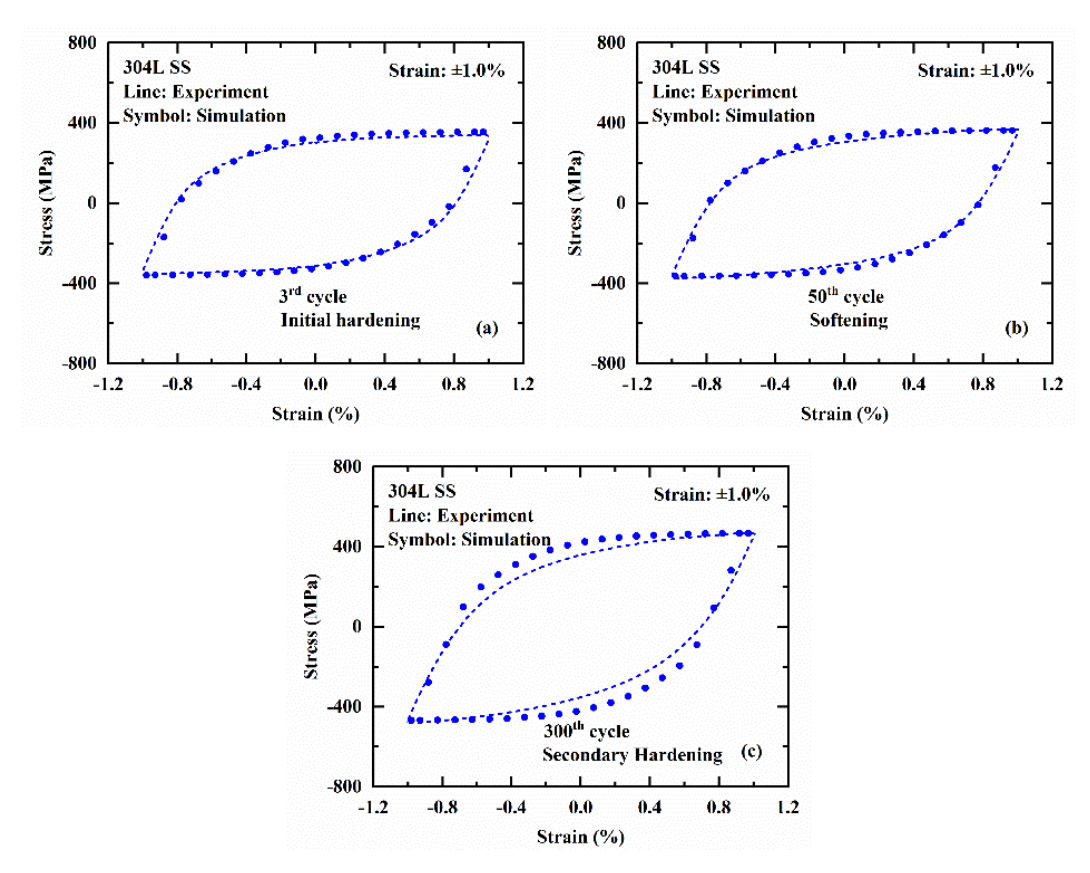


Figure. 4.18. Comparison of experimental and simulated hysteresis loops for 304L SS at $\pm 1.0\%$ strain amplitude.

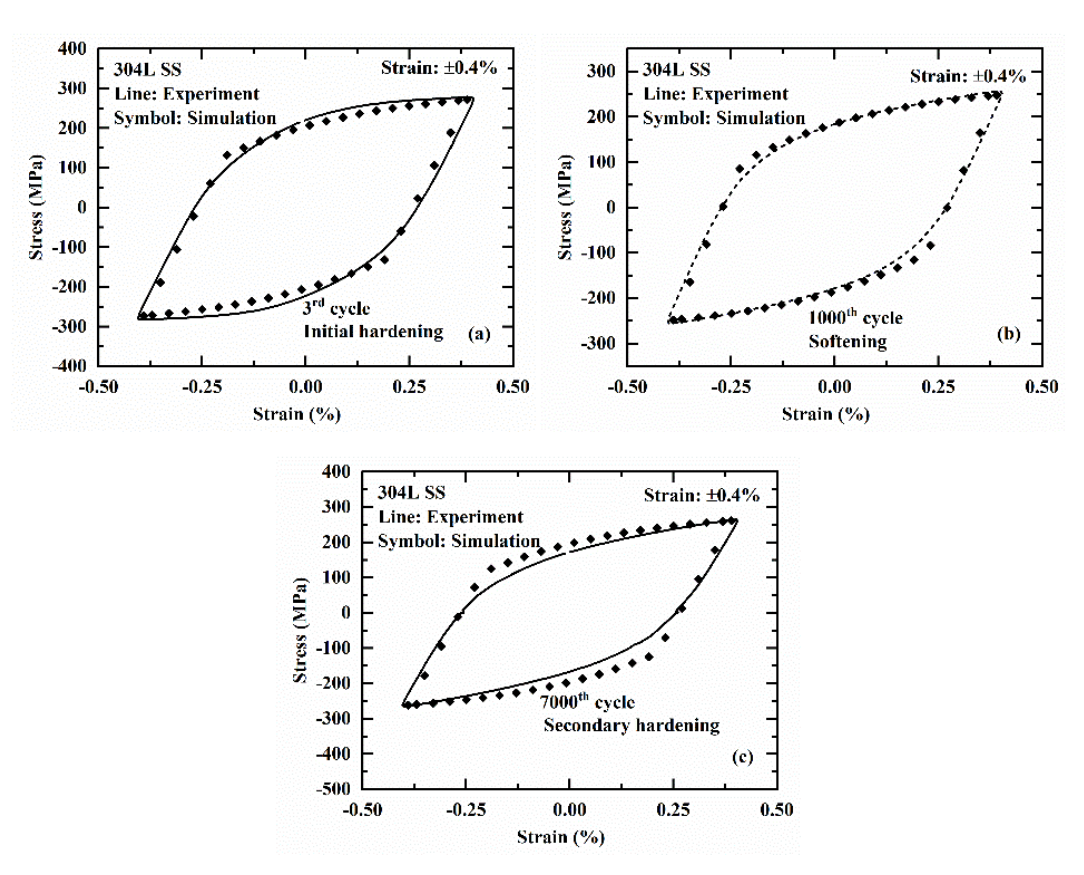


Figure. 4.19. Comparison of experimental and simulated hysteresis loops for 304L SS at $\pm 0.4\%$ strain amplitude.

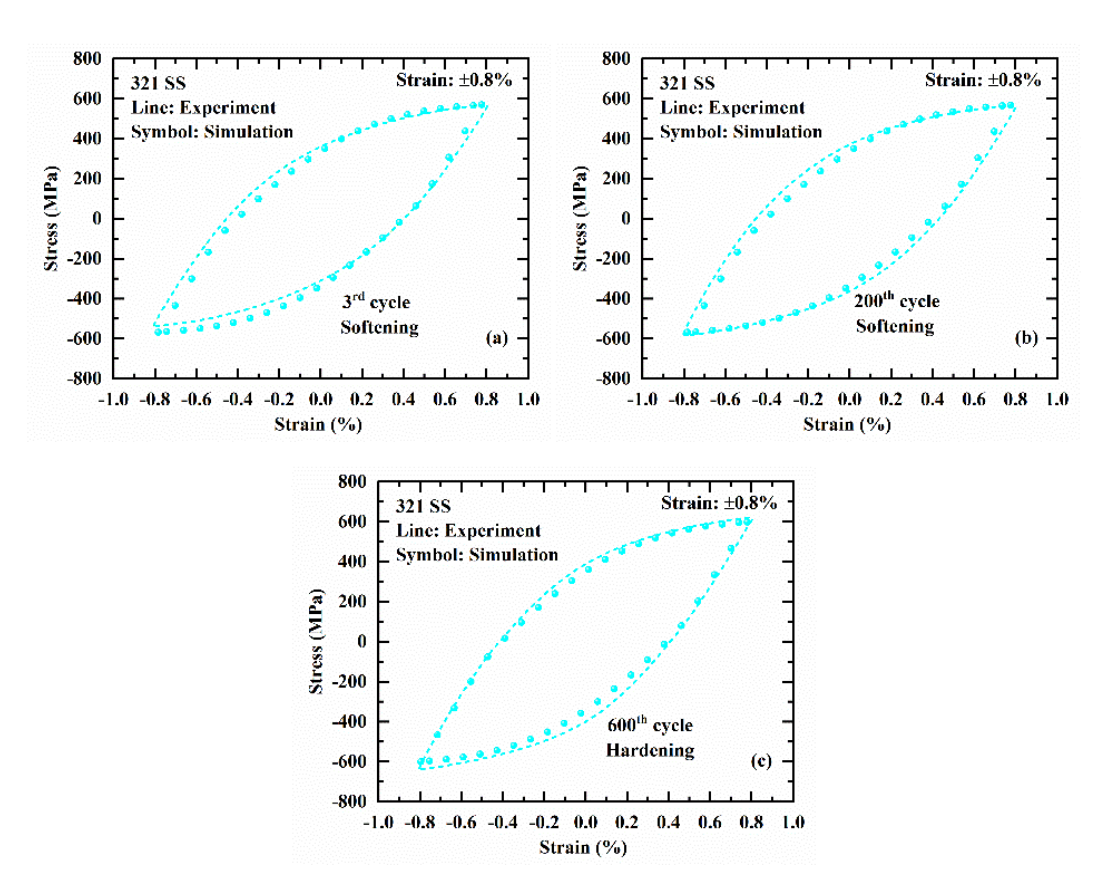


Figure. 4.20. Comparison of experimental and simulated hysteresis loops for 321 SS at $\pm 0.8\%$ strain amplitude.

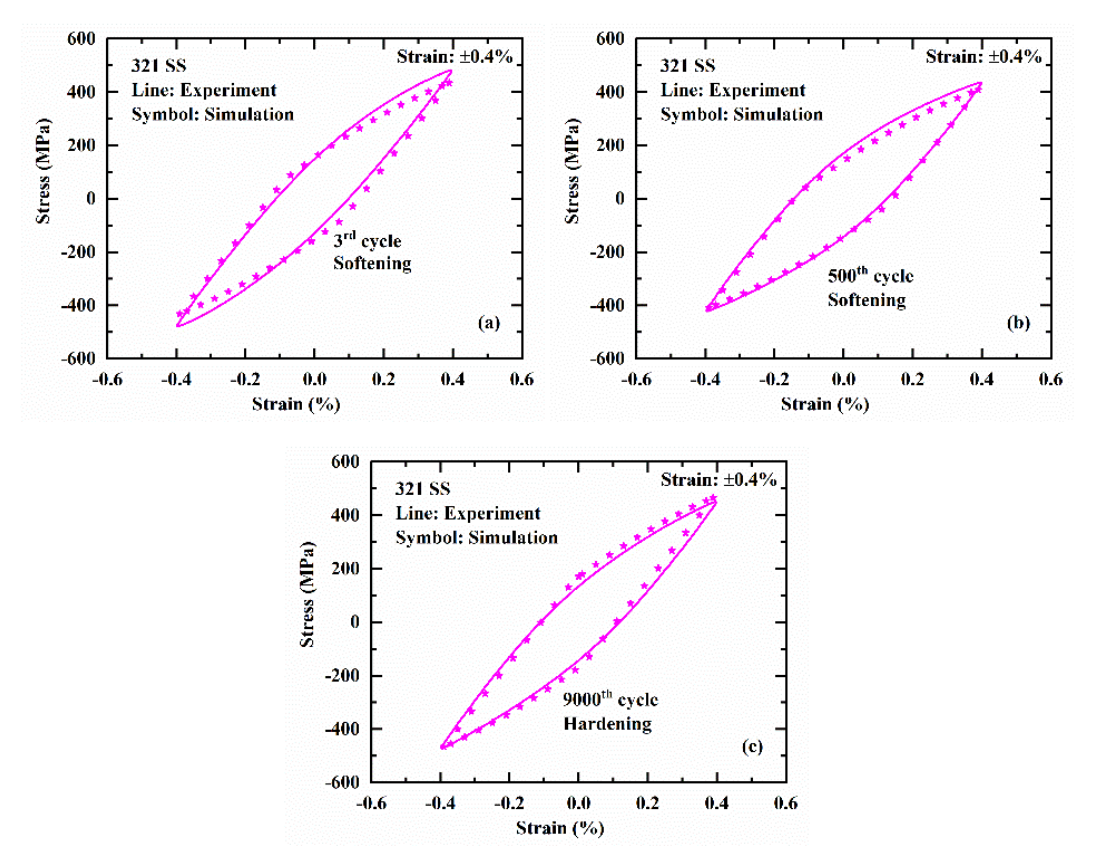


Figure. 4.21. Comparison of experimental and simulated hysteresis loops for 321 SS at $\pm 0.4\%$ strain amplitude.

4.5.2. Prediction capability of the model

The material parameters were identified and calibrated from the experimental data of the LCF tests conducted at strain amplitudes of $\pm 0.4\%$, $\pm 0.6\%$, $\pm 0.8\%$, and $\pm 1.0\%$ for 304L SS, and $\pm 0.4\%$, $\pm 0.5\%$, $\pm 0.6\%$, and $\pm 0.8\%$ for 321 SS. To verify the prediction capability of the proposed model and validate the material parameters determined from the test data, additional LCF tests are conducted at random strain amplitudes: $\pm 0.25\%$ for 304L SS and $\pm 0.45\%$ for 321 SS. The strain amplitudes are chosen such that they are not the same strain amplitudes at which the material parameters were determined. Then, LCF simulations are also performed at the strain amplitudes of $\pm 0.25\%$ for 304L SS and $\pm 0.45\%$ for 321 SS with the previously determined material parameters (given in Table 4.5). The simulated results are then compared with the experimental results. As can be seen, the model provides an excellent prediction of the peak stress variation with the number of cycles for both materials, as shown in Figure. 4.22. Figure. 4.23 shows a comparison of the hysteresis loops, plotted for different cycles, for 304L SS at $\pm 0.25\%$ strain amplitude. Similarly, Figure. 4.24 shows a comparison of the hysteresis loops, plotted for different cycles, for 321 SS at

 $\pm 0.45\%$ strain amplitude. As can be seen, the loop shape prediction is quite good for 321 SS; however, some deviation in the loop shape can be noticed for 304L SS. The error is highlighted in Figure. 4.23 estimates the difference between the areas of the simulated and experimental hysteresis loops. Such error can be minimized by considering multiple components of back stress, which defines the loop shape. However, we have considered only a single component of back stress while calibrating the material parameters. Moreover, it should be noted that 304L SS exhibited a significantly different cyclic behavior at $\pm 0.25\%$ strain amplitude, as evident from the absence of secondary hardening behavior, which is considered while calibrating the material parameters. The results presented in Figure. 4.22 to Figure. 4.24 highlight that to ensure consistent accuracy in the prediction, it is better to calibrate the material parameters within the minimum and maximum limits of strain amplitudes to which a component or structure would be subjected.

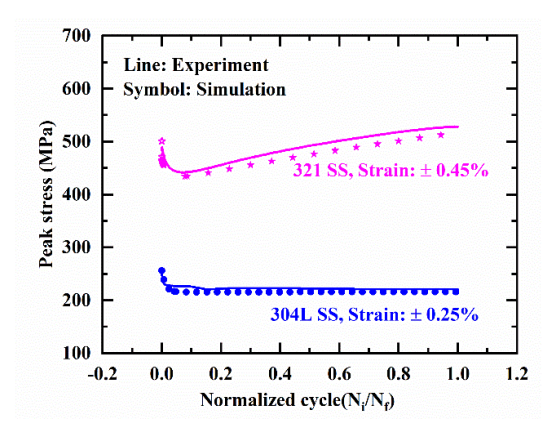


Figure. 4.22. Comparison of simulated and experimental results for cyclic peak stress variation at strain amplitudes of $\pm 0.25\%$ for 304L SS and $\pm 0.45\%$ for 321 SS.

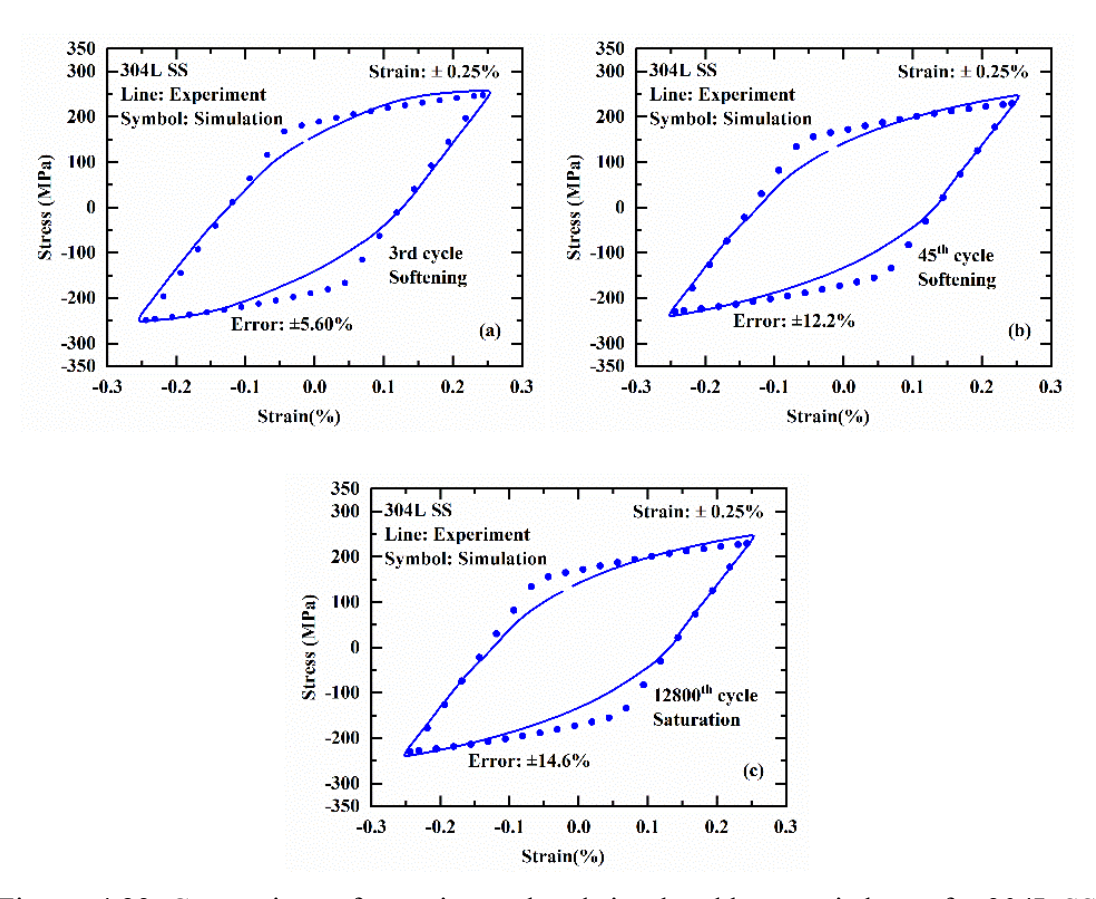


Figure. 4.23. Comparison of experimental and simulated hysteresis loops for 304L SS at $\pm 0.25\%$ strain amplitude.

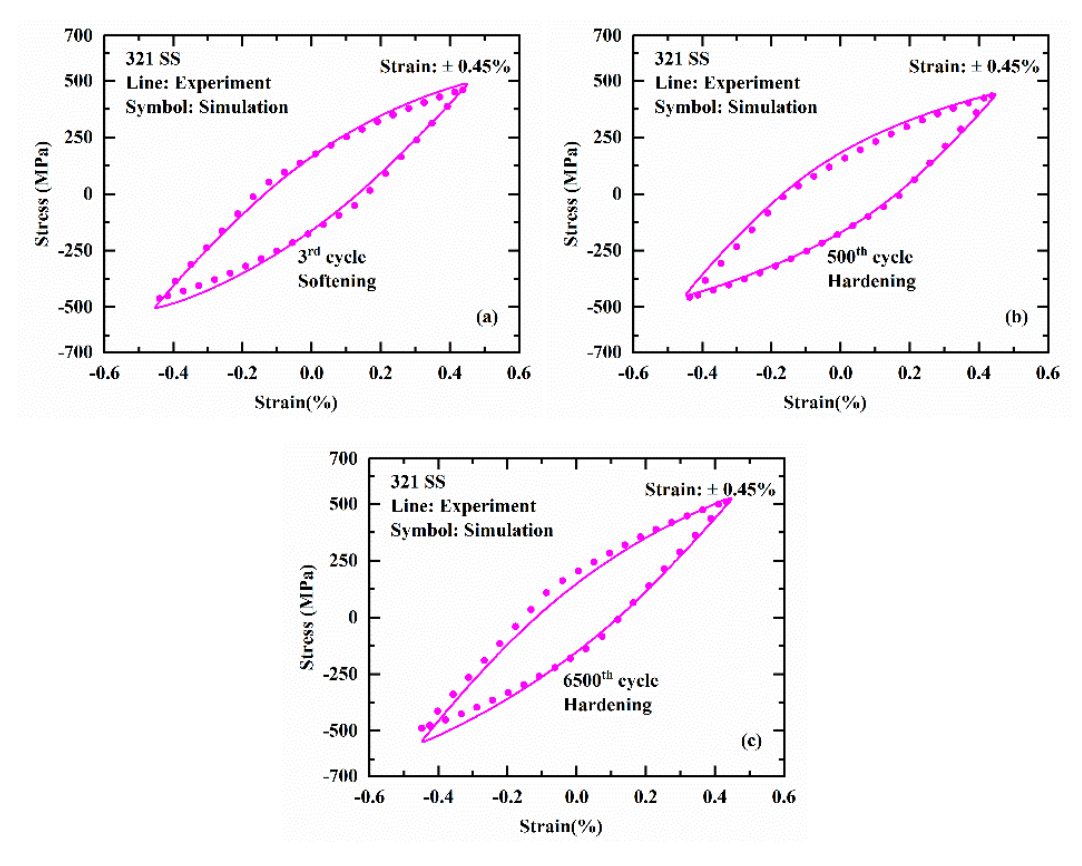


Figure. 4.24. Comparison of experimental and simulated hysteresis loops for 321 SS at $\pm 0.45\%$ strain amplitude.

4.6. Conclusions

Strain-controlled low-cycle fatigue tests performed at room temperature show that austenitic stainless steels 321 and 304L exhibit Type-I and Type-II non-Masing behaviors, respectively. The cyclic behavior of the material 321 SS exhibited initial softening followed by hardening, and 304L SS exhibited initial hardening followed by softening and secondary hardening.

A constitutive model, based on Chaboche's combined non-linear isotropic-kinematic hardening, is proposed to simulate the cyclic elastoplastic behavior of the materials along with their characteristic Type-I and Type-II non-Masing behaviors. The proposed constitutive model modifies the isotropic and kinematic hardening laws to take into account the strain range memory effect in the cyclic softening and hardening regions of 321 SS and softening and secondary hardening regions of 304L SS, as observed experimentally. The proposed model is implemented in the finite element analysis tool ABAQUS and validated with the LCF test results of 321 and 304L SS.

With the proposed modifications, the constitutive model is able to simulate the low cycle fatigue behavior, *i.e.*, 'peak stress' and 'hysteresis loop shape' variation with

cycling, for the whole life of 321 and 304L SS at different strain amplitudes. Moreover, the model is also able to accurately capture the Type-I and Type-II non-Masing behavior of the materials. The simulated results show an excellent agreement with the experimental results. The methodology of material parameter determination and calibration has also been explained in detail. It is expected that the modified model and methodology can be used to predict the LCF behavior of various steels.

Chapter 5: Quantification of the creep, fatigue, and oxidation damage and life prediction

Materials at high temperatures may undergo damage due to the interaction of creep, fatigue, and oxidation. Since the last decade, many methods have been developed to predict the life of the materials under creep-fatigue interaction (CFI) loading. However, oxidation damage is very rarely considered in such prediction models. Moreover, most of the methods available in the literature use a lot of testing and data acquisition from pure fatigue, creep-fatigue, and pure creep tests. To overcome these difficulties, this work investigates the net tensile hysteresis strain energy density method (THSED) available in the open literature. A modified THSED method that takes into account oxidation damage is proposed and implemented with four different materials for uniaxial CFI and hybrid CFI loading conditions. The proposed method could predict the CFI life of 304 SS, 304L SS, Mod. 9Cr-1Mo steel, and P92 steel within a scatter factor of ± 2.0 . The model parameter (γ_d) , determined by the hit and trial method in the existing THSED method, is found to be dependent on the oxidation damage, strain rate, and hold time. The analytical expressions for the estimation of THSED for U-CFI (Uniaxial creep-fatigue interaction) and H-CFI (Hybrid creep-fatigue interaction) loading conditions have also been derived

5.1. Introduction

The structural components used in automobiles, aero-engines, and nuclear/thermal power plants are usually made of ferritic, austenitic, martensitic steels and superalloys (Ni/Ti/Fe/Co-based) [191–194]. The components, such as heat exchangers, pipes, engines, rotor shafts, turbines, etc., operate at high temperature and pressure. Therefore, they undergo creep during operation and fatigue during start-up and shutdown [191,195].

The component behavior in the laboratory is usually investigated by uniaxial creep-fatigue interaction (U-CFI) test, *i.e.*, low cycle fatigue tests conducted with a hold time at tensile or compressive peak strain/stress. The U-CFI tests mainly focus on investigating the material's cyclic response, microstructural evolution, and useful life [196]. Fatigue damage is generally associated with transgranular cracking, as reported in the literature for different structural materials such as austenitic [175,197], ferritic-

martensitic [198], and Ni-based superalloy [199,200] materials. Whereas creep damage is generally associated with the formation of voids and intergranular cracking, as observed in the above mentioned materials [175,197–200]. However, the formation of voids and intergranular cracks are difficult to observe on the fracture surface of straincontrolled U-CFI tested specimens, as reported by Tang et al. [198] for martensitic and Wang et al. [201] for Ni-based superalloy materials. In a strain-controlled U-CFI test, the elastic strain energy stored in a material gets released during the period of strain hold, thereby, causing stress relaxation. Stress relaxation is associated with the transformation of elastic strain to creep strain. Thus, the introduction of strain hold during low cycle fatigue reduces the materials' life due to the development of creep damage. However, as the stress relaxation drops very rapidly in the initial period of hold and gets saturated, with the increase in hold time (typically beyond a few hundred seconds), there is a marginal increase in creep damage [57,202]. Thus, it becomes difficult to induce a variable extent of creep damage in strain-controlled U-CFI testing, whereas the extent of fatigue damage can be easily varied by varying the cyclic strain amplitude. The limitation arises as the elastic strain converts into plastic strain; the extent of creep damage that can be induced is limited and very minimal. The shortcomings of strain-controlled U-CFI testing are overcome by performing the hybrid (i.e. strain-controlled fatigue with stress hold) creep-fatigue interaction tests (H-CFI) [203– 205]. Under H-CFI, the extent of both the creep and fatigue damages can be varied.

During the hold time, creep damage occurs, which appears as intergranular or grain boundary cavitation [6]. While, during loading and unloading, fatigue damage occurs, which causes surface crack formation [6]. Also, the environment plays a critical role at high temperatures, as oxidation shortens the crack initiation period; as verified experimentally through microscopic observations [6,206,207]. The interaction of creep, fatigue, and oxidation damage promotes change from trans-granular cracking to intergranular cracking; thus, usually, a mixed-mode type damage occurs [208]. The synergetic interaction of the creep, fatigue, and oxidation at high temperatures leads to accelerated failure of the components [19–22]. The oxidation degrades the material's performance by diffusion of oxygen and subsequent chemical reactions with the parent material [209,210]. It is considered a surface and sub-surface phenomenon dependent on time and temperature [21,23–27]. Thus, accurate life prediction considering creep, fatigue, and oxidation under different loading conditions and strain paths is critical and

necessary for the successful operation of the real components at elevated temperatures for the desired lifetime.

Until now, many efforts have been made to predict the damage mechanism and failure life using creep-fatigue testing. Most methods to predict fatigue life are based on the Coffin-Manson relationship and its modification [67–69]. The time fraction (TF) rule [70] and ductility exhaustion (DE) method [71–73] are used mainly for the calculation of creep damage. The recent methods [76–78] use the so-called strain energy density exhaustion (SEDE), i.e., a criterion based on the area of the hysteresis loop corresponding to the hold time, to accurately predict the creep damage as a proposed by Takahashi [74]. Further, Takahashi [75] modified the strain energy density exhaustion (SEDE) method based on the criterion that the high rate of inelastic deformation at the start of hold time is less harmful than the remaining period (i.e., before saturation in stress relaxation is achieved) and predicted the creep-fatigue life more accurately within the scatter factor of ± 3 for various materials. Wang et al. [76,77] considered the effect of mean stress on creep damage accumulation and modified the creep damage calculation based on the modified SEDE model proposed by Takahashi [75] and predicted the creep-fatigue life within the scatter factor of ± 2 for various materials. Zhu et al. [211,212] conducted systematic investigations to take into account the effects of mean stress, hold time, and waveform on the strain energy density exhaustion criterion and characterized different materials' low cycle fatigue-creep behaviors.

For the tensile hold, Song *et* al. [78] considered the effect of mean stress on fatigue damage calculation and the effect of threshold stress on creep damage. The creep damage is found to accumulate significantly only when the applied stress is more than the threshold stress. They modified the creep and fatigue damage equations proposed by Wang *et* al. [76,77], to take into account the threshold stress and mean stress effect, respectively. The models mentioned above have the drawback that they require a large number of fatigue, creep-fatigue interaction, and creep test data to identify model parameters to predict the lifetime of the material.

While investigating the effect of oxidation damage, Coffin [213] observed that oxidation damage is more when the frequency of cycling is low and vice-versa. Thus, to take into account the oxidation effect, he introduced a frequency factor in the Coffin-Manson equation. Reuchet and Remy [25] studied the effect of fatigue loading on

oxidation kinetics and proposed oxidation damage based on the microstructure evaluation and propagation of the crack. Neu and Sehitoglu's [26,27] model contained separate components of creep, fatigue, and oxidation, in which the expression of oxidation damage was associated with strain range, strain rate, repeated micro-rupture of the oxide, and oxidation kinetics. Phasing term in the model, i.e., the ratio of thermal strain rate to mechanical strain rate, requires many tests. Takahashi [74] used a life reduction ratio to assess the effect of oxidation in ferritic steel during compressive hold fatigue. It predicts the lifetime of material within the scatter factor of ± 2 . The model does not explicitly consider the temperature dependence of oxidation damage. The type 1 damage, only the surface of the material gets oxidized, while in type 2, the surface and subsurface regions are oxidized due to cracking of the oxide layer formed at the surface. They pointed out that compressive hold fatigue is more harmful than tensile hold fatigue for ferritic steels due to type 2 damage. They also predicted the lifetime of the material for compressive hold fatigue by considering the crack initiation and propagation lives. The drawback of this approach is that it requires a large number of parameters and the accurate measurement of crack density to predict a lifetime with the suggested model. Also, the procedure to obtain them is complex. Wang et al. [76] considered the oxidation effect by modifying Agatonovic's [214] oxidation damage as surface and sub-surface phenomena for compression hold creep-fatigue test only for ferritic steel. They predicted that under the compression hold creep-fatigue test, the predicted life of the material lies within a scatter factor of ± 1.5 . The model predicts the lifetime of material with considerable accuracy. Lately, Song et al. [28] have taken into account the oxidation damage as surface and sub-surface phenomena in modified SEDE method by a non-linear interaction of the creep, fatigue, and oxidation damage to predict the life of the material undergoing U-CFI and H-CFI loading. They predicted the life of 304SS and Grade 91 steel within the scatter factor of ± 3.0 .

Many methods are available in the open literature to predict material life at high temperatures depending on the loading, strain waveform, and environmental conditions. Most of the methods predict material life within a scatter factor of ± 2.0 or more. Moreover, they use complicated fitting procedures with many model parameters. To reduce the number of model parameters, Wang et al. [30] recently proposed the so-called net tensile hysteresis strain energy density (THSED) method for predicting the creep-fatigue life of materials. The model considers the synergistic interaction of fatigue and creep damages in terms of the plastic strain energy absorbed by the material during

loading-unloading and hold time, respectively. Creep-fatigue life exhibits the power-law relation with total tensile hysteresis strain energy density. The co-relation contains the model parameter (γ_d) , which is found by the hit and trial method by Wang et al. [30]. They did not explain the physical significance of the model parameter (γ_d) . It has been used as a material constant.

The present investigation focuses on analyzing creep, fatigue, and oxidation damages and their interactions to predict material life. The oxidation kinetics approach is considered for calculating the oxidation damage considering it as surface and subsurface phenomena. Interestingly, while analyzing the oxidation damage for different materials, it is observed that the model parameter (γ_d) used by Wang et al. [30] can be estimated as the ratio of oxidation damage (neglecting the time effect) to strain rate. Thus, we propose the modified THSED method, considering the (γ_d) as a physical parameter rather than a number found by the hit and trial method. The parameter is found to be dependent on the oxidation damage, strain rate, and hold time of the CFI test. The functional relationship between these parameters and γ_d has also been established. The proposed modified THSED method is extended to hybrid (H-CFI) stress-strain control loading conditions. The model is validated for the austenitic and ferritic stainless steel for different loading conditions. Experimental data for validating the modified THSED method is collected from various articles [215-217]. The prediction capability of the proposed modified-THSED model is compared with modified SEDE (oxidation damage) [28] and THSED [30] models available in the open literature. It is observed that the prediction accuracy lies in a scatter factor of ± 3 for the modified SEDE and the THSED model, which is reduced to a scatter factor of ±2 for the proposed modified THSED model.

5.2. Life prediction methods

5.2.1. THSED method for axial loading

The THSED method proposed in article [30] considers the fatigue damage stress (σ_d) and elastic strain energy density effect along with the plastic strain energy density and creep strain energy density for the estimation of total tensile hysteresis strain energy density. The plastic strain energy density takes into account of the fatigue damage caused during the loading-unloading duration. The creep strain energy density takes into account creep damage caused during the hold time. The plastic and creep energy

densities may lead to crack initiation and propagation. The tensile elastic strain energy density is introduced as it may facilitate crack propagation.

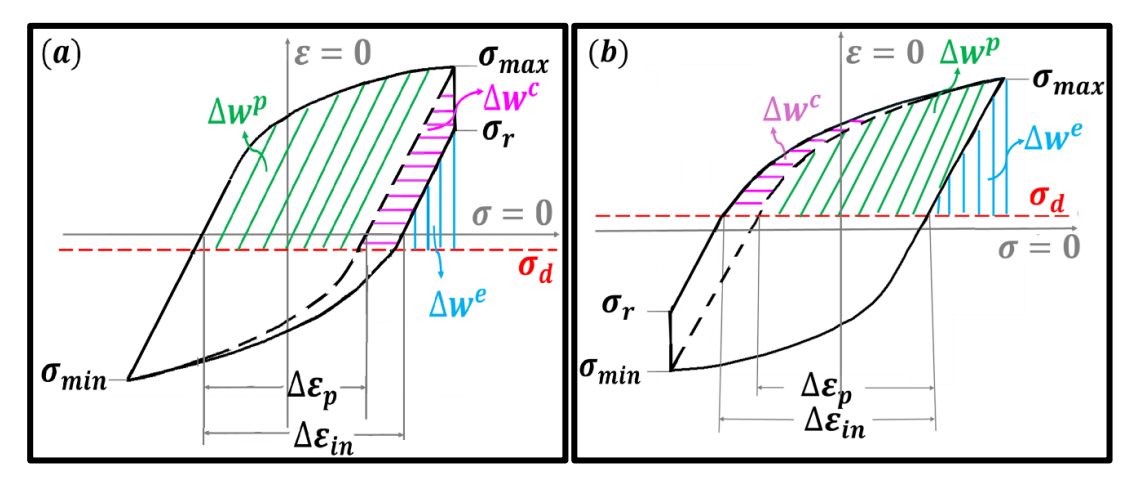


Figure 5.1. Shaded area represents THSED for U-CFI loading (a) tension hold and (b) compression hold.

Wang et al. [30] defined the fatigue damage stress σ_d as given by Eq. (5.1), based on the crack opening concept.

$$\sigma_d = \gamma_d \sigma_m \tag{5.1}$$

$$\sigma_m = (\sigma_{max} + \sigma_{min})/2 \tag{5.2}$$

Here, σ_m is mean stress, σ_{max} is the tensile peak stress, σ_{min} is the compressive peak stress, and γ_d is a material parameter found by hit and trial method.

Total tensile hysteresis strain energy density is the effective energy density that causes the crack to advance and is given as the area under the stress-strain hysteresis loop above the fatigue damage stress, σ_d . It is dependent on the mean stress through the parameter γ_d , as shown by the shaded area in Figure 5.1. and given by Eq. (5.3).

$$\Delta w^t = \Delta w^p + \Delta w^c + \Delta w^e \tag{5.3}$$

The equation for the estimation of plastic strain energy density (Δw^p) was originally proposed by Halford [218]. Skeleton [65,219] has further used it for U-CFI along with strain energy density due to creep (Δw^c) and elastic recovery (Δw^e) . Wang et al. [43] further modified the equations used by Skeleton by considering the effect of the fatigue damage stress (σ_d) , as shown by Eq. (5.4) to Eq. (5.9). Finally, used the well-known power law [220] relationship, given by Eq. (5.9), for predicting the creep-fatigue life of the material.

$$\Delta w^p = \frac{1 - n'}{1 + n'} \sigma_{max} \Delta \varepsilon_p - \sigma_d \Delta \varepsilon_p \text{ for tensile \& compressive hold}$$
 (5.4)

$$\Delta w^{c} = \frac{\sigma_{max}^{2} - \sigma_{r}^{2}}{2E} + \sigma_{d} \left(\Delta \varepsilon_{in} - \Delta \varepsilon_{p} \right)$$
 for tensile hold (5.5)

$$\Delta w^{e+} = \frac{(\sigma_r - \sigma_d)^2}{2E} \text{ for tensile hold}$$
 (5.6)

$$\Delta w^{c} = \frac{(\sigma_{max} - \sigma_{d})(\Delta \varepsilon_{in} - \Delta \varepsilon_{p})}{2} \text{ for compressive hold}$$
 (5.7)

$$\Delta w^e = \frac{(\sigma_{max} - \sigma_d)^2}{2E} \text{ for compressive hold}$$
 (5.8)

$$N_{pre} = a(\Delta w^t)^b \tag{5.9}$$

5.2.2. THSED method extended to H-CFI

The THSED method proposed by Wang et al. [30] for U-CFI life prediction is extended to the hybrid creep-fatigue interaction (H-CFI). Figure 5.2 schematically represents the hysteresis loops for tension and compression stress hold H-CFI test, and the shaded area represents the tensile hysteresis strain energy density. The THSED for tension and compressive hold is calculated by using Eq. (5.3) to Eq. (5.8), but Eq. (5.10) is used instead of Eq. (5.5) to calculate the creep part of energy density Δw^c and Eq. (5.11) is used instead of Eq. (5.6) for the elastic component of energy density Δw^c . Once Δw^t is calculated, the H-CFI life is predicted using Eq. (5.9). The model parameter (γ_a) is calculated using Eq. (5.27) and (5.28) (in the proposed in this article). The parameters a and b were obtained by fitting Eq. (5.9) to the experimental creep-fatigue life variation with total tensile strain energy density for various materials.

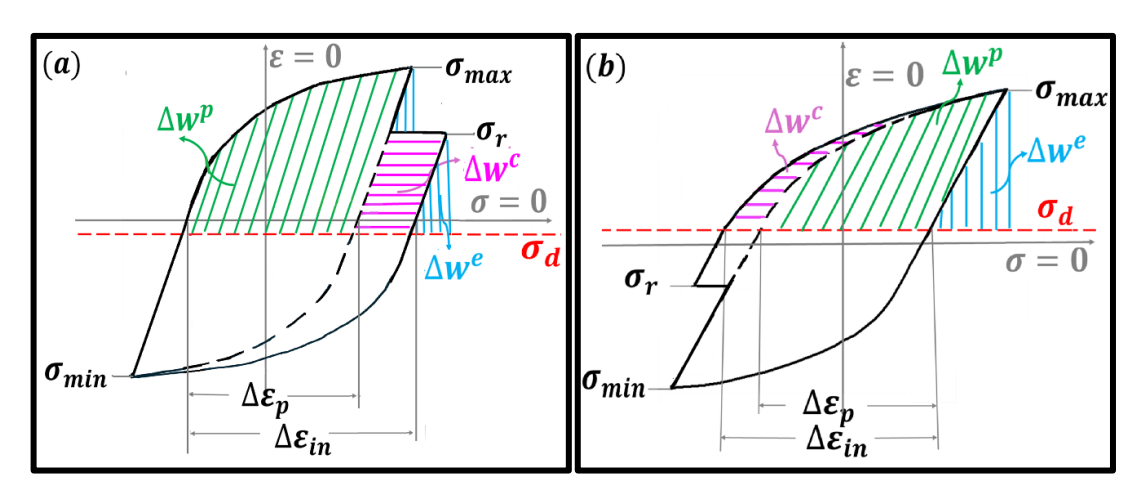


Figure 5.2. Shaded area represents THSED for H-CFI loading (a) tension stress hold and (b) compression stress hold.

$$\Delta w^{c} = (\sigma_{r} - \sigma_{d}) (\Delta \varepsilon_{in} - \Delta \varepsilon_{p}) \text{ for tensile stress hold}$$
 (5.10)

$$\Delta w^e = \frac{(\sigma_{max} - \sigma_r)^2}{2E} + \frac{(\sigma_r - \sigma_d)^2}{2E} \text{ for tensile stress hold}$$
 (5.11)

5.2.3. Modified SEDE method

The modified SEDE (strain energy density exhaustion) method proposed by Song et al. [28] is based on Eq. (5.12) proposed by Skeleton and Gandy [66] to estimate the total damage by considering non-linear interaction of fatigue (D_f) , creep (D_c) , and oxidation (D_0) damage. The creep-fatigue life (N_{pre}) is predicted using Eq. (5.13). In existing literature, only this method takes oxidation damage into account to predict the creep-fatigue life of material under strain-controlled U-CFI and H-CFI loading conditions. Thus, in the current investigation, the creep-fatigue life is also predicted by using the 'modified SEDE method'. The values of the various material parameters required for the creep-fatigue life prediction are usually estimated from pure fatigue, creep-fatigue, and pure creep test data. The method is highlighted by the mathematical expressions in Eq. (5.12) to Eq. (5.20) [28] and is implemented in Section 5.4.2 to compare the creep-fatigue life prediction with the other two methods.

$$D_{cf} = \frac{D_c}{1 - D_f - D_o} + \frac{D_f}{1 - D_c - D_o} + D_o$$
 (5.12)

$$N_{pre} = \frac{1}{D_{cf}} \tag{5.13}$$

$$D_f = \left(\frac{C(1+n')}{(1-n')\sigma_{max}\Delta\varepsilon_p + 2n'\sigma_m\Delta\varepsilon_p}\right)^{\delta}$$
 (5.14)

$$w_f = \frac{w_{f,max} + w_{f,min} \left(\sigma/\sigma_{y0} + B\right)^{-\kappa}}{\left(\sigma/\sigma_{y0} + B\right)^{-\kappa} + 1}$$
(5.15)

$$\sigma(t) = \frac{\sigma_{max} \exp\left(-\dot{\varepsilon}^* E t / \sigma^*\right)}{\left(1 + \left(\frac{\sigma}{\sigma^*}\right)^{m^* - 1} \left(1 - \exp\left(t - -\dot{\varepsilon}^* E t / \sigma^*\right)\right)\right)^{(1/m^* - 1)}}$$
(5.16)

$$\dot{\varepsilon}_{cr} = -\frac{\dot{\sigma}}{E} = -\frac{1}{E} \frac{d\sigma}{dt} \tag{5.17}$$

$$\dot{w} = \dot{\varepsilon}(\sigma - \sigma_{th}) \tag{5.18}$$

$$D_c = \int_0^{t_h} \frac{\dot{w}}{w_f(\dot{w}, T)} - \frac{\dot{w}}{w_{f,max}(\dot{w}, T)} dt$$
 (5.19)

$$D_o = \left(\frac{x_w - x_i}{x_w}\right)^{\beta} \int_0^t 0.5 \sqrt{k_p} \, t^{-0.5} dt \tag{5.20}$$

The mean stress effect on fatigue damage is considered by Eq. (5.14). To evaluate creep damage, the creep strain energy is calculated considering that the stress above the threshold stress only causes positive creep accumulation, as shown Eq. (5.18). It is supported by intermediate steps outlined in Eq. (5.15) through Eq. (5.17). Once the creep strain energy density is obtained, creep damage is calculated using Eq. (5.19). The oxidation damage that occurs in each cycle is determined using Eq. (5.20).

5.3. Oxidation damage above

The total damage from oxidation in a material is due to surface and subsurface oxidation phenomena. The overall oxidation damage (D_o) as a function of exposure time can be represented by Eq. (5.21), as reported by Nikbin and Bilgari [23,24]. In Eq. (5.21) k_p represents the oxidation constant. The 'damage index' (i.e. D_{index} in Eq. (5.22)) represents the normalized distribution of oxidation damage from the surface to the sub-surface. The parameter x_i represents the distance of any point in the material from the oxidized surface, while x_w represents the geometric length of the material. The estimate of x_w will depend on the geometry of the test specimen, e.g., to study the oxidation damage distribution for a cylindrical specimen, x_w can be considered as the radius of the specimen. The exponent β defines the shape of the damage profile, which depends on time, temperature, and material.

$$D_o = D_{index} \int_0^t 0.5 \sqrt{k_p} \, t^{-0.5} dt \tag{5.21}$$

$$D_{index} = \left(\frac{x_w - x_i}{x_w}\right)^{\beta} \tag{5.22}$$

5.3.1. Proposed damage index

As the diffusion of oxygen causes oxidation damage, the present work considers the oxygen concentration variation with depth for the assessment of oxidation damage, as shown in Figure 5.3 for different steels. The data plotted in Figure 5.3 is extracted

from the literature [221–225]. Nikbin and Bilgari [23,24] considered the micro-hardness variation with depth for the assessment of oxidation damage or defining the damage index parameter, as diffusion of oxygen, which causes oxidation, also increases the hardness of a material. However, under low cycle fatigue, the hardness of a material in real components under service conditions may also increase due to various other reasons, e.g., deformation-induced phase transformation [226], diffusion of hydrogen or nitrogen [227], neutron irradiation [228], etc. Thus, this article proposes to use the oxygen concentration profile for the oxidation damage index. For P91 steel [229], Haynes 230 [230], and Alloy 617 [221], the oxygen concentration distribution with depth, as obtained from the oxidation experiment in air, is observed to have an exponential variation, as shown in Figure 5.3 and given by Eq. (5.23).

$$D = D' + A \exp(rx) \tag{5.23}$$

$$D_{index} = \frac{D}{D_{max}} \tag{5.24}$$

Eq. (5.23), x represents the depth along which oxygen concentration varies. In the current investigation, D_{index} is calculated by using Eq. (5.24), where D_{max} is the maximum value of the oxygen concentration at the surface. The constants D', A, and r are material, temperature, and time dependent parameters. Mathematically, D' and A in Eq. (5.23) represent the maximum value and scaling factor, respectively. Thus, the value of D' + A gives an estimate of the maximum oxygen concentration at the surface (x = 0), and r indicates the rate at which the concentration varies with depth. The values of D_0 , A and r were found by fitting Eq. (5.24) to the oxygen concentration vs depth data, shown in Figure 5.3. The values are given in Table 5.1.

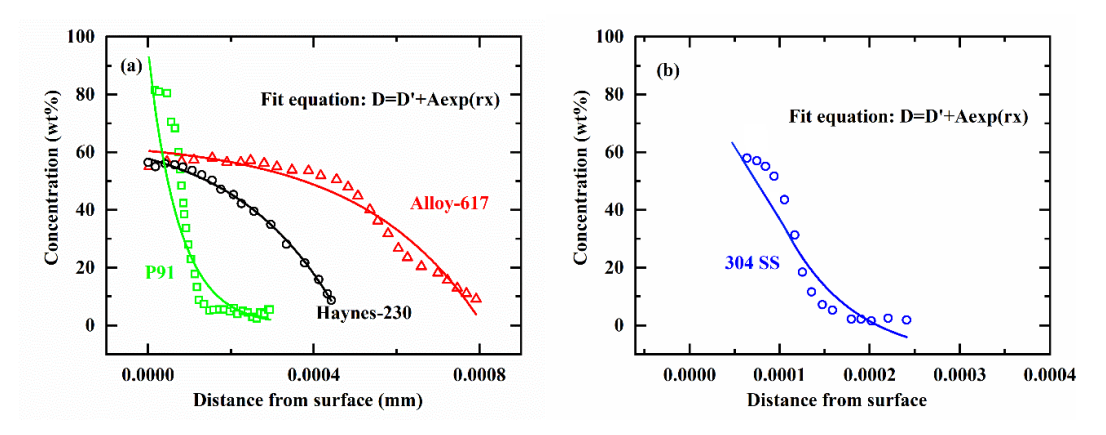


Figure 5.3. Oxygen content (wt.%) variation with depth (mm) [221,229–231] (Note: for P91 steel, to determine the material parameters (D' and A), the saturated value of oxygen concentration is assumed to be 80% at the surface).

Table 5.1: Estimated values of material parameters for damage index, Eq. (5.24)

Material	Temperature (°C)	D' (wt.%)	A (wt.%)	r (mm)
Alloy 617 [221]	850	53.042	-0.299	3834.26
Haynes 230 [230]	850	67.486	-9.711	4078.23
P91 [229]	550	0.125	94.609	-13339.903
Inconel 625 [232]	815	87.754	-1.227	144.1833

5.4. Results and discussion

5.4.1. Oxidation damage model

In a material under creep-fatigue loading, oxidation damage occurs during the loading, unloading, and hold period. Moreover, as reported by Coffin [213], the severity of oxidation damage during fatigue increases with a decrease in the frequency of cyclic loading; thus making oxidation an important concern for creep-fatigue interaction life prediction as well. Motivated by the findings of Coffin [213], the overall oxidation damage in the present investigation is considered to be inversely proportional to the strain-rate ($\dot{\varepsilon}$) of cyclic loading. Hence, Eq. (5.21) is redefined by Eq. (5.25) to take into account the strain rate effect. Further, if we neglect the effect of time, the overall oxidation damage represented by Eq. (5.25) can be rewritten as Eq. (5.26).

$$D_0^{mod} = D_O/\dot{\varepsilon} \tag{5.25}$$

$$D_0' = \left(D_0/\sqrt{t}\right)/\dot{\varepsilon} = \sqrt{k_p(D_{index}/\dot{\varepsilon})}$$
 (5.26)

Based on the estimate of D'_0 corresponding to the geometrical extent of oxidation damage, the model parameter γ_d is found to be related to D'_0 , as shown in Eq. (5.27). The values of γ_d obtained by using Eq. (5.27) for different materials are compared with the values of γ_d as reported in article [30] for different materials and is shown in Table 5.2.

$$\gamma_d = 100 \times D_0' \tag{5.27}$$

Interestingly, the model parameter (γ_d) estimated by using Eq. (5.27) for different materials is very closer to the values reported by Wang et al. in [30]. It should be noted that Wang et al. [30] estimated the values of γ_d by hit-and-trial method;

however, Eq. (5.27) phenomenologically describes its dependence on the oxidation damage and the strain rate of cyclic loading.

Table 5.2: Estimated parameters of the oxidation damage equations and comparison of parameter γ_d

Material	Temp.	έ (%/s)	$D_o/t^{0.5}$	$k_p (\text{mg}^2\text{mm}^{-1})$	D_0^{mod}	γ _d in [30]	γ_d from Eq. (5.27)
Alloy 617	850	0.1	1.27×10^{-4}	9.92×10^{-11}	0.127	11.7	12.7
Alloy 617	850	0.025	7.67×10^{-5}	9.92×10^{-11}	0.304	30	30.43
Haynes 230	850	0.025	3.35×10^{-7}	7.04×10^{-12}	0.0013	0.1	0.13
P91	550	0.1	2.99×10^{-5}	6.89×10^{-9}	-0.029	-2.2	-2.33
Inconel 625	815	1.0	3.52×10^{-5}	2.3×10^{-10}	0.003	0.3	0.3

As can be seen in Table 5.2, the value of γ_d is less for alloy 230 compared to the other materials, which indicates better oxidation resistance of alloy 230 compared to the other materials. The effect of creep and oxidation on Ni-based superalloys such as alloy 617, Haynes 230, and Inconel 625 have been studied by many authors [8,232,233]. These studies report Alloy 230's better creep-fatigue performance due to improved oxidation resistance under creep-fatigue loading. The better oxidation resistance is attributed to the formation of a duplex oxide layer (Outer MnCr₂O₄ and inner Cr₂O₃), which prevents the oxygen from penetrating further into the material, thus reducing the oxidation damage [8,233]. Further, the estimated values of γ_d (as seen in Table 5.2 for alloy 617) increase with a decrease in the strain rate, thus correctly explaining the detrimental effect of decreasing strain rate on oxidation damage, as experimentally observed by Coffin [213].

The shaded areas in Figure 5.1 show the THSED for a positive value of γ_d , indicating that tensile hold is more detrimental than compression hold, as the tensile hysteresis strain energy density is more in each cycle with tensile hold. Most of the austenitic stainless steels [234] and Ni-based superalloys [208] show similar behavior, which causes lower creep-fatigue interaction life with tension hold compared to compression hold. However, for ferritic-martensitic steel (P91), compression hold is reported to be more detrimental than tension hold during cyclic loading [21,235]. Thus, the negative value of γ_d for P91 in Table 5.2 indicates the opposite behavior of P91 steel observed experimentally [21,235].

5.4.2. Implementation of modified THSED model and lifetime prediction

In Section 5.4.1, the model parameter γ_d (defined by Eq. (5.27)) depends on the temperature and strain rate only, as the oxidation damage defined by Eq. (5.26) does not take into account the time effect. It was done to compare the values of γ_d estimated using Eq. (5.27) (proposed in the current study) with the values of γ_d given by Wang et al. in [30]. However, oxidation is a time-dependent phenomenon [23,24]. The oxidation effect in different materials such as Ni-based superalloys [199], austenitic steel [234], and ferritic-martensitic steel [21,235] under creep-fatigue loading is found to increase with an increase in hold time. Thus, in the case of creep-fatigue loading, the effect of time (especially the hold time) on oxidation damage cannot be avoided. Therefore, considering the oxidation damage as a time, temperature, and strain-rate dependent phenomenon, as defined by D_0^{mod} in Eq. (5.26), the parameter γ_d (of Eq. (5.27)) is redefined as γ^{mod} given by Eq. (5.28). Similar to D_0' , the D_0^{mod} corresponding to the geometrical extent of oxidation damage is considered for the estimation of γ^{mod} .

$$\gamma^{mod} = 100 \times D_0^{mod} \tag{5.28}$$

In the current investigation, the creep-fatigue life prediction is done by estimating the model parameter γ_d by Eq. (5.27) and also by Eq. (5.28). As the values of γ_d estimated using Eq. (5.27) are almost the same as given in article [50], as shown in Table 2, the creep-fatigue life prediction done by estimating the value of γ_d by Eq. (5.27) is termed in this investigation as **'THSED method'**. While the creep-fatigue life prediction done by estimating the value of γ_d by Eq. (5.28) (i.e. γ^{mod}) is termed as the **'modified THSED method'**.

For the implementation of the proposed methods for CFI life prediction, the half-life hysteresis loop data (i.e., $\Delta \varepsilon_{in}$, $\Delta \varepsilon_{p}$, σ_{max} , σ_{r}) and N_{exp} , n', and E for 304SS [215], 9Cr-1Mo steel [216] and P92 [217] were obtained from the literature, as given in Table 3. For 304L SS, the test data were obtained by conducting U-CFI experiments on a BISS (UT-20-0100) 100 kN servo-electric fatigue testing machine.

The implementation of the **'THSED method'** for creep-fatigue life prediction is explained below:

- Step-1: Determined the half-life hysteresis loop data (i.e., $\Delta \varepsilon_{in}$, $\Delta \varepsilon_{p}$, σ_{max} , σ_{r}) and N_{exp} , n', and E.
- Step-2: Mean stress σ_m is calculated using Eq. (5.2).
- Step-3: The material parameters D', A and r are obtained by fitting Eq. (5.23) to the 'oxidation data,' as shown in Figure 5.3. The oxidation data (the oxygen concentration (wt.%) distribution with distance from the surface) and the values of oxidation rate constant (k_p) were obtained from the literature [229].
- Step-4: D_{index} is calculated using Eq. (5.24). For the calculation, D_{max} (the maximum oxygen concentration) value is obtained at x = 0 from Figure 5.3, and the value of D is obtained using Eq. (5.23) with the estimated values of D', A and r.
- Step-5: D_0^{mod} is calculated using Eq. (5.25).
- Step-6: D'_0 is calculated using Eq. (5.26).
- Step-7: Model parameter γ_d is obtained using Eq. (5.27).
- Step-8: Fatigue damage stress σ_d is obtained using Eq. (5.1).
- Step-9: Tensile hysteresis strain energy density (Δw^t) is calculated from the half-life hysteresis loops data using Eq. (5.3). The Δw^p , Δw^c , and Δw^e are calculated as described in Section 5.2.1 for U-CFI and Section 5.2.2 for H-CFI loadings depending on the condition of tension hold and compression hold.
- Step-10: The material parameters a and b are found by fitting Eq. (5.9) to the experimental creep-fatigue life (N_{exp}) (obtained in step-1) vs. Δw^t data, as shown in Figure 5.4.
- Step-11: Finally, the creep-fatigue life (N_{pre}) of the materials is predicted using Eq. (5.9) with the estimated values of Δw^t and materials parameters a and b.

The implementation of the 'modified THSED method' for creep-fatigue life prediction will follow similar steps as mentioned above for the 'THSED method', except for the differences highlighted below.

- Step-1 to Step-5: Similar to the THSED method.
- Step-6: Not required.
- Step-7: Estimate the model parameter γ^{mod} using Eq. (5.28).
- Step-8: Fatigue damage stress σ_d is obtained using γ^{mod} instead of γ_d in Eq. (5.1).
- Step-9 to Step-11: Similar to the THSED method.

The material parameters used for the creep-fatigue life prediction of the materials by the THSED method and modified THSED method are given in Table 5.4 and Table 5.5.

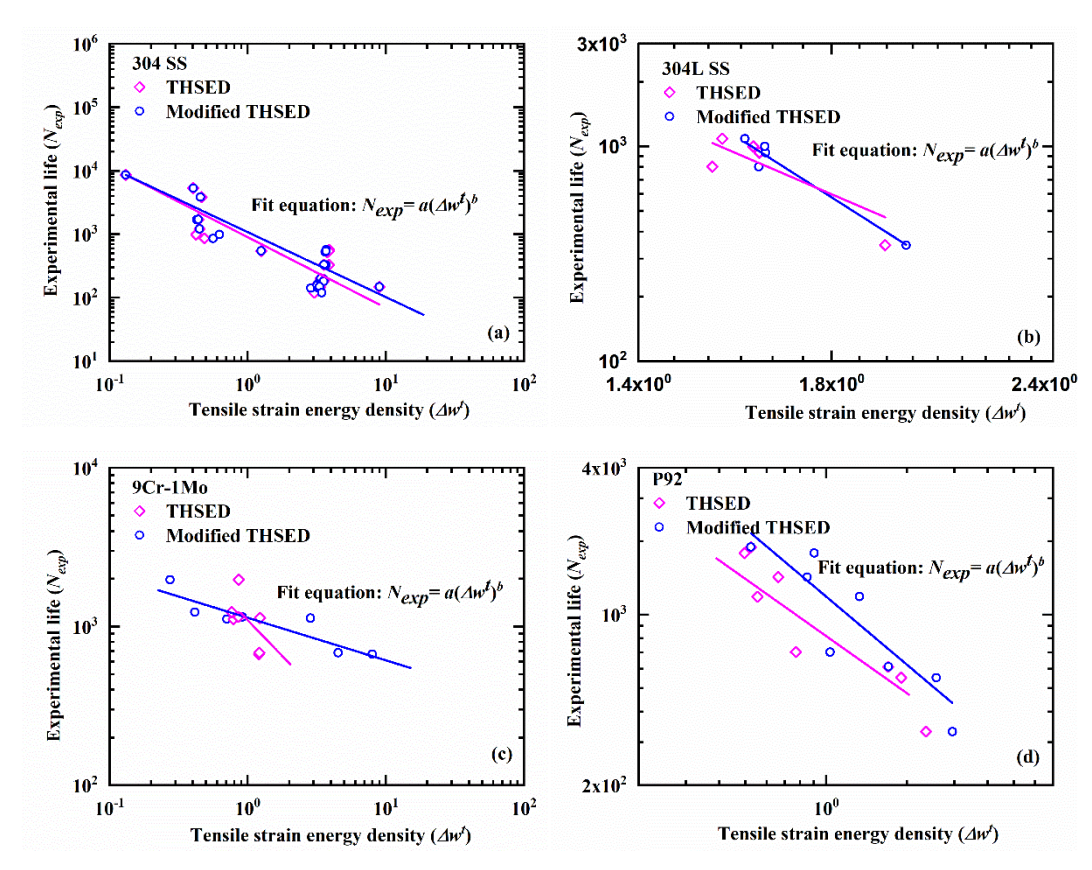


Figure 5.4. Experimental creep-fatigue life (N_{exp}) vs. Δw^t

Table 5.3: Creep-fatigue data of the materials

Material	Temp (°C)	έ (%/s)	E (GPa)	TH (min)	CH (min)	H-CFI (MPa- min)	N _{exp}	n'
304 SS [215]	650	0.4	150	0.1/10/30 /60/180/ 600	5.5/30		59- 8640	0.14
304L SS	650	0.1	170	1/3/5	1/3		600- 855	0.39
9Cr- 1Mo [216]	550	0.2	175	3/10/30	3/10/ 30		670- 1973	0.12
P92 [217]	650	0.2	150	3/10		115-10/ 140-3	476- 1790 &335- 1427	0.04

Table 5.4: Parameters used for the THSED method and modified THSED method

Material	k_p	D' (wt.%)	A (wt.%)	r (mm)
304 SS [215]	3.66×10^{-12}	0.683	85.497	-10614.14
304L SS	1.66×10^{-12}	0.683	85.497	-10614.14
9Cr-1Mo [216]	6.89×10^{-9}	0.125	94.609	-13339.903
P92 [217]	4.44×10^{-10}	0.125	94.609	-13339.903

Table 5.5: Parameters used for the THSED method and modified THSED method

Material	Tomp (9C)	THSED method		Modified THSED method		
	remp. (C)	а	b	а	b	
304 SS	650	871.26	-1.129	1082.55	-1.023	
304L	650	4784.12	-3.537	12613.30	-5.242	
9Cr-1Mo	550	1085.58	-0.564	1135.65	-0.268	
P92	650	817.98	-0.778	1187.38	-0.927	

The implementation of the 'modified SEDE method' for creep-fatigue life prediction is explained below. The articles by Song et al. [28,78] may be followed for a detailed description. The method is implemented with 304 SS [215], 9Cr-1Mo steel [216], and P92 [217] materials. The test data and material parameters were obtained from the literature, as highlighted in Table 5.3, Table 5.6 and Table 5.7, respectively.

- Step-1: Mean stress σ_m is calculated from pure fatigue test data [215–217].
- Step-2: The fatigue parameters C and δ are determined from pure fatigue test data of $\Delta \varepsilon_p$ vs N_f .
- Step-3: The fatigue damage (D_f) is calculated by using Eq. (5.12). The constants $(n', \sigma_{max}, \sigma_m \text{ and } \Delta \varepsilon_p)$ are directly taken from the literature ([215–217]).
- Step-4: Creep fracture strain energy density (w_f) is determined using Eq. (15). The required constants $(w_{f,max}, w_{f,min}, \sigma_{y0}, B, \text{ and } \kappa)$ are directly taken from the literature. [78].
- Step-5: Creep strain rate (\dot{w}) is determined using Eq. (5.18). The required constants ($\dot{\varepsilon}^*$, σ^* , m^* , σ_{th} , and E) are obtained from the literature [28] using stress relaxation data.
- Step-6: After determining the w_f and \dot{w} , he creep damage (D_c) is calculated using Eq. (5.19)
- Step-7: The oxidation damage (D_0) is calculated using Eq. (5.20). The required constants $(x_i, x_w, \beta, k_p, \beta, k_p)$ and hold time are obtained from the literature [28].
- Step-8: Total damage (D_{cf}) is calculated using Eq. (5.12).
- Step-9: Creep-fatigue life (N_{pre}) of the material is predicted by using Eq. (5.13).

Table 5.6: Parameters for modified SEDE method

Material	C	δ	σ_{y0}
304 SS [215]	580.02	1.25	173
9Cr-1Mo [216]	3801.89	1.257	336
P92 [217]	2018.75	0.93	283

Table 5.7: Parameters for modified SEDE method

Material	$W_{f,max}$	$w_{f,min}$	В	κ	σ_{th}	Ė *	σ^*	m *
304 SS	82	4.5	0.15	-4.5	41	5×10^{-3}	74	11.8
9Cr-1Mo	92	6.5	0.46	-8.5	145	2×10^{-3}	90	11.5
P92	92	6.5	0.46	-8.5	75	2×10^{-3}	90	11.5

As explained above, the creep-fatigue interaction lives of the materials for U-CFI and H-CFI tests (as given in Table 5.3) have been estimated and compared in Figure 5.5 and Figure 5.6. As can be seen, for all four materials, the prediction by the modified THSED method is always better than the other two methods. For 304 SS, the prediction accuracy of the modified SEDE and THSED method lie within a scatter factor ± 3 , which is reduced to a scatter factor ± 2 for the modified THSED method. For 304L SS, mod. 9Cr-1Mo steel and P92 steel, the prediction accuracy of the modified THSED method lies within a scatter factor of ± 1.5 ; however, the other two methods yield a higher (> ± 1.5) scatter factor.

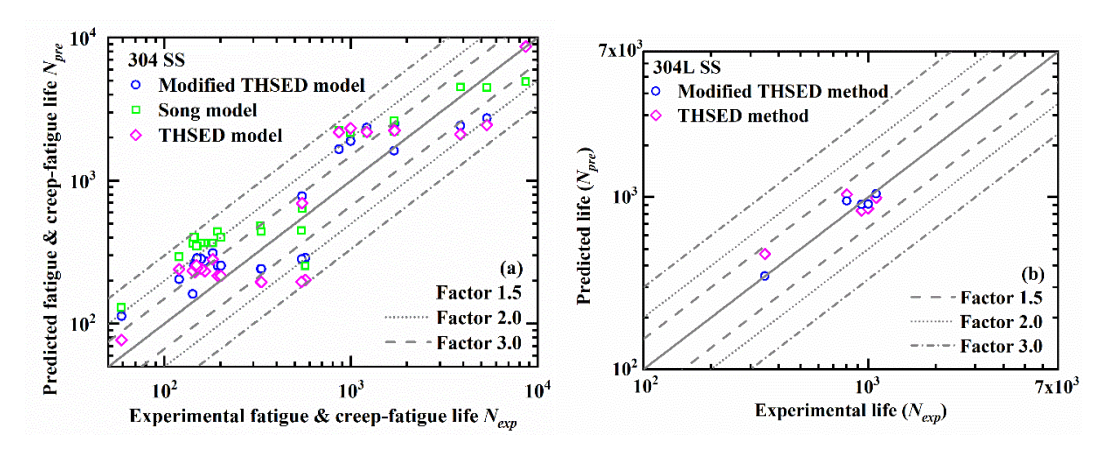


Figure 5.5. Comparison between experimental and predicted life of austenitic steels: (a) 304SS and (b) 304L SS.

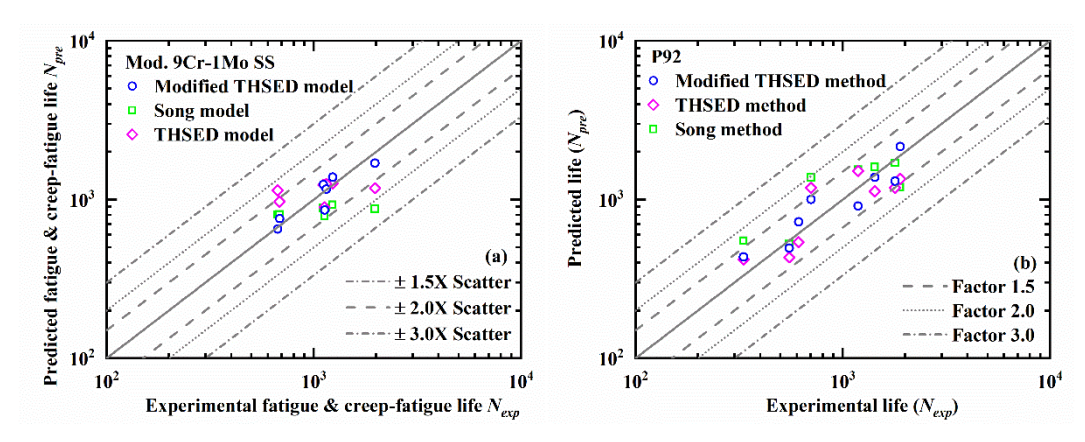


Figure 5.6. Comparison between experimental and predicted life of ferritic-martensitic steels: (a) Modified 9Cr-1Mo steel and (b) P92 steel.

5.4.3. Life prediction factor

The sensitivity of the modified THSED method to strain amplitude and hold time for creep-fatigue life prediction has been analyzed with the help of the life prediction factor (LPF), as defined by Eq. (5.29). The results are plotted in Figure 5.7. The value of LPF=1 is expected for all strain amplitudes and hold times. However, as can be seen, depending on strain amplitude and hold time, the LPF deviates from 1. For the test data considered in the current investigation, the LPF lies within ± 2.0 .

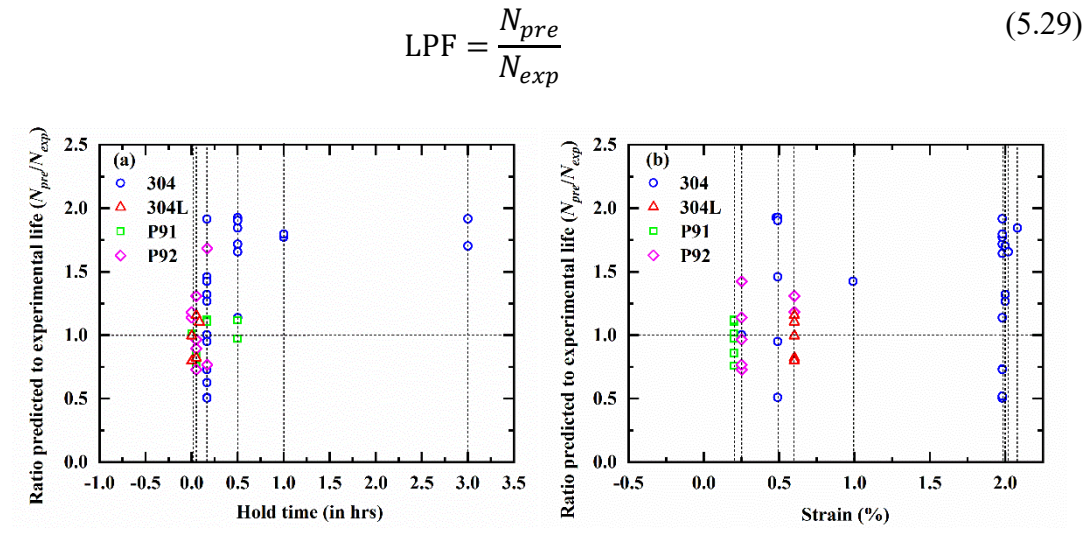


Figure 5.7. Life prediction factor for different materials plotted with (a) strain amplitude (%) and (b) hold time (hrs.).

5.5. Conclusion

A modified tensile hysteresis strain energy density (THSED) method is proposed and implemented for life prediction under uniaxial creep-fatigue interaction and hybrid creep-fatigue interaction loadings conditions. The life predicted by the modified THSED method is compared with the life predicted by the existing THSED and modified energy density exhaustion (SEDE) methods available in the literature for four different materials. The analytical expressions for the estimation of THSED for uniaxial creep-fatigue interaction and hybrid creep-fatigue interaction loadings have been derived and implemented for life prediction. The effect of oxidation damage is included in the estimate of THSED with the help of the parameter γ_d , which is defined as the ratio of fatigue damage stress to the mean stress and found to improve the life prediction by the modified THSED method. In literature, the parameter γ_d is reported to be a numerical constant obtained by the hit-and-trial method. However, the current investigation suggests that γ_d depends on the oxidation damage, temperature, strain rate of cyclic loading, and hold time.

Chapter 6: Continuum damage mechanics based unified model for creep-fatigue-oxidation

As discussed in Chapter 1: and Chapter 5: the combination of creep, fatigue, and oxidation damage causes accelerated failure in materials, and locating the damage becomes a challenging task. It can be managed by predicting the areas where the maximum stress development or strain accumulation occurs. Therefore, in this chapter, the continuum damage mechanics-based unified model is coupled with the proposed modified isotropic and kinematic hardening laws (in Chapter 3: and Chapter 4:), which are dependent on accumulated plastic, strain range memory, and transient back stress effect. The incremental damage variable is considered in the constitutive model. The damage variable consists of all three physical components, *i.e.*, creep, fatigue, and oxidation damage, and predicts the experimentally observed materials' mechanical state and behavior under creep-fatigue loading. Finally, the proposed continuum damage mechanics-based unified model is validated for the creep-fatigue interaction loading for 304L SS material.

6.1. Introduction

The phenomenological constitutive models are used in engineering applications for routine design for practical predictions of fatigue response and life assessment of materials [18,80]. The phenomenological models for creep-fatigue loading are classified as unified and non-unified models. In unified theory, the viscoplastic potential function is used that considers the plastic and creep strain together as inelastic strain, *i.e.*, the two strains exist in an inseparable form. Whereas, the non-unified theory considers the plastic (time-independent) and creep (time-dependent) strains separately [80]. Many authors have reported in the literature that creep and fatigue damage interaction causes the failure in a material [175,197–200]. Thus, the non-unified theory is considered disadvantageous as it considers the creep and plastic strain in separate forms without any interaction [32,62]. Also, implementing non-unified theory in the finite element method framework is difficult [236]. The unified theory increases simulation accuracy and can be used to predict the complex behavior of material [45]. Unified and non-unified models are based upon the two hypotheses, i.e., isotropic hardening and

kinematic hardening laws for predicting the hardening behavior of material [80]. For simulating creep-fatigue behavior, modifications are made in the kinematic hardening rule to improve the numerical prediction of viscous effect, i.e., stress relaxation. Malinin and Khadjinsky [237] assumed that the static recovery is due to high temperature in kinematic hardening. They modified the kinematic hardening law by adding a static term to predict stress relaxation behavior accurately. Yaguchi and Takahashi [238] studied the behavior of Ni-based superalloys and observed that the mean stress increases with cycling. To incorporate the increase in mean stress with cycling, they introduced a new variable in the static recovery term of the back stress. Ahmed and Hasaan [56] modified the static recovery term to incorporate the mean stress effect. They showed that the incorporation leads to only a slight improvement in the prediction of stress relaxation behavior for isothermal creep-fatigue loading. Barrett et al. [239] used hyperbolic sine law to include the strain rate effect in stress relaxation. Benaarbia et al. [54] included the thermal effect in modeling stress relaxation behavior. Wu et al. [55] observed that cyclic softening decreases with a decrease in strain amplitude and a similar effect was observed on mean stress relaxation. Thus, they added a constant parameter in the static recovery term of kinematic hardening. Zhang and Xuan [57] observed that stress relaxation shows cyclic softening behavior and incorporated it by modifying the static recovery term of the kinematic hardening law. They replaced the constant term with a variable depending on the accumulated plastic strain. Wang et al. [62] modified the dynamic recovery part of kinematic hardening by adding a varied parameter to it and kept the static recovery term as given by Zhang and Xuan [57]. This is done to reduce the number of material parameters. The new modified variable takes care of cyclic softening and changes in loop shape with cycling. Chen et al. [240] found that the cyclic hardening during the creep-fatigue interaction test was due to kinematic hardening rather than isotropic. They also concluded that the static recovery term improves the prediction of stress relaxation, but during the stress holding periods, the inelastic strain rate evolution cannot be predicted. Thus, the creep-fatigue constitutive models to date are based on modifying the kinematic hardening rule without considering the effect of hold time and hold position on isotropic hardening.

Further, as discussed in Chapter 1: Section 1.2 it is important to consider the damage state in the constitutive model to analyze the areas of maximum material degradation. Therefore, in the current investigation, the synergistic interaction of the creep, fatigue, and oxidation damage assessment is done by considering the incremental

damage variable based on the net tensile hysteresis energy density method, which considers oxidation damage as strain-rate, time (especially the hold-time) and temperature dependent parameter, as discussed in Chapter 5: Section 5.4.1 Thus, the continuum damage mechanics-based unified constitutive model is proposed here, considering the damage as an internal state variable. The proposed constitutive model is implemented in ABAQUS as a user-defined subroutine UMAT and validated with uniaxial strain-controlled creep-fatigue test data of 304L SS material. The comparison of experimental and simulated results shows good agreement for the creep-fatigue behavior of 304L SS, *i.e.*, the variation of peak stress with cycle number, stress relaxation, and the entire stress-strain loops.

6.2. Experimental details

The strain-controlled creep-fatigue tests were conducted on 304L SS. The material's chemical composition (in % wt.) is shown in 0Section 3.2. The creep-fatigue samples were prepared with the axis of the specimen in the rolling direction. The M16 test specimens were prepared per ASTM standards, as shown in Figure. 6.1. The creep-fatigue tests were conducted at 650 °C, with a strain rate of 1×10^{-3} s⁻¹ and strain amplitude of $\pm0.6\%$ with hold times of 60, 180, and 300 sec at peak tensile strain. Similar tests were also conducted with 60 and 300 sec hold times at peak compression strain. The tests were performed on a BISS (UT-20-0100) 100 kN servo-electric fatigue testing machine.

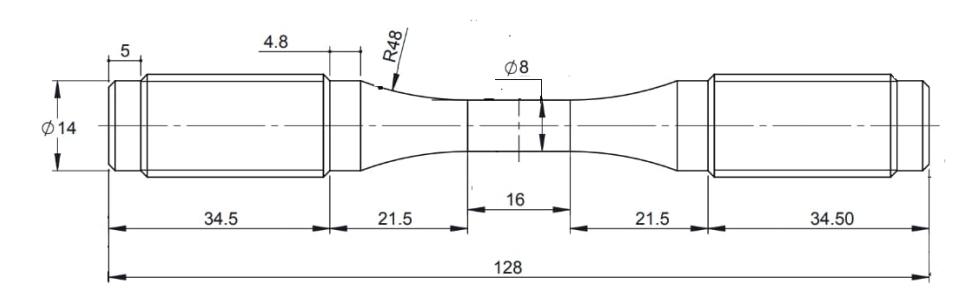


Figure. 6.1 Creep-fatigue test specimen.

6.2.1. Cyclic peak stress variation

The cyclic stress amplitude of 304L SS shows initial hardening (R_1) followed by softening (R_2) . For both peak tensile hold and peak compressive hold creep-fatigue interaction tests, as depicted in Figure. 6.2. In the creep-fatigue tests with tensile hold of 60, 180, and 300 sec, the life spent under the hardening softening phases are 4% 96%,

14%|86%, and 7%|93%, respectively. Similarly, in the creep-fatigue tests with compression holds of 60 and 300 sec, the life spent under the hardening|softening phases are 6%|94% and 5%|95%, respectively. Thus, the softening phase dominates in both compression and tensile hold creep-fatigue tests.

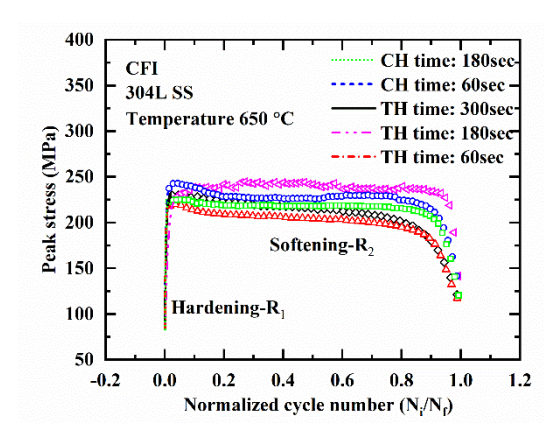


Figure. 6.2 Peak stress variation with the number of cycles normalized by failure cycles

6.2.2. Yield surface expansion and translation with cycling, hold time and hold position

The yield surface expansion/contraction in constitutive modeling is taken into account by considering peak effective stress (σ^0), *i.e.*, half of the linear stress of the loading branch of different stress-strain loops. It is observed that the peak effective stress (σ^0) exhibits an initial hardening region (R_1) followed by a softening region (R_2) for both tensile hold and compression hold, *i.e.*, behavior remains the same with hold position (tensile or compression hold) under creep-fatigue tests, as shown in Figure. 6.3(a). The loop shape variation with cycling is included in constitutive modeling by considering a non-dimensional parameter (φ_{mod}), [159] which is defined as the ratio of 'maximum back stress at any cycle' to the 'maximum back stress at first cycle', and is shown in Figure. 6.3(b). It (φ_{mod}) shows initial hardening followed by almost saturation.

For the pure fatigue experiments in Chapter 4: Section 4.2.2, it is observed that the variation of the $\varphi_{\rm mod}$ with accumulated plastic strain (p) follows the variation of peak stress with accumulated plastic strain (p) for materials 304L SS and 321 SS. However, under creep-fatigue loading of material 304L SS, the variation of the $\varphi_{\rm mod}$ with p shows initial hardening and saturation, whereas peak stress with accumulated plastic strain shows initial hardening followed by softening region.

From Figure. 6.3 (a) and (b), the value of peak effective stress and φ_{mod} is found to increase with an increase in hold time and achieves the maximum value with almost the same amount of accumulation of plastic strain for different hold times. For the softening region (R_2) the peak effective stress is observed to decrease with hold time and achieves the minimum value at failure. However, the amount of accumulated plastic strain remains almost the same in the case of peak tensile hold and peak compressive hold, irrespective of hold time.

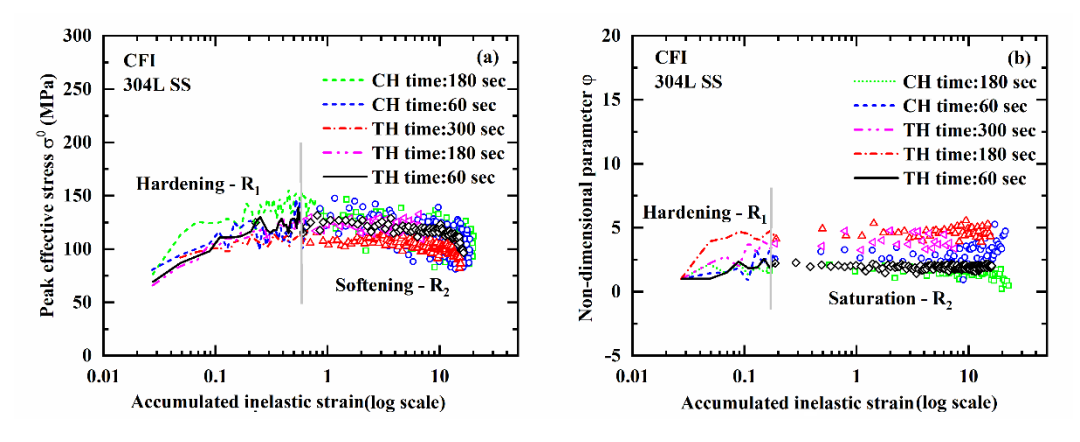


Figure. 6.3 (a) Peak effective stress variation with accumulated inelastic strain (p) (b) Variation of φ_{mod} with accumulated inelastic strain (p) at different hold times and hold position.

6.2.3. Stress relaxation with cycling

The stress relaxation is plotted with cycle number and is shown in Figure. 6.4 it can be observed that stress relaxation increases with an increase in cycling for both peak tensile hold and peak compression hold time for the region (R_1) and attains the maximum value, and then it remains almost constant with cycling for both peak tensile and peak compression hold positions. It can be concluded that the stress relaxation curves show almost similar behavior to that of the non-dimensional parameter (φ_{mod}) with accumulated plastic, *i.e.*, initial increase almost like hardening (R_1) followed by the saturation region (R_2) .

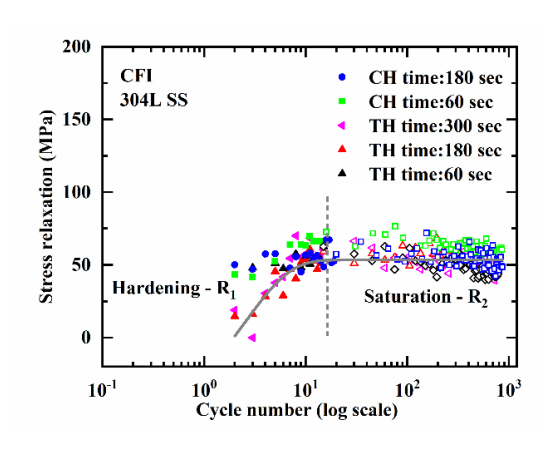


Figure. 6.4 Stress relaxation with cycle number

6.2.4. Damage accumulation and creep-fatigue life

Figure 6.5 shows that under compression hold the creep-fatigue life of the material is more than tensile hold, similar to as reported for austenitic steel in literature [234,241]. Also, it is observed that as the peak tensile hold time increases from 60 to 300 sec, the creep-fatigue life of the material increases by 85 cycles. Similarly, under peak compression hold, an increase in creep-fatigue life of 90 cycles is observed with an increase in hold time from 60 to 180 sec.

In literature, an increase in the creep-fatigue life of material with hold time is reported for austenitic 316LN SS [242–244]. It is attributed to dislocation annihilation that occurs as the longer hold times at high temperatures cause the edge dislocations to climb up and screw dislocations to cross-slip. Another factor that contributes to the increase in creep-fatigue life with hold time is thermal aging, i.e., with increased hold time, the recovery in a material that causes the development of a grain structure refinement, i.e., grains of a similar size are formed [243,245,246].

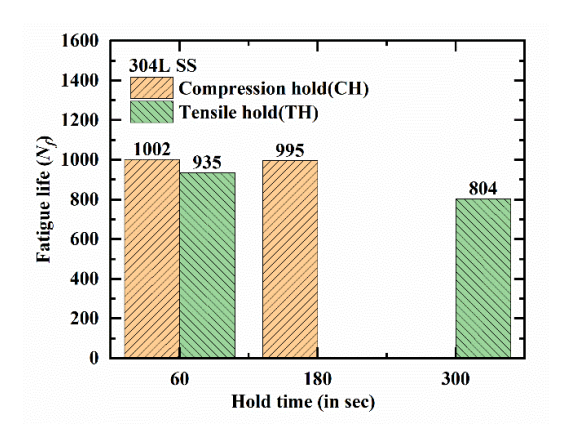


Figure 6.5 Creep-fatigue life with hold time

The increment in damage in N^{th} cycle is calculated as given by Eq. (6.1). A similar estimation of damage is used by other researchers [99–101,109,110] for pure fatigue and creep-fatigue condition considering the inelastic strain energy density. However, in Eq. (6.1), Δw^t is the modified total tensile hysteresis strain energy density, which is calculated as the summation of plastic, creep, and elastic strain energy density components, as discussed in Chapter 5: Section 5.2.1.

It should be noted that Δw^t in Eq. (6.1) takes into account the material parameter γ^{mod} , which is proportional to oxidation damage, as shown by Eq. (5.28) in Chapter 5: Section 5.4.1. The parameter w^{total} in Eq. (6.1) represents the accumulated tensile hysteresis strain energy density at failure.

$$\Delta d_N = \frac{\Delta w^t}{\sum \Delta w^t} = \frac{\Delta w^t}{w^{total}} \tag{6.1}$$

It is important to note that the value of w^{total} for a material varies with temperature and loading conditions, *i.e.*, different values of w^{total} are obtained when the material is subjected to different tensile hold times and compression hold times. The variation can be incorporated into the constitutive model by considering the maximum plastic strain range memory effect. For this purpose, the w^{total} is plotted with maximum plastic strain range (%), as shown in Figure 6.6, which shows a power-law relationship and is given by Eq. (6.2). Therefore, instead of using a fixed value of w^{total} , Eq. (6.2) can be used in the constitutive model, along with the plastic strain memorization equations proposed by Chaboche et al. [116]. However, to keep the damage evolution model simple, a constant value of w^{total} has been assumed in this study. Accordingly, the model has been validated for tensile, and compression hold time of 60 seconds, and the implementation of the co-relation remains the scope of future work.

$$w^{total} = a(q)^b (6.2)$$

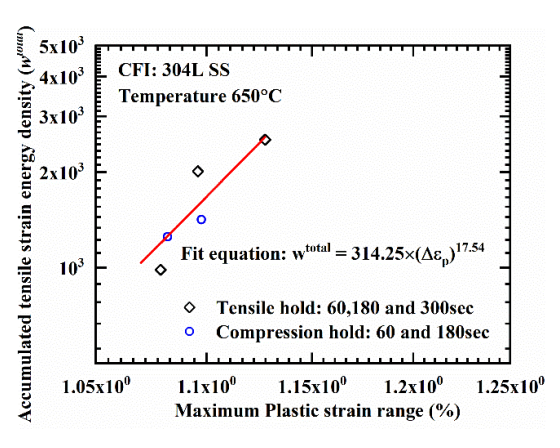


Figure 6.6 Accumulated tensile strain energy density (w^{total}) with maximum plastic strain range (%).

6.3. Damage coupled unified constitutive model

6.3.1. Main equations

The proposed modified damage-coupled unified model is based on the basic framework of the Chaboche unified viscoplastic [32] model. The total strain is decomposed in elastic and plastic strain, as shown by Eq.

$$\boldsymbol{\varepsilon} = \boldsymbol{\varepsilon}_e + \boldsymbol{\varepsilon}_{in} \tag{6.3}$$

The trial stress is calculated as given by Eq. (6.4).

$$\sigma_{N+1}^{tr} = \sigma_N + (1 - D)C: \varepsilon_e$$
(6.4)

The inelastic strain rate is given by Eq. (6.5) (6.4)

$$\dot{p} = \frac{\lambda}{1 - D} \langle \frac{f}{K} \rangle^m \tag{6.5}$$

Where K and m are rate-dependent viscous material parameters. f is the yield criteria and is given by Eq. (6.6).

$$f = J_2(\frac{\sigma'}{1 - D} - x) - r(p) - \sigma_{y0}$$
 (6.6)

Here (x) represents the yield surface translation and $(r(p) + \sigma_{y0})$ represents the yield surface expansion, *i.e.*, peak effective stress (σ^0) . The equations for yield surface expansion and translation are modified (as discussed in Section 6.3.2 to 6.3.3) and are used.

6.3.2. Modeling yield surface expansion and translation with cycling

The evolution of peak effective stress (σ^0) and non-dimensional parameter ($\phi_{\rm mod}$) with cycling, as shown in Figure. 6.3(a) and (b), respectively, are modeled as additive decomposition of two terms, as given by Eq. (6.7) and Eq. (6.8). The 1st term takes into account the cyclic hardening behavior, and the 2nd term takes into account of the softening/saturation behavior.

$$\sigma^{0} = [\sigma_{y0} + Q(1 - exp(-bp))] + [\sigma_{1} + Q_{1}(1 - exp(-b_{1}p))]$$

$$1^{\text{st}} \text{ term}$$

$$2^{\text{nd}} \text{ term}$$
(6.7)

$$\varphi_{\text{mod}} = [a_2 + a_3(1 - exp(-a_4p))] + [a_5 + a_6p]$$

$$1^{\text{st}} \text{ term} \qquad 2^{\text{nd}} \text{ term}$$
(6.8)

(Note: the detailed formulation of Eq. (6.7) and Eq. (6.8) can be found under 0Section 3.3.1 and 3.3.2, respectively).

6.3.3. Modification in kinematic hardening rule due to variation in stress relaxation behavior with cycling

In literature articles [57,62], the variation of decaying stress relaxation behavior with cycling is modeled by modifying the non-linear kinematic hardening rule shown by Eq. (6.9) to Eq. (6.10), *i.e.*, by adding the static recovery term. It should be noted that the static recovery term (written in the box in Eq. (6.10)) contains a variable τ with accumulated plastic strain, and material parameter r is proposed for 9-12 Cr- 1Mo steel by Wang et al. in article [62] which shows continuous softening feature in stress relaxation and is given by Eq. (6.11).

The stress relaxation of 304L SS shows an initial increase followed by saturation for different hold times, as shown in Figure. 6.4 in Section 6.2.3. Similar to Eq. (3.11) proposed in Chapter 3: Section 3.4.2 to model cyclic hardening/softening behavior, the stress relaxation behavior is modeled by Eq. (6.15), where b_1 to b_5 are material parameters.

Further, fitting Eq. (6.11) and Eq. (6.12) to the stress relaxation vs. accumulated plastic strain data, it is observed that Eq. (6.12) fits better, as shown by Figure 6.7.

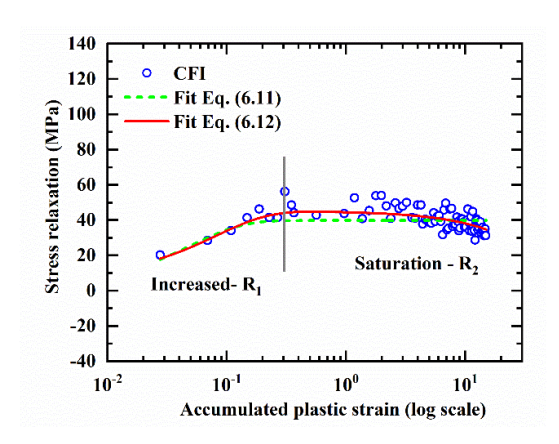


Figure 6.7 Stress relaxation vs. accumulated inelastic strain

In the present approach, the change in loop shape is modeled by considering the non-dimensional parameter φ_{mod} . Thus, the overall equation for backstress evolution is given by Eq. (6.13). In Eq. (6.13), the C and γ are simple kinematic hardening parameters, r and $\tau(p)$ controls the amount of static recovery and J(x) represents the second invariant of back stress.

$$\dot{x} = \frac{2}{3} C \dot{\varepsilon}_p - \gamma x \, \dot{p} \tag{6.9}$$

$$\dot{\mathbf{x}} = \frac{2}{3}C\dot{\mathbf{\varepsilon}}_{p} - \gamma \mathbf{x}\,\dot{p} - \boxed{\tau(p)[J(\mathbf{x})]^{r-1}\mathbf{x}}$$
(6.10)

$$\tau(p) = \tau_0[\emptyset + (1 - \emptyset) \exp(-\omega p)] \tag{6.11}$$

$$\tau(p) = b_1 + b_2(1 - \exp(-b_3 p)) + b_4 + b_5 p \tag{6.12}$$

$$\dot{\mathbf{x}} = \varphi_{mod} \frac{2}{3} C \dot{\boldsymbol{\varepsilon}}_{p} - \gamma \boldsymbol{x} \, \dot{p} - \boxed{\tau(p) [J(\boldsymbol{x})]^{r-1} \boldsymbol{x}}$$
(6.13)

$$J(\mathbf{x}) = \left(\frac{3}{2}(\mathbf{x}:\mathbf{x})\right)^{1/2} \tag{6.14}$$

6.3.4. Damage evolution

The incremental damage per cycle (Δd_N) is calculated as shown by Eq. (6.1). Thus, the total damage accumulation (D) after N^{th} cycle is calculated as given by Eq. (6.15).

$$D_N = \Delta d_N + D_{N-1} \tag{6.15}$$

It is to be noted that the linear damage accumulation models are inadequate for accurate damage prediction under cyclic loading [97,247–249], as damage accumulation does not occur evenly in each cycle. Initially, the material would undergo deformation without damage. However, accumulation of deformation with cycling leads to damage initiation and propagation. Hence, damage under cyclic loading initially

increases slowly, followed by exponential growth [65,97,249,250]. Therefore, in the current investigation, the non-linear damage accumulation model proposed by Aeran et al. [250], as described by Eq. (6.16) and Eq. (6.17), is used with the modification highlighted in Eq. (6.18) and Eq. (6.19). The model parameter S in Eq. (6.16) is obtained from the damage (D) versus fatigue life (N_f) curve, and the exponent -1.25 provides the best fit for C45 steel in the referred article [250]. The Eq. (6.16) is modified to co-relate damage (D) with total tensile hysteresis strain energy density (w^{total}), as given by Eq. (6.18). In Eq. (6.18), the factor of 0.75 is applied for 304L stainless steel. It ensures non-linear damage propagation from 0 to 1 with cycling for various hold times, as illustrated in Figure 6.8. Accordingly, the modified damage model used in the current investigation is given by Eq. (6.19).

$$S = \frac{-1.25}{\ln(N_f)} \tag{6.16}$$

$$D = abs(1 - (1 - D_N)^s) (6.17)$$

$$S' = \frac{-0.75}{ln(w^{total})} \tag{6.18}$$

$$D = abs(1 - (1 - D_N)^{s'})$$
(6.19)

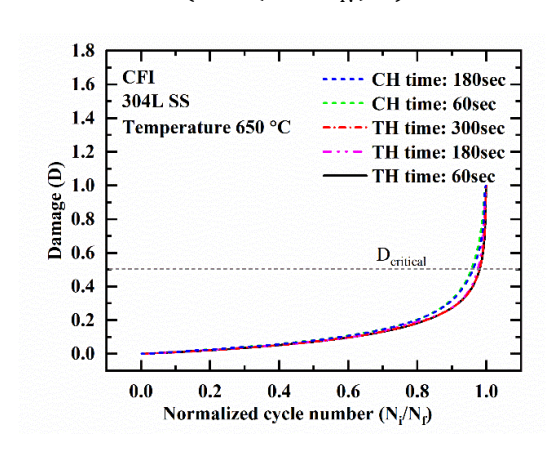


Figure 6.8 Damage evolution with normalized cycle number

6.4. Identification and calibration of material parameters

The yield stress (σ_{y0}) and elastic modulus (E) are calculated from the first cycle of the stress-strain hysteresis loops, as shown schematically in Figure 6.9. The peak effective stress (σ^0) for each cycle is estimated from the linear portion of the stress-strain hysteresis loops. The peak back stress (x_{max}) is calculated from the peak stress (σ_{max}) by subtracting the peak effective stress (σ^0) and viscous stress (σ_v) . The yield

surface expansion in the constitutive model is modeled by considering the peak effective stress (σ^0), *i.e.*, half of the linear stress of the loading branch of different stress-strain loops.

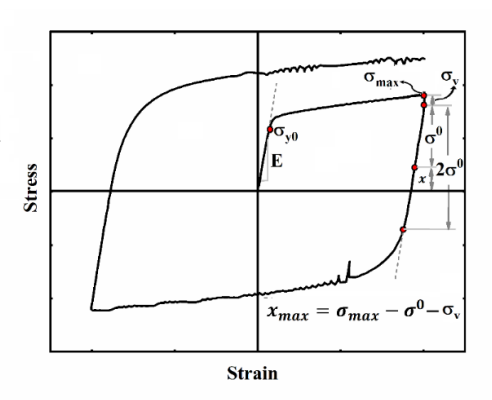


Figure 6.9. Schematic diagram showing the determination of elastic modulus (E), yield stress (σ_{y0}) , peak effective stress (σ^0) , peak back stress (x_{max}) , and viscous stress (σ_v) .

Initially, all the material parameters of the constitutive model are determined as per the model description provided through Eq. (6.1) to Eq. (6.15). Then, the parameters and calibrated as explained in the stepwise details given below:

- 1. Step-1: The yield stress (σ_{y0}) and elastic modulus (E) are calculated from the first cycle of the stress-strain hysteresis loops, as shown schematically in Figure 6.9.
- 2. Step-2: The back stress parameters C_1 and γ_1 are determined from the upper branch of the hysteresis loop (of the second cycle) obtained from the highest strain amplitude test.
- 3. Step-3: The rate-dependent viscous parameters, i.e., the *K* and *m* are calculated from the second cycle's stress relaxation with time.
- 4. Step-4: φ_{mod} is estimated as a function of p (accumulated plastic strain) for the lowest tensile hold time, *i.e.*, 60 sec, as shown in Figure. 6.3(b), and the parameters a_2 to a_9 are determined by fitting Eq. (6.8).
- 5. Step-5: The parameters b_1 to b_5 are determined from stress relaxation vs. accumulated inelastic strain data, as shown by Eq. (6.12) for 60sec tensile hold data, as shown by Figure 6.7
- 6. Step-6: σ^0 is determined from the different hysteresis loops of a test and defined as a function of p. Fitting Eq. (6.7) to the σ^0 vs. p data for lowest tensile hold

- (*i.e.*, 60 sec) test, as shown in Figure. 6.3(a), the isotropic hardening parameters are determined.
- 7. Step-7: The damage is calculated using Eq. (6.19) and is used in the constitutive equations. The input parameter w^{total} is assumed to be constant and is directly taken from the experimental result for a tensile hold of 60 sec.

Table 6.1 Material parameters required for creep-fatigue simulations for 304L SS at 650° C.

304L SS	$E = 153.359 \text{ GPa}, \nu = 0.3$
Isotropic	$\sigma_{yo} = 41.28 \text{ MPa}, Q = 105.28 \text{ MPa}, b = 6.982, \sigma_1 = 35.40 \text{ MPa}, \\ Q_1 = -3.417 \text{ MPa}, b_1 = -0.000201$
Kinematic	$C = 20400.1 \text{ MPa}, \ \gamma = 636.36$
Viscous	K = 1664.7, m = 1.48
$arphi_{mod}$	$a_2 = 1$, $a_3 = 14.919$, $a_4 = 41.736$, $a_5 = -1.688$, $a_6 = -0.00364$
$\tau(p)$	$b_1 = 3.743 \times 10^{-5}, b_2 = 37.697 \times 10^{-5}, b_3 = 12.177 \times 10^{-5}, b_4 = 3.743 \times 10^{-5}, b_5 = -0.63963 \times 10^{-5}$
Damage parameters	$w^{total} = 2531.91945 \text{ MJ/m}^3.$

6.5. Comparison of experimental and simulation results

The proposed constitutive model is implemented in ABAQUS with the help of a user material subroutine (UMAT) written in Fortran language. A three-dimensional model with 35 mm × 35 mm × 35 mm dimensions, as shown in Fig. 16 (with boundary conditions), is used for simulations. A three-dimensional 8-noded linear brick element (C3D8) is considered for simulations. According to the experimental CFI test parameters, the model was subjected to constant strain rate controlled cyclic loading with hold time at tensile or compressive peak strain. The material parameters are identified and calibrated from strain-controlled low cycle fatigue-creep test data of 304L SS at the tensile hold of 60 sec.

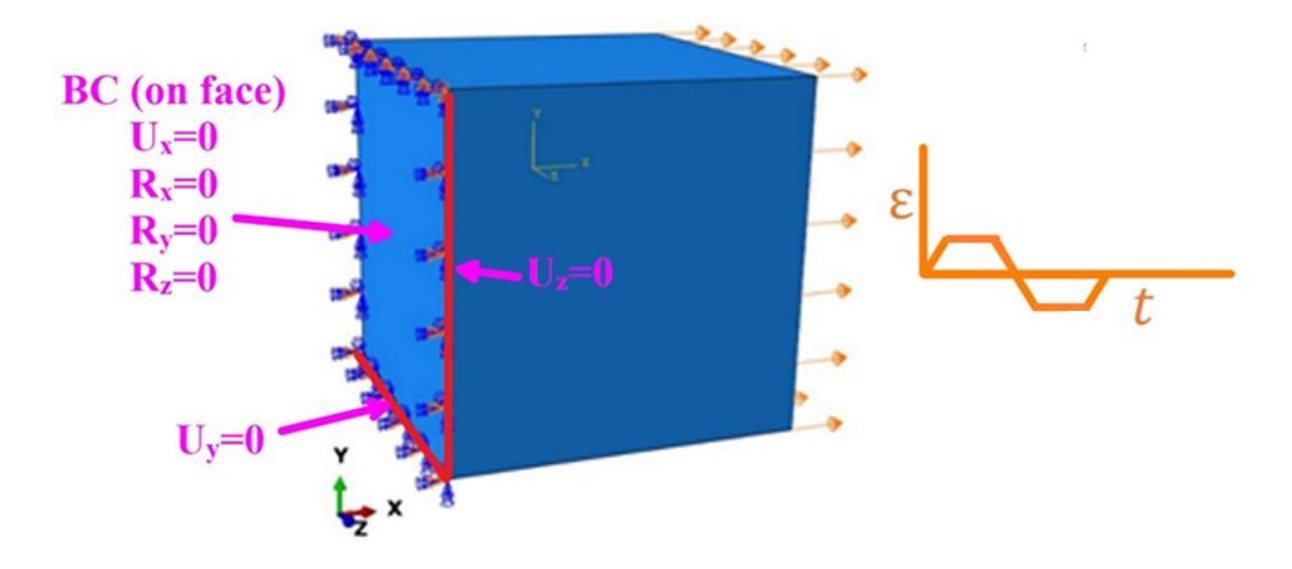


Figure 6.10 3-D model for creep-fatigue simulation. R denotes rotational degrees of freedom, and U denotes displacement.

6.5.1. Validation of model accuracy

The proposed constitutive model is validated with the material parameters obtained from the creep-fatigue interaction test conducted with a peak tensile hold time of 60 sec. The cyclic peak stress variation with the number of cycles obtained from the simulation is compared with that obtained from the creep-fatigue experiment, as shown in Figure 6.11(a). It is evident that the model incorporating damage could capture the cyclic peak stress variation with sufficient accuracy. This also validates the material parameters obtained from the test data. The analysis indicates that peak stress can be predicted with reasonable accuracy up to approximately 80% of the material's fatigue life when damage is not included in the model. However, incorporating the damage variable allows to capture the sudden peak stress drop due to damage accumulation. Like other researchers in the literature [251–253], the simulation was carried out until the damage parameter reaches a critical threshold value of 0.5. The comparison of stress relaxation behavior is demonstrated by the second and half-life cycles, as shown in Figure 6.11(b). It can be seen that stress relaxation behavior could also be captured well by the proposed model.

The evolution of the simulated and experimental hysteresis stress-strain loops for different regions, i.e., cyclic hardening (R_1) and softening (R_2) exhibited by the material under creep-fatigue interaction loading, are compared in Figure 6.12. It is observed that simulated and experimental results show good agreement.

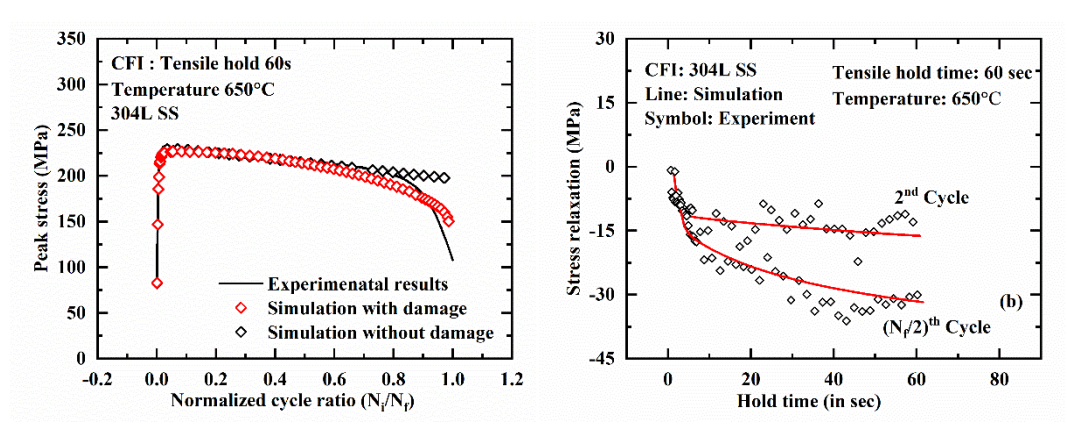


Figure 6.11. Comparison of experimental and simulated results (a) Peak stress variation with normalized cycle number (b) Stress relaxation with hold time for 2nd and half-life cycle

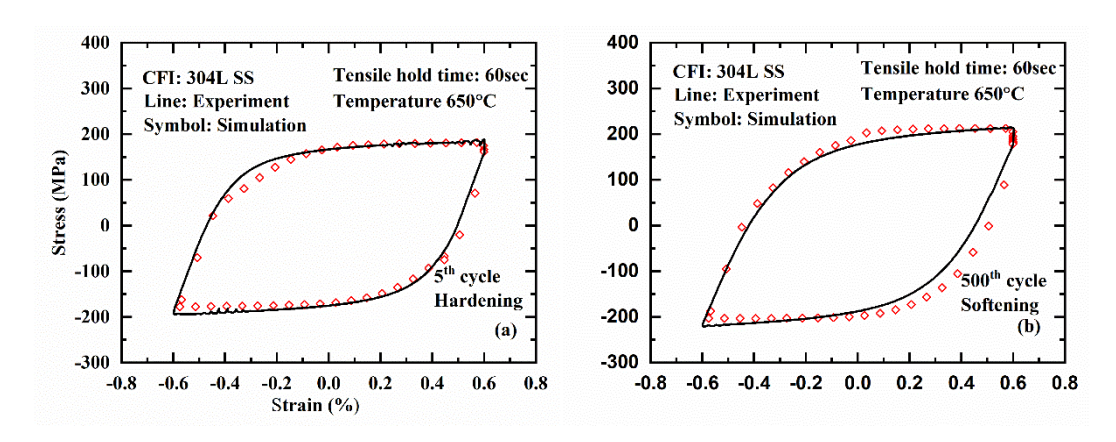


Figure 6.12. Comparison of experimental and simulated hysteresis loops of 304L SS under creep-fatigue interaction loading with peak tensile hold of 60 sec. Plotted for (a) 5th cycle and (b) 500th cycle.

6.5.2. Prediction capability of the model

The prediction capability of the proposed model can be verified by comparing the simulated results with the experimental results, especially for the test data with different hold times, which were not used for material parameter identification. Thus, this section compares the simulation results with the experimental data obtained from the creep-fatigue interaction test with a peak compressive hold time of 60 sec. From Figure 6.13(a, b) and Figure 6.14, it can be observed that the simulated and experimental results show considerable agreement for cyclic peak stress response, evolution of hysteresis stress-strain loops, and stress-relaxation behavior, respectively.

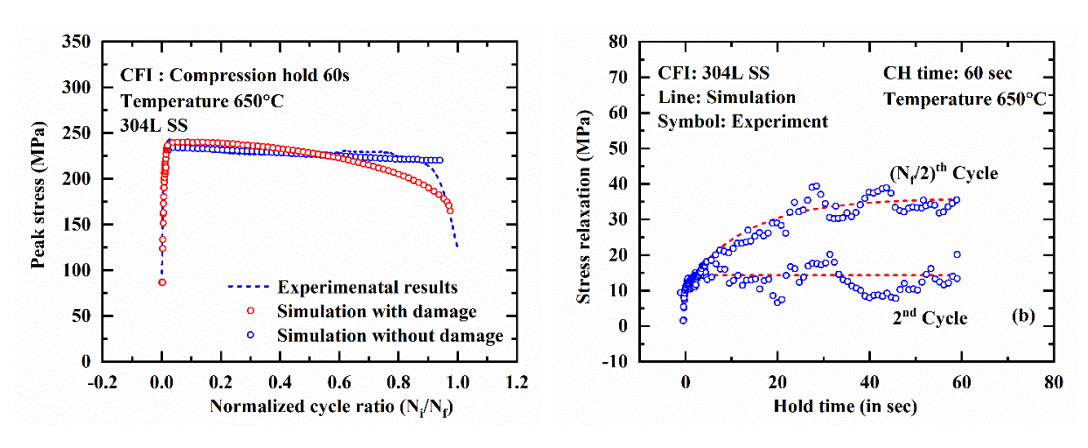


Figure 6.13. Comparison of experimental and simulated results: (a) Peak stress with cycle number (b) Stress relaxation with hold time for 2nd and half-life cycle

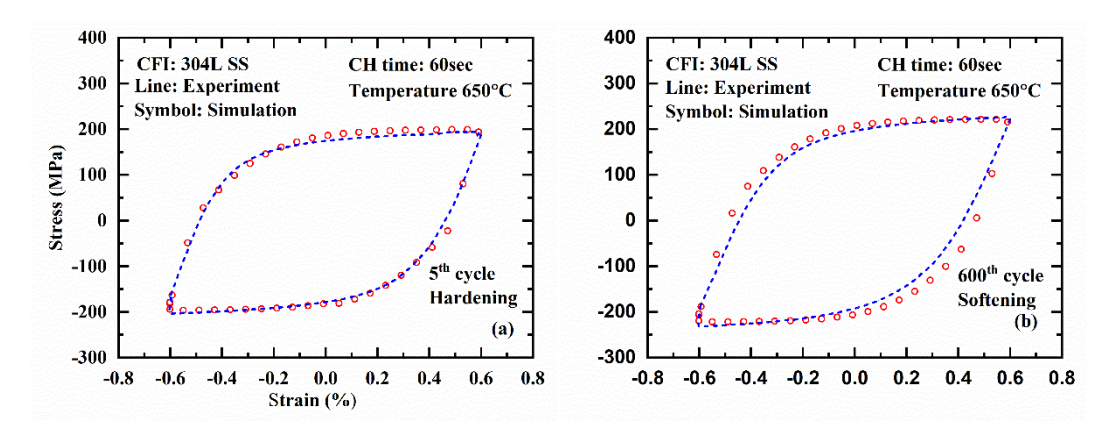


Figure 6.14. Comparison of experimental and simulated hysteresis loops for 304L SS at peak compression hold 60sec

6.6. Conclusions

Strain-controlled creep-fatigue interaction tests were performed on 304L SS at 650 °C and $\pm 0.6\%$ of strain amplitude with peak tensile hold time of 60, 180, and 300 sec and peak compressive hold time of 60 and 180 sec. The creep-fatigue interaction life is found to improve with an increase in threshold duration in tension and compression.

The influence of hold time and hold position on peak effective stress (σ^0) and back stress has been analyzed. It is observed that the cyclic peak stress and peak effective stress exhibit initial hardening followed by softening behavior. In contrast, peak back stress shows initial hardening followed by saturation behavior. Thus, unlike the low cycle fatigue test, where both peak effective stress and peak back stress follow the trend of peak stress, in the creep-fatigue test, the peak back stress does not follow the trend of peak stress.

The continuum damage mechanics-based unified constitutive model is proposed, considering the cyclic evolution of stress relaxation behavior consisting of stages, *i.e.*, initial rise followed by saturation. A new damage parameter is defined using the estimate of modified tensile hysteresis strain energy density and implemented in the proposed constitutive model to take into account the oxidation damage in creep-fatigue interaction modeling.

The model's accuracy is predicted by comparing the simulated results with the experimental results of the creep-fatigue interaction test conducted with a peak tensile hold of 60 sec. Further, the model's prediction capability is analyzed by comparing the simulated results with the experimental results obtained from the creep-fatigue interaction test conducted with a peak compressive hold of 60 sec, i.e., with the test data not used for material parameter identification and calibration. The comparison of results for stress relaxation behavior, hysteresis loop shape, and cyclic peak stress evolution over multiple cycles show considerable accuracy and predictability at various hold times.

Chapter 7: Conclusions and scope of future work

The conclusions derived from the investigations carried out to accomplish each of the thesis objectives are presented in each chapter. However, the key findings are highlighted below for the sake of readers.

7.1. Conclusions

The present study aimed to develop a robust constitutive model to predict the cyclic deformation behavior of material under strain-controlled loading that consists of either cyclic hardening, softening, saturation, and secondary hardening, or a combination of any of these. The developed constitutive model proposes modified isotropic and kinematic hardening equations. The modified isotropic hardening equation additively decomposes the various cyclic hardening and softening behaviors. The cyclic hardening and softening behaviors could be represented by exponential relationships, and the secondary hardening behavior could be represented by a linear relationship. The modified kinematic hardening equations can take into account hysteresis loop shape change with cycling and strain amplitude. The proposed model is implemented in the finite element analysis software ABAQUS with a user-defined material subroutine (UMAT) and validated with the low cycle fatigue test data of 304L SS.

Efforts have been made to apply the constitutive model to simulate the low cycle fatigue behavior of other materials, e.g., 321 SS. Strain-controlled low cycle fatigue tests were conducted on 321 SS, which is found to exhibit Type-I non-Masing behavior, contrary to Type-II non-Masing behaviors of 304L SS. Thus, the proposed constitutive laws are further modified to capture the non-Masing Type-I and Type-II behavior exhibited by different materials at different strain amplitudes. This is accomplished by taking into account the strain range memory effect in both isotropic and kinematic hardening. The proposed model with the modifications has been implemented in ABAQUS with a UMAT and validated with the low cycle fatigue test data of 304L SS and 321 SS. The model could accurately predict the hysteresis loops, cyclic peak stress variation with cycling, and the non-Masing behaviors of both materials. It may be concluded that the proposed model is very versatile and can be applied to different structural steels to simulate their low-cycle fatigue behavior.

The current study further aimed to apply the developed constitutive model for simulating the creep-fatigue interaction behavior of materials and life prediction. Thus, the hardening laws developed for modeling the low cycle fatigue behavior are modified to take into account the time-dependent effect to simulate the creep-fatigue interaction behavior. This is done by modifying the kinematic hardening equation to take into account the stress relaxation behavior during strain hold. The model also considers damage in an incremental form based on the proposed modified tensile hysteresis strain energy density method, thus taking into account the oxidation damage. The continuum damage mechanics-based unified constitutive model developed for this purpose has been validated by uniaxial creep-fatigue interaction test data of 304L SS for different tension and compression hold times.

For the life prediction, tensile strain energy density based methods have been investigated. A modified tensile hysteresis strain energy density (modified THSED) method is proposed to predict the creep-fatigue interaction (CFI) life of materials by taking into account oxidation damage. The oxidation kinetics approach is considered for estimating the oxidation damage. The oxidation damage is taken into account with the help of a model parameter γ_d , which is found by hit and trial in the literature, is found to be dependent on the oxidation damage, strain rate, and hold time of cyclic loading. The proposed modified THSED method could predict the life of different materials under uniaxial and hybrid creep-fatigue loading conditions within a scatter factor of ± 2 .

7.2. Future scope

- The proposed model is validated for uniaxial strain-controlled low cycle fatigue behavior of materials, which exhibit Type-I and Type-II non-Masing behavior. However, the model's applicability should be validated for complex loading, such as multiaxial-loading conditions.
- 2. The strain rate and temperature variation are important factors that affect the cyclic hardening/softening and Type-I/Type-II Masing behaviors of material, which are not considered in the study. Thus, the effect of strain-rate may be investigated and incorporated into the constitutive model.
- 3. The modified THSED method may be verified with more materials data and also for complex loading conditions such as multi-axial loading.
- 4. The strain rate effect may be studied experimentally and incorporated into the

- proposed unified creep-fatigue damage mechanics-based model. Moreover, due to limited time, the proposed model could not be verified for creep-fatigue interaction tests at different strain amplitudes. Such a study may be conducted.
- 5. The accumulated tensile strain energy density for a material varies with temperature, strain-rate and, complex loading condition such as tensile hold, compression hold creep-fatigue loading. Thus, the variation in accumulated tensile hysterisis strain energy density must be studied and included in the continuum damage mechanics-based unified constitutive model.

Chapter 8: Publications

Journals

- **1.** N. Mehani, S.C. Roy, Modified isotropic and kinematic hardening equations for 304L SS under low cycle fatigue, Comput. Mater. Sci. 240 (2024) 112999. https://doi.org/10.1016/j.commatsci.2024.112999.
- **2.** N. Mehani, S.C. Roy, Type-I and Type-II non-Masing behaviors of materials under low cycle fatigue: constitutive modeling and simulation, submitted to Engineering Fracture Mechanics
- **3.** N. Mehani, S.C. Roy, Quantification of the creep, fatigue, and oxidation damage and life prediction, submitted to International Journal of Damage Mechanics.
- **4.** N. Mehani, S.C. Roy, Article on "Continuum damage mechanics based unified model for creep-fatigue-oxidation". (To be submitted soon).

Presentations in Conferences

- **1.** N. Mehani, S.C. Roy, "Constitutive modeling of low cycle fatigue behavior of 321 austenitic stainless steel" in 3rd International Conference on Structural Integrity, ICONS-2023, August 23rd-25th, 2023.
- **2.** N. Mehani, S.C. Roy, "Constitutive modeling of materials' cyclic hardening and softening behavior for steel under low cycle fatigue" in the 16th International Conference on Creep and Fracture of Engineering Materials and Structures, Creep-2024, held during 28th July 2nd August 2024.

Chapter 9: References

- [1] International Energy Agency IEA. Electricity 2024 Analysis and forecast to 2026. Int Energy Agency 2023:1–170.
- [2] Bhattacharjee D, Chakrabarti S. Future Landscape of Structural Materials in India. 2022. https://doi.org/10.1007/978-981-16-8523-1.
- [3] Patel SJ, De Barbadillo JJ, Baker BA, Gollihue RD. Nickel base superalloys for next generation coal fired AUSC power plants. Procedia Eng 2013;55:246–52. https://doi.org/10.1016/j.proeng.2013.03.250.
- [4] Chen S, Xie A, Lv X, Chen S, Yan C, Jiang H, et al. Tailoring Microstructure of Austenitic Stainless Steel with Improved Performance for Generation-IV Fast Reactor Application: A Review. Crystals 2023;13. https://doi.org/10.3390/cryst13020268.
- [5] Nuclear Energy Agency. Technical and Economic Aspects of Load Following with Nuclear Power Plants. 2011.
- [6] Rao KBS, Nagesha A. Significance of Creep- Fatigue Interactions in Strctural Integrity Assessment, in: Ranganath, S. Tarafder, A. Bahadur (Eds.),. Recent Trends Struct Integr Assessment, National Metall Lab Jamshedpur, India 2001:164–84.
- [7] Wang X, Zhang W, Gong J, Wahab MA. Low cycle fatigue and creep fatigue interaction behavior of 9Cr-0.5Mo-1.8W-V-Nb heat-resistant steel at high temperature. J Nucl Mater 2018;505:73–84. https://doi.org/10.1016/j.jnucmat.2018.03.055.
- [8] Xiang Chen. High temperature creep-fatigue behavior of alloy 617 and alloy 230. University of Illinois at Urbana-Champaign, 2012.
- [9] Dodgson M, Gann DM, Salter A. The impact of modelling and simulation technology on engineering problem solving. Technol Anal Strateg Manag 2007;19:471–89. https://doi.org/10.1080/09537320701403425.
- [10] Guguloth K, Swaminathan J, Ghosh RN. Creep life prediction of P91 Steel from stress relaxation tests 2014;088.

- [11] Yang Q, Zhang W, Guo Y, Liang F, Yin P, Chang L, et al. A universal constitutive model considering strain range dependence effect and transient behaviour for both cyclic softening and hardening steels. Eng Fract Mech 2023;290:109481. https://doi.org/10.1016/j.engfracmech.2023.109481.
- [12] Wang YL, Chen ZY, Liao YQ, Peng JH, Ni YZ, Xu H. A damage-coupled viscoplastic constitutive model considering tension-compression asymmetry for modeling low cycle fatigue mechanical behaviors of Inconel 617 at elevated temperature. Int J Press Vessel Pip 2023;206. https://doi.org/10.1016/j.ijpvp.2023.105040.
- [13] Song K, Wang K, Zhao L, Xu L, Han Y, Hao K. A combined elastic–plastic framework unifying the various cyclic softening/hardening behaviors for heat resistant steels: Experiment and modeling. Int J Fatigue 2022;158:106736. https://doi.org/10.1016/j.ijfatigue.2022.106736.
- [14] Mughrabi H, Christ HJ. Cyclic deformation and fatigue of selected ferritic and austenitic steels: Specific aspects. ISIJ Int 1997;37:1154–69. https://doi.org/10.2355/isijinternational.37.1154.
- [15] Jiang Y, Zhang J. Benchmark experiments and characteristic cyclic plasticity deformation. Int J Plast 2008;24:1481–515. https://doi.org/10.1016/j.ijplas.2007.10.003.
- [16] Yadav SS, Roy SC, Veerababu J, Goyal S. Type-I to Type-II non-Masing behavior of 304L SS under low cycle fatigue: Material's internal changes. Int J Fatigue 2023;175:107789. https://doi.org/10.1016/j.ijfatigue.2023.107789.
- [17] Yadav SS, Roy SC, Goyal S. A comprehensive review and analysis of Masing/non-Masing behavior of materials under fatigue. Fatigue Fract Eng Mater Struct 2023;46:759–83. https://doi.org/10.1111/ffe.13906.
- [18] Chaboche JL. Time-independent constitutive theories for cyclic plasticity. Int J Plast 1986;2:149–88. https://doi.org/10.1016/0749-6419(86)90010-0.
- [19] Zheng D, Ghonem H. Oxidation-Assisted Fatigue Crack Growth Behavior in Alloy 718-Part Ii. Applications. Fatigue Fract Eng Mater Struct 1991;14:761–8. https://doi.org/10.1111/j.1460-2695.1991.tb00704.x.
- [20] WHITE DJ. Effect of Environment and Hold Time on the High Strain Fatigue Endurance of 1/2 Percent Molybdenum Steel 1969;184:223–40.

- https://doi.org/10.1243/pime proc 1969 184 020 02.
- [21] Fournier B, Sauzay M, Caës C, Noblecourt M, Mottot M, Bougault A, et al. Creepfatigue-oxidation interactions in a 9Cr-1Mo martensitic steel. Part III: Lifetime prediction. Int J Fatigue 2008;30:1797–812. https://doi.org/10.1016/j.ijfatigue.2008.02.006.
- [22] Evangelou A, Soady KA, Lockyer S, Gao N, Reed PAS. On the mechanism of oxidation-fatigue damage at intermediate temperatures in a single crystal Ni-based superalloy. Mater Sci Eng A 2019;742:648–61. https://doi.org/10.1016/j.msea.2018.10.095.
- [23] Biglari F, Nikbin KM. Environmental creep intergranular damage and multisite crack evolution model for engineering alloys. Comput Mater Sci 2014;84:267–77. https://doi.org/10.1016/j.commatsci.2013.12.020.
- [24] Nikbin KM, Biglari F. Modelling Multiple Crack Initiation and Evolution Under Environmental Creep Conditions Using a Continuum Damage and Probabalisitc Approach. J Multiscale Model 2013;05:1350001. https://doi.org/10.1142/s1756973713500017.
- [25] Reuchet, J; Remy L. Fatigue Oxidation Interaction in a Superalloy- Application to Life Prediction in High Temperature Low Cycle Fatigue. Met Trans A n.d.; Vol. 14A:141–9.
- [26] Neu RW, Sehitoglu H. Thermomechanical fatigue, oxidation, and creep: Part i. Damage mechanisms. Metall Trans A 1989;20:1755–67. https://doi.org/10.1007/BF02663207.
- [27] Neu RW, Sehitoglu H. Thermomechanical Fatigue, Oxidation, and Creep: Part II. Life Prediction. Metall Trans 1989;20A:1769–83.
- [28] Song K, Wang D, Zhao L, Xu L, Han Y. An improved life prediction strategy at elevated temperature based on pure creep and fatigue data: Classical strain controlled and hybrid stress–strain controlled creep-fatigue test. Eng Fract Mech 2023;289:109412. https://doi.org/10.1016/j.engfracmech.2023.109412.
- [29] Islam N, Hassan T. Uniaxial Fatigue, Creep and Ratcheting Response Simulations of Alloy 617 Using Damage Coupled Viscoplastic Model 2018:1–6. https://doi.org/10.1115/pvp2018-84756.

- [30] Wang Q, Zhang N, Wang X. A new 3d creep-fatigue-elasticity damage interaction diagram based on the total tensile strain energy density model. Metals (Basel) 2020;10. https://doi.org/10.3390/met10020274.
- [31] Wang Q, Xu Z, Wang X. An efficient fatigue and creep-fatigue life prediction method by using the hysteresis energy density rate concept. Fatigue Fract Eng Mater Struct 2020;43:1529–40. https://doi.org/10.1111/ffe.13230.
- [32] Chaboche JL. Constitutive equations for cyclic plasticity and cyclic viscoplasticity. Int J Plast 1989;5:247–302. https://doi.org/10.1016/0749-6419(89)90015-6.
- [33] Hashiguchi K. Foundations of elastoplasticity: Subloading surface model. Found Elastoplast Subloading Surf Model 2017:1–796. https://doi.org/10.1007/978-3-319-48821-9.
- [34] Sidoroff F. On the formulation of plasticity and viscoplasticity with internal variables. Arch Mech Stosow 1975;27:807–19.
- [35] Lubarda VA. Elastoplasticity theory. Second. Springer Berlin Heidelberg; 2001. https://doi.org/10.1201/9781420040784.
- [36] Prager W. Recent developments in the mathematical theory of plasticity. J Appl Phys 1949;20:235–41. https://doi.org/10.1063/1.1698348.
- [37] Dafalias YF, Popov EP. A model of nonlinearly hardening materials for complex loading. Acta Mech 1975;21:173–92. https://doi.org/10.1007/BF01181053.
- [38] Besseling JF. A Theory of Plastic Flow for Anisotropic Hardening in Plastic Deformation of an Initially Isotropic Material. Amsterdam: 1953.
- [39] Brokate M, Krejčí P, Rachinskii D. Some analytical properties of the multidimensional continuous Mróz model of plasticity. Control Cybern 1998;27:199–215.
- [40] Krieg RD. A practical two surface plasticity theory. J Appl Mech Trans ASME 1975;42:641–6. https://doi.org/10.1115/1.3423656.
- [41] Yoshida F, Uemori T. A model of large-strain cyclic plasticity describing the Bauschinger effect and workhardening stagnation. Int J Plast 2002;18:661–86. https://doi.org/10.1016/S0749-6419(01)00050-X.
- [42] Ohno N, Wang JD. Kinematic hardening rules with critical state of dynamic recovery, part I: formulation and basic features for ratchetting behavior. Int J Plast

- 1993;9:375–90. https://doi.org/10.1016/0749-6419(93)90042-O.
- [43] Chen X, Jiao R, Kim KS. On the Ohno-Wang kinematic hardening rules for multiaxial ratcheting modeling of medium carbon steel. Int J Plast 2005;21:161–84. https://doi.org/10.1016/j.ijplas.2004.05.005.
- [44] Jiang Y, Sehitoglu H. Modeling of cyclic ratchetting plasticity, part ii: Comparison of model simulations with experiments. J Appl Mech Trans ASME 1996;63:726–33. https://doi.org/10.1115/1.2823356.
- [45] Krishna S, Hassan T, Ben Naceur I, Saï K, Cailletaud G. Macro versus micro-scale constitutive models in simulating proportional and nonproportional cyclic and ratcheting responses of stainless steel 304. Int J Plast 2009;25:1910–49. https://doi.org/10.1016/j.ijplas.2008.12.009.
- [46] Nouailhas D, Cailletaud G, Policella H, Marquis D, Dufailly J, Lieurade HP, et al. On the description of cyclic hardening and initial cold working. Eng Fract Mech 1985;21:887–95. https://doi.org/10.1016/0013-7944(85)90095-5.
- [47] Khutia N, Dey PP, Hassan T. An improved nonproportional cyclic plasticity model for multiaxial low-cycle fatigue and ratcheting responses of 304 stainless steel. Mech Mater 2015;91:12–25. https://doi.org/10.1016/j.mechmat.2015.05.011.
- [48] Taleb L, Cailletaud G, Saï K. Experimental and numerical analysis about the cyclic behavior of the 304L and 316L stainless steels at 350 °c. Int J Plast 2014. https://doi.org/10.1016/j.ijplas.2014.05.006.
- [49] Xu LY, Fan JS, Yang Y, Tao MX, Tang ZY. An improved elasto-plastic constitutive model for the exquisite description of stress-strain hysteresis loops with cyclic hardening and softening effects. Mech Mater 2020;150:103590. https://doi.org/10.1016/j.mechmat.2020.103590.
- [50] Zhu Y, Kang G, Kan Q, Bruhns OT, Liu Y. Thermo-mechanically coupled cyclic elasto-viscoplastic constitutive model of metals: Theory and application. Int J Plast 2016;79:111–52. https://doi.org/10.1016/j.ijplas.2015.12.005.
- [51] Zhou J, Sun Z, Kanouté P, Retraint D. Experimental analysis and constitutive modelling of cyclic behaviour of 316L steels including hardening/softening and strain range memory effect in LCF regime. Int J Plast 2018;107:54–78. https://doi.org/10.1016/j.ijplas.2018.03.013.

- [52] Zhang J, Jiang Y. Constitutive modeling of cyclic plasticity deformation of a pure polycrystalline copper. Int J Plast 2008;24:1890–915. https://doi.org/10.1016/j.ijplas.2008.02.008.
- [53] Abdel-Karim M, Khan A. Cyclic multiaxial and shear finite deformation responses of OFHC Cu. Part II: An extension to the KHL model and simulations. Int J Plast 2010;26:758–73. https://doi.org/10.1016/j.ijplas.2009.10.008.
- [54] Benaarbia A, Rae Y, Sun W. Unified viscoplasticity modelling and its application to fatigue-creep behaviour of gas turbine rotor. Int J Mech Sci 2018;136:36–49. https://doi.org/10.1016/j.ijmecsci.2017.12.008.
- [55] Wu DL, Xuan FZ, Guo SJ, Zhao P. Uniaxial mean stress relaxation of 9-12% Cr steel at high temperature: Experiments and viscoplastic constitutive modeling. Int J Plast 2016;77:156–73. https://doi.org/10.1016/j.ijplas.2015.10.001.
- [56] Ahmed R, Barrett PR, Hassan T. Unified viscoplasticity modeling for isothermal low-cycle fatigue and fatigue-creep stress-strain responses of Haynes 230. Int J Solids Struct 2016;88–89:131–45. https://doi.org/10.1016/j.ijsolstr.2016.03.012.
- [57] Zhang SL, Xuan FZ. Interaction of cyclic softening and stress relaxation of 9-12% Cr steel under strain-controlled fatigue-creep condition: Experimental and modeling. Int J Plast 2017;98:45–64. https://doi.org/10.1016/j.ijplas.2017.06.007.
- [58] Chen W, Wang F, Feng M. Study of a modified non-unified model for time-dependent behavior of metal materials. Mech Mater 2017;113:69–76. https://doi.org/10.1016/j.mechmat.2017.07.017.
- [59] Ding PS, Zheng XT. Creep-ratcheting effect and lifetime prediction of advanced 9-12% Cr ferritic steel at 600 °C. Int J Fatigue 2023;167:107245. https://doi.org/10.1016/j.ijfatigue.2022.107245.
- [60] Zhao L, Xu L, Han Y, Jing H, Gao Z. Modelling creep-fatigue behaviours using a modified combined kinematic and isotropic hardening model considering the damage accumulation. Int J Mech Sci 2019;161–162. https://doi.org/10.1016/j.ijmecsci.2019.105016.
- [61] Chaboche JL. A review of some plasticity and viscoplasticity constitutive theories. Int J Plast 2008;24:1642–93. https://doi.org/10.1016/j.ijplas.2008.03.009.
- [62] Wang X, Zhang T, Zhang W, Wahab MA, Gong J. An improved unified

- viscoplastic model for modelling low cycle fatigue and creep fatigue interaction loadings of 9–12%Cr steel. Eur J Mech A/Solids 2021;85:104123. https://doi.org/10.1016/j.euromechsol.2020.104123.
- [63] Miner, M.A. (1945), 12 A. Cumulative damage in fatigue. J Appl Mech n.d.
- [64] ASME: Boiler and Pressure Vessel Code, Part III, Division 1, Subsection NH Class 1 Components in Elevated Tempera- ture Service, ASME, New York, 2004, n.d.
- [65] Skelton RP. The energy density exhaustion method for assessing the creep-fatigue lives of specimens and components. Mater High Temp 2013;30:183–201. https://doi.org/10.3184/096034013X13757890932442.
- [66] Skelton RP, Gandy D. Creep-fatigue damage accumulation and interaction diagram based on metallographic interpretation of mechanisms. Mater High Temp 2008;25:27–54. https://doi.org/10.3184/096034007X300494.
- [67] Coffin LF, Schenectady NY. A study of the effects of cyclic thermal stresses in ductile metals. Metall Trans 1954;76:931–50.
- [68] Manson SS. Fatigue: A complex subject—Some simple approximations. Exp Mech 1965;5:193–226.
- [69] Manson, S.S.; Hirschberg MH. Fatigue behavior in strain cycling in the low- and intermediate-cycle range. An Interdiscip. Approach, Proc. 10th Sagamore Army Res. Conf. Raquette Lake, NY, n.d.
- [70] Robinson SL. Effect of Temperature Variation on the Long Time Rupture Strength of Steels. Trans ASME 1952;74:777–80.
- [71] Priest, R.H.; Ellison EG. A combined deformation map-ductility exhaustion approach to creep-fatigue analysis. Mater Sci Eng n.d.; Volume 49:7–17. https://doi.org/https://doi.org/10.1016/0025-5416(81)90128-2.
- [72] Ainsworth RA. R5 procedures for assessing structural integrity of components under creep and creep–fatigue conditions. Int Mater Rev n.d.:107–26.
- [73] Hales R. A Method of creep damage summation based on accumulated strain for the assessment of creep-fatigue endurance. Fatigue Fract Eng Mater Struct 1983; Volume 6:121–35. https://doi.org/https://doi.org/10.1111/j.1460-2695.1983.tb00329.x.

- [74] Takahashi Y. Study on creep-fatigue evaluation procedures for high-chromium steels-Part I: Test results and life prediction based on measured stress relaxation.

 Int J Press Vessel Pip 2008;85:406–22. https://doi.org/10.1016/j.ijpvp.2007.11.008.
- [75] Takahashi Y, Dogan B, Gandy D. Systematic evaluation of creep-fatigue life prediction methods for various alloys. J Press Vessel Technol Trans ASME 2013;135:1–10. https://doi.org/10.1115/1.4024436.
- [76] Wang RZ, Zhu XM, Zhang XC, Tu ST, Gong JG, Zhang CC. A generalized strain energy density exhaustion model allowing for compressive hold effect. Int J Fatigue 2017;104:61–71. https://doi.org/10.1016/j.ijfatigue.2017.07.008.
- [77] Wang RZ, Zhang XC, Tu ST, Zhu SP, Zhang CC. A modified strain energy density exhaustion model for creep-fatigue life prediction. Int J Fatigue 2016;90:12–22. https://doi.org/10.1016/j.ijfatigue.2016.03.005.
- [78] Song K, Zhao L, Xu L, Han Y, Hao K. A modified energy model including mean stress and creep threshold stress effect for creep–fatigue life prediction. Fatigue Fract Eng Mater Struct 2022;45:1299–316. https://doi.org/10.1111/ffe.13661.
- [79] Dieter G.E. Mechanical Metallurgy. second ed. New York: McGraw-Hill; 1961.
- [80] Dunne, Fionn; Petrinic N. Introduction to Computational Plasticity. vol. 39. 2006. https://doi.org/10.1088/0305-4470/39/14/B02.
- [81] Hübel H. Simplified Theory of Plastic Zones. 2017. https://doi.org/10.1007/978-3-319-29875-7.
- [82] Kang G, Kan Q. Constitutive modeling for uniaxial time-dependent ratcheting of SS304 stainless steel. Mech Mater 2007;39:488–99. https://doi.org/10.1016/j.mechmat.2006.08.004.
- [83] E. V. A practical strain-hardening function. Metallurgia n.d.;51.
- [84] M. K. Continuum model of medium with cracks. J Eng Mech Div 1980;106:1039–51. https://doi.org/https://doi.org/10.1061/JMCEA3.0002642.
- [85] Lemaitre J, Plumtree A. Application of Damage Concepts To Predict Creep-Fatigue Failures. Am Soc Mech Eng 1978;V.
- [86] Ibijola EA. On some fundamental concepts of continuum damage mechanics.

 Comput Methods Appl Mech Eng 2002;191:1505–20.

- https://doi.org/10.1016/S0045-7825(99)90187-1.
- [87] Dunne FPE, Hayhurst DR. Continuum damage based constitutive equations for copper under high temperature creep and cyclic plasticity. Proc R Soc A Math Phys Eng Sci 1992;437:545–66. https://doi.org/10.1098/rspa.1992.0079.
- [88] Bartošák M, Horváth J. A continuum damage coupled unified viscoplastic model for simulating the mechanical behaviour of a ductile cast iron under isothermal low-cycle fatigue, fatigue-creep and creep loading. Int J Plast 2024;173:103868. https://doi.org/10.1016/j.ijplas.2023.103868.
- [89] Yaguchi M, Yamamoto M, Ogata T. A viscoplastic constitutive model for nickel-base superalloy, part 2: Modeling under anisothermal conditions. Int J Plast 2002;18:1111–31. https://doi.org/10.1016/S0749-6419(01)00030-4.
- [90] Miner MA. Cumulative Damage in Fatigue. J Appl Mech Trans ASME 1945;12:A159–64. https://doi.org/10.1115/1.4009458.
- [91] Coffin LF. .Concept of frequency separation in life prediction for time-dependent fatigue. No. . General Electric Co., Schenectady, NY (USA), 1976. ASME-MPC creep/fatigue Interact. MPC-3, NY(USA): 1976.
- [92] Halford GR, Saltsman JF. Strainrange Partitioning A Total Strain Range Version. NASA Tech. Memo., 1983.
- [93] Priest RH, Ellison EG. A combined deformation map-ductility exhaustion approach to creep-fatigue analysis. Mater Sci Eng 1981;49:7–17. https://doi.org/10.1016/0025-5416(81)90128-2.
- [94] Simo JC, Ju JW. Strain- and stress-based continuum damage models-I. Formulation. Int J Solids Struct 1987;23:821–40. https://doi.org/10.1016/0020-7683(87)90083-7.
- [95] Murakami S. Continuum Damage Mechanics-A Continuum Mechanics Approach to the Analysis of Damage and Fracture. vol. 185. 1st ed. Springer Science and Buisnesss Media; 2012. https://doi.org/10.1007/978-94-007-2666-6.
- [96] Kachanov LM. On rupture time under condition of creep. 1958.
- [97] Fatemi A, Yang L. Cumulative fatigue damage and life prediction theories. Int J Fatigue 1998;20:9–34.
- [98] Lemaitre J, Dufailly J. Damage measurements. Eng Fract Mech 1987;28:643–61.

- https://doi.org/10.1016/0013-7944(87)90059-2.
- [99] Youn GG, Nam HS, Kim YJ, Kim JW. Numerical prediction of thermal aging and cyclic loading effects on fracture toughness of cast stainless steel CF8A: Experimental and numerical study. Int J Mech Sci 2019;163. https://doi.org/10.1016/j.ijmecsci.2019.105120.
- [100] Hwang JH, Kim YJ, Kim JW. Energy-based damage model incorporating failure cycle and load ratio effects for very low cycle fatigue crack growth simulation. Int J Mech Sci 2022;221:107223. https://doi.org/10.1016/j.ijmecsci.2022.107223.
- [101] Li K, Wang R, Yuan G, Zhu S, Zhang X, Tu S, et al. A crystal plasticity-based approach for creep-fatigue life prediction and damage evaluation in a nickel-based superalloy. Int J Fatigue 2021;143:106031. https://doi.org/10.1016/j.ijfatigue.2020.106031.
- [102] Chaboche JL, Gallerneau F. An overview of the damage approach of durability modelling at elevated temperature. Fatigue Fract Eng Mater Struct 2001;24:405–18. https://doi.org/10.1046/j.1460-2695.2001.00415.x.
- [103] Stewart CM. A hybrid constitutive model for creep, fatigue, and creep-fatigue damage. College of Engineering and Computer Science, University of Central Florida, Orlando, Florida, 2009.
- [104] Rabotnov YN, Leckie FA, Prager W. Creep Problems in Structural Members. North Holland, Amsterdam: 1969. https://doi.org/10.1115/1.3408479.
- [105] Yu. NR. Creep rupture. In: Hetenyi M., Vincenti M. (eds). Springer, Berlin; 1968.
- [106] Lemaitre J, Chaboche JL. Mechanics of solid materials. vol. 19. United Kingdom: Cambridge University Press; 1990.
- [107] Liu Y, Mukarami S. Damage Localization of Concventional Creep Damage Models and Proposition of a New Modelfor Creep Damage Analysis. JSME Int J Ser 1998;41:57–65. https://doi.org/https://doi.org/10.1299/jsmea.41.57.
- [108] Pandey VB, Singh I V., Mishra BK. A Strain-based continuum damage model for low cycle fatigue under different strain ratios. Eng Fract Mech 2021;242:107479. https://doi.org/10.1016/j.engfracmech.2020.107479.
- [109] Fan ZC, Chen XD, Chen L, Jiang JL. A CDM-based study of fatigue-creep interaction behavior. Int J Press Vessel Pip 2009;86:628–32.

- https://doi.org/10.1016/j.ijpvp.2009.04.003.
- [110] Zhang G, Zhao Y, Xue F, Mei J, Wang Z, Zhou C, et al. Creep-fatigue interaction damage model and its application in modified 9Cr-1Mo steel. Nucl. Eng. Des., 2011. https://doi.org/10.1016/j.nucengdes.2011.08.076.
- [111] Dassault Systèmes Simulia. Abaqus user subroutines. Abaqus 612 2013;53:1689–99. https://doi.org/10.1017/CBO9781107415324.004.
- [112] Wilkins ML. Computation of elastic--plastic flow. Methods Comput Phys 1964;3.
- [113] Zhang J, Zhou Z, Zhang F, Tan Y, Yi R. Molding process and properties of continuous carbon fiber three-dimensional printing. Adv Mech Eng 2019;11. https://doi.org/10.1177/1687814019835698.
- [114] Armstrong P. J., Frederick CO. A mathematical representation of the multiaxial Bauschinger effect. vol. RD/B/N731. Berkeley, U.K: 2007.
- [115] McDowell DL. A two surface model for transient nonproportional cyclic plasticity: Part 2 comparison of theory with experiments. J Appl Mech Trans ASME 1985;52:303–8. https://doi.org/10.1115/1.3169045.
- [116] Chaboche JL, Van KD, Cordier G. Modelization of the Strain Memory Effect on the Cyclic Hardening of 316 Stainless Steel. Trans Int Conf Struct Mech React Technol 1979;L.
- [117] Nouailhas D, Chaboche JL, Savalle S, Cailletaud G. On the constitutive equations for cyclic plasticity under nonproportional loading. Int J Plast 1985;1:317–30. https://doi.org/10.1016/0749-6419(85)90018-X.
- [118] Taleb L, Cailletaud G, Saï K. Experimental and numerical analysis about the cyclic behavior of the 304L and 316L stainless steels at 350 °c. Int J Plast 2014;61:32–48. https://doi.org/10.1016/j.ijplas.2014.05.006.
- [119] Tanaka E. A nonproportionality parameter and a cyclic viscoplastic constitutive model taking into account amplitude dependences and memory effects of isotropic hardening. Eur J Mech A Solids 1994:155–73.
- [120] Jiang Y, Kurath P. Nonproportional cyclic deformation: Critical experiments and analytical modeling. Int J Plast 1997;13:743–63. https://doi.org/10.1016/S0749-6419(97)00030-2.
- [121] Jiang Y, Kurath P. An investigation of cyclic transient behavior and implications

- on fatigue life estimates. J Eng Mater Technol Trans ASME 1997;119:161–70. https://doi.org/10.1115/1.2805989.
- [122] Kang GZ, Li Y, Gao Q, Kan QH, Zhang J. Uniaxial ratchetting in steels with different cyclic softening/hardening behaviours. Fatigue Fract Eng Mater Struct 2006;29:93–103. https://doi.org/10.1111/j.1460-2695.2006.00964.x.
- [123] Xu L, Nie X, Fan J, Tao M, Ding R. Cyclic hardening and softening behavior of the low yield point steel BLY160: Experimental response and constitutive modeling. Int J Plast 2016;78:44–63. https://doi.org/10.1016/j.ijplas.2015.10.009.
- [124] Zhu Y, Kang G, Yu C. A finite cyclic elasto-plastic constitutive model to improve the description of cyclic stress-strain hysteresis loops. Int J Plast 2017;95:191–215. https://doi.org/10.1016/j.ijplas.2017.04.009.
- [125] Xing R, Yu D, Shi S, Chen X. Cyclic deformation of 316L stainless steel and constitutive modeling under non-proportional variable loading path. Int J Plast 2019;120:127–46. https://doi.org/10.1016/j.ijplas.2019.04.016.
- [126] Yadav SS, Roy SC, Veerababu J, Goyal S. Quantitative Assessment and Analysis of Non-Masing Behavior of Materials under Fatigue. J Mater Eng Perform 2021;30:2102–12. https://doi.org/10.1007/s11665-021-05494-w.
- [127] Xu L, Nie X, Fan J, Tao M, Ding R. Cyclic hardening and softening behavior of the low yield point steel BLY160: Experimental response and constitutive modeling. Int J Plast 2016;78:44–63. https://doi.org/10.1016/j.ijplas.2015.10.009.
- [128] S. Ganesh Sundara Raman KAP. Influence of martensite formation and grain size on room temperature low cycle fatigue behaviour of AISI 304LN austenitic stainless steel. Mater Sci Technol 2013:614–20. https://doi.org/10.1179/mst.1994.10.7.614.
- [129] Li Y. Fatigue crack initiation (in 304L steel): influence of the microstructure and variable amplitude loading. 2012.
- [130] Armas AF, Petersen C, Schmitt R, Avalos M, Alvarez-Armas I. Mechanical and microstructural behaviour of isothermally and thermally fatigued ferritic/martensitic steels. J Nucl Mater 2002;307:509–13. https://doi.org/10.1016/S0022-3115(02)01086-3.
- [131] Lebedev AA, Kosarchuk V V. Influence of phase transformations on the

- mechanical properties of austenitic stainless steels. Int J Plast 2000;16:749–67. https://doi.org/10.1016/S0749-6419(99)00085-6.
- [132] Pegues JW, Shao S, Shamsaei N, Schneider JA, Moser RD. Cyclic strain rate effect on martensitic transformation and fatigue behaviour of an austenitic stainless steel. Fatigue Fract Eng Mater Struct 2017;40:2080–91. https://doi.org/10.1111/ffe.12627.
- [133] Voce E. A practical strain-hardening function. Metallurgia 1955;51:219–26.
- [134] Taleb L, Cailletaud G. An updated version of the multimechanism model for cyclic plasticity. Int J Plast 2010;26:859–74. https://doi.org/10.1016/j.ijplas.2009.11.002.
- [135] Le Pécheur A, Curtit F, Clavel M, Stephan JM, Rey C, Bompard P. Thermomechanical FE model with memory effect for 304L austenitic stainless steel presenting microstructure gradient. Int J Fatigue 2012;45:106–15. https://doi.org/10.1016/j.ijfatigue.2012.05.016.
- [136] Li X, Sun Q, Zhang X. Identification of combined hardening model parameters by considering pre-tensile stress for 2024-T3 aluminum alloy. Mater Today Commun 2021;26:102065. https://doi.org/10.1016/j.mtcomm.2021.102065.
- [137] Weiping H, Chun H, Barter S. Analysis of cyclic mean stress relaxation and strain ratchetting behaviour of aluminium 7050. 1999.
- [138] Kyaw ST, Rouse JP, Lu J, Sun W. Determination of material parameters for a unified viscoplasticity-damage model for a P91 power plant steel. Int J Mech Sci 2016;115–116:168–79. https://doi.org/10.1016/j.ijmecsci.2016.06.014.
- [139] Teimouri R, Amini S, Guagliano M. Analytical modeling of ultrasonic surface burnishing process: Evaluation of residual stress field distribution and strip deflection. Mater Sci Eng A 2019;747:208–24. https://doi.org/10.1016/j.msea.2019.01.007.
- [140] Wang H, Yan Y, Wan M, Wu X. Experimental investigation and constitutive modeling for the hardening behavior of 5754O aluminum alloy sheet under two-stage loading. Int J Solids Struct 2012;49:3693–710. https://doi.org/10.1016/j.ijsolstr.2012.08.007.
- [141] Colin J, Fatemi A, Taheri S. Cyclic hardening and fatigue behavior of stainless steel 304L. J Mater Sci 2011;46:145–54. https://doi.org/10.1007/s10853-010-

- [142] Dey R, Tarafder S, Sivaprasad S. Influence of phase transformation due to temperature on cyclic plastic deformation in 304LN stainless steel. Int J Fatigue 2016;90:148–57. https://doi.org/10.1016/j.ijfatigue.2016.04.030.
- [143] Voyiadjis GZ, Abu Al-Rub RK. Thermodynamic based model for the evolution equation of the backstress in cyclic plasticity. Int J Plast 2003;19:2121–47. https://doi.org/10.1016/S0749-6419(03)00062-7.
- [144] Narendra PVR, Prasad K, Krishna EH, Kumar V, Singh KD. Low-Cycle-Fatigue (LCF) behavior and cyclic plasticity modeling of E250A mild steel. Structures 2019;20:594–606. https://doi.org/10.1016/j.istruc.2019.06.014.
- [145] Ohno N, Tsuda M, Kamei T. Elastoplastic implicit integration algorithm applicable to both plane stress and three-dimensional stress states. Finite Elem Anal Des 2013;66:1–11. https://doi.org/10.1016/j.finel.2012.11.001.
- [146] Mohanty Subhasish, Barua Bipul, Listwan Joseph, Majumdar Saurin NK. 3D-FE Modeling of 316 SS under Strain-Controlled Fatigue Loading and CFD Simulation of PWR Surge Line. No. ANL/LWRS-17/01. Argonne National Lab. (ANL), Argonne, IL (United States). 2017.
- [147] Basquin O. The exponential law of endurance tests. Am Soc Test Mater Proc 1910;10:625–30.
- [148] n LF Jr C. A study of the effect of cyclic thermal stresses in ductile metals. Trans ASME 1954;76:931–50.
- [149] JD. M. Cycle plastic strain energy and fatigue of metals. Intern Frict Damping, Cycl Plast ASTM Int 1965.
- [150] Scott-Emuakpor O, George T, Cross C, Shen MHH. Hysteresis-loop representation for strain energy calculation and fatigue assessment. J Strain Anal Eng Des 2010;45:275–82. https://doi.org/10.1243/03093247JSA602.
- [151] Lee KO, Hong SG, Lee SB. A new energy-based fatigue damage parameter in life prediction of high-temperature structural materials. Mater Sci Eng A 2008;496:471–7. https://doi.org/10.1016/j.msea.2008.07.035.
- [152] Chaboche J, Rousselier G. On the plastic and viscoplastic constitutive equations-Part 2: Application of Internal Variable Concepts to the 316 Stainless Steel. Trans

- ASME J Press Vessel Technol 1983;105:159-64.
- [153] Chaboche JL, Rousselier G. On the Plastic and Viscoplastic Constitutive Equations
 Part I: Rules Developed With Internal Variable Concept 1983:153–8.
- [154] McDowell DL. Stress state dependence of cyclic ratchetting behavior of two rail steels. Int J Plast 1995;11:397–421. https://doi.org/10.1016/S0749-6419(95)00005-4.
- [155] Kang G, Gao Q, Yang X. Uniaxial and non-proportionally multiaxial ratcheting of SS304 stainless steel at room temperature: Experiments and simulations. Int J Non Linear Mech 2004;39:843–57. https://doi.org/10.1016/S0020-7462(03)00060-X.
- [156] Ohno N, Kachi Y. A constitutive model of cyclic plasticity for nonlinear hardening materials. J Appl Mech Trans ASME 1986;53:395–403. https://doi.org/https://doi.org/10.1115/1.3171771.
- [157] OHNO N. Material models of cyclic plasticity with extended isotropic hardening: a review. Mech Eng Rev 2015;2:14-00425-14-00425. https://doi.org/10.1299/mer.14-00425.
- [158] Das P, Khutia N, Dey PP, Arora P, Gupta SK. Multi-objective cyclic plastic modelling of cyclic hardening and softening characteristics of nuclear piping SA333 gr. 6 carbon steel. Int J Fatigue 2024;180:108082. https://doi.org/10.1016/j.ijfatigue.2023.108082.
- [159] Mehani N, Roy SC. Modified isotropic and kinematic hardening equations for 304L SS under low cycle fatigue. Comput Mater Sci 2024;240:112999. https://doi.org/10.1016/j.commatsci.2024.112999.
- [160] Dahlberg M, Segle P. Evaluation Of Models For Cyclic Plasticity Deformation A Literature Study. Ebook 2010:62.
- [161] IAEA Report. Status of Fast Reactor Research and Technology Development. 2012.
- [162] Vaidyanathan G, Kale RD. India's nuclear power program: a critical review. Sadhana - Acad Proc Eng Sci 2022;47. https://doi.org/10.1007/s12046-022-01953-9.
- [163] Krovvidi SCSPK, Goyal S, Bhaduri AK. Low cycle fatigue and creep-fatigue response of the 316Ti stainless steel. Frat Ed Integrita Strutt 2019;13:577–84.

- https://doi.org/10.3221/IGF-ESIS.48.56.
- [164] Krovvidi SCSPK, Goyal S, Bhaduri AK. Experimental and Numerical Investigation of High-Temperature Low-Cycle Fatigue and Creep-Fatigue Life of Bellows. J Mater Eng Perform 2021;30:2742–50. https://doi.org/10.1007/s11665-021-05611-9.
- [165] Xie X, Jiang W, Chen J, Zhang X, Tu S. Cyclic hardening / softening behavior of 316L stainless steel at elevated temperature including strain-rate and strain-range dependence: Experimental and damage-coupled constitutive modeling. Int J Plast 2019;114:196–214. https://doi.org/10.1016/j.ijplas.2018.11.001.
- [166] Chetal SC, Chellapandi P. Indian fast reactor technology: Current status and future programme. Sadhana Acad Proc Eng Sci 2013;38:795–815. https://doi.org/10.1007/s12046-013-0167-8.
- [167] Li B, Yang J, Wang Z, Chen G, Chen X. Low cycle fatigue behavior of 316LN stainless steel: Effects of temperature, strain rate and strain amplitude. Int J Fatigue 2023;175:107767. https://doi.org/10.1016/j.ijfatigue.2023.107767.
- [168] Chen G, Li C, Xie M, Li B, Lin Q. Damage-coupled unified constitutive modeling of 316LN stainless steel including dynamic strain aging under various tension dwell time: A macroscopic phenomenological study. Int J Plast 2023;170:103764. https://doi.org/10.1016/j.ijplas.2023.103764.
- [169] Ortner S. A review of structural material requirements and choices for nuclear power plant. Front Nucl Eng 2023;2:1–11. https://doi.org/10.3389/fnuen.2023.1253974.
- [170] Hu C, Xu L, Zhao L, Han Y, Song K, Luo X, et al. Investigation of low cycle fatigue crack propagation behavior of 316H steel at 550°C based on cyclic response and damage accumulation: experiment and modelling. Int J Plast 2023;167. https://doi.org/10.1016/j.ijplas.2023.103661.
- [171] Chetal SC, Jayakumar T, Bhaduri AK. Materials research and opportunities in thermal (coal-based) power sector including advanced ultra super critical power plants. Proc Indian Natl Sci Acad 2015;81:739–54. https://doi.org/10.16943/ptinsa/2015/v81i4/48294.
- [172] Bhiogade DS. Ultra supercritical thermal power plant material advancements: A review. J Alloy Metall Syst 2023;3:100024.

- https://doi.org/10.1016/j.jalmes.2023.100024.
- [173] Armas AF, Bettin OR, Alvarez-Armas I, Rubiolo GH. Strain aging effects on the cyclic behavior of austenitic stainless steels. J Nucl Mater 1988;155–157:644–9. https://doi.org/10.1016/0022-3115(88)90388-1.
- [174] Zhong Y-L, Wang Y-B, Xiang Y, Li G-Q. Constitutive model for cyclic behavior of mild steel under various strain amplitudes. J Constr Steel Res 2022;196. https://doi.org/https://doi.org/10.1016/j.jcsr.2022.107396.
- [175] Zhou H, Zhang H, Bai F, Song M, Chen Y, Zhang L, et al. Planar dislocation structure during creep-fatigue interactions of TP347H heat-resistant austenitic steel at 600 °C. Mater Sci Eng A 2020;779:139141. https://doi.org/10.1016/j.msea.2020.139141.
- [176] Zhou HW, He YZ, Cen YW, Jiang JQ. Low-cycle fatigue behavior of TP347H austenitic stainless steels at room temperature. Adv Mater Res 2013;815:875–9. https://doi.org/10.4028/www.scientific.net/AMR.815.875.
- [177] Zhou H, He Y, Cui M, Cen Y, Jiang J. Dependence of dynamic strain ageing on strain amplitudes during the low-cycle fatigue of TP347H austenitic stainless steel at 550 C. Int J Fatigue 2013;56:1–7. https://doi.org/10.1016/j.ijfatigue.2013.07.010.
- [178] Sivaprasad S, Paul SK, Tarafder S, Gupta SK, Bhasin V. Cyclic Plastic Deformation Behaviour of Pht Piping Materials an Experimental Investigation 2011:6–11.
- [179] Guguloth K, Sivaprasad S, Chakrabarti D, Tarafder S. Low-cyclic fatigue behavior of modified 9Cr-1Mo steel at elevated temperature. Mater Sci Eng A 2014;604:196–206. https://doi.org/10.1016/j.msea.2014.02.076.
- [180] Government of India, Department of Atomic Energy, Indira Gandhi Centre for Atomic Research, Kalpakkam, 60310 I. Fast Breeder Test Reactor. n.d.
- [181] Government of India, Department of Atomic Energy, Indira Gandhi Centre for Atomic Research, Kalpakkam-603102 I. Annual Report-2022. 2022.
- [182] Dutta A, Company DC. Material characterization of SS 316 in low-cycle fatigue loading Material characterization of SS 316 in low-cycle fatigue loading 2010. https://doi.org/10.1007/s10853-009-4155-7.

- [183] Hormozi R. Experimental and Numerical Simulations of Type 316 Stainless Steel Failure under LCF / TMF Loading Conditions. Imperial College London, 2014.
- [184] Sivaprasad S, Paul SK, Das A, Narasaiah N, Tarafder S. Cyclic plastic behaviour of primary heat transport piping materials: Influence of loading schemes on hysteresis loop. Mater Sci Eng A 2010;527:6858–69. https://doi.org/10.1016/j.msea.2010.07.041.
- [185] Khutia N, Dey PP, Sivaprasad S, Tarafder S. Development of new cyclic plasticity model for 304LN stainless steel through simulation and experimental investigation. Mech Mater 2014;78:85–101. https://doi.org/10.1016/j.mechmat.2014.07.019.
- [186] Purgert R, Phillips J, Hendrix H, Shingledecker J, Tanzosh J. Materials for Advanced Ultra-supercritical (A-USC) Steam Turbines-A-USC Component Demonstration Pre-FEED Final Technical Report 2016:79.
- [187] Marquis D. Etude théorique et vérification expérimentale d'un modèle de plasticité cyclique. Thèse de 3ème Cycle, Université Pierre et Marie Curie, Paris 6. 1979.
- [188] Liang F, Zhang W, Chen F, Yin P, Yang Q, Chang L, et al. Experimental and constitutive modelling studies of type 316L stainless steel based on internal stress under low cycle fatigue and creep-fatigue interaction. Int J Fatigue 2023;175. https://doi.org/10.1016/j.ijfatigue.2023.107835.
- [189] Ellyin F, Kujawski D. Plastic strain energy in fatigue failure. J Press Vessel Technol Trans ASME 1984;106:342–7. https://doi.org/10.1115/1.3264362.
- [190] Xu X, Wang Z, Zhang X, Gao G, Wang P, Kan Q. Strain amplitude-dependent cyclic softening behavior of carbide-free bainitic rail steel: Experiments and modeling. Int J Fatigue 2022;161:106922. https://doi.org/10.1016/j.ijfatigue.2022.106922.
- [191] Chetal SC, Jayakumar T, Bhaduri AK. Materials research and opportunities in thermal (coal-based) power sector including advanced ultra super critical power plants. Proc Indian Natl Sci Acad 2015;81:739–54. https://doi.org/10.16943/ptinsa/2015/v81i4/48294.
- [192] Power A, Gmbh S, Strasse A, Asia E. Advanced Ultra-Supercritical Steam Power Plants 2014.
- [193] Ravinder Reddy P, Kumar Reddy D, Professor A. Advance Power Plant

- Technologies and Steam Cycle for Super Critical Application. Int J Sci Res Publ 2012;2:2250–3153.
- [194] Wright I, Maziasz P. Materials issues for turbines for operation in ultrasupercritical steam. ... Res Mater ... 2004.
- [195] Schaffel-Mancini N, Mancini M, Szlek A, Weber R. Novel conceptual design of a supercritical pulverized coal boiler utilizing high temperature air combustion (HTAC) technology. Energy 2010;35:2752–60. https://doi.org/10.1016/j.energy.2010.02.014.
- [196] Rodriguez P, Mannan SL. High temperature low cycle fatigue. Sadhana 1995;20:123–64. https://doi.org/10.1007/BF02747287.
- [197] Alsmadi ZY, Alomari A, Kumar N, Murty KL. Effect of hold time on high temperature creep-fatigue behavior of Fe–25Ni–20Cr (wt.%) austenitic stainless steel (Alloy 709). Mater Sci Eng A 2020;771:138591. https://doi.org/10.1016/j.msea.2019.138591.
- [198] Tang Z, Jing H, Xu L, Chi D, Zhao L, Han Y, et al. Crack growth behavior, fracture mechanism, and microstructural evolution of G115 steel under creep–fatigue loading conditions. Int J Mech Sci 2019;161–162. https://doi.org/10.1016/j.ijmecsci.2019.105037.
- [199] Wang Q, Yu J, Li B, Li Y, Wang K, Chen X. Mechanisms of deformation, damage and life behavior of inconel 617 alloy during creep-fatigue interaction at 700 °C. Int J Fatigue 2025;190:108635. https://doi.org/10.1016/j.ijfatigue.2024.108635.
- [200] Xiang S, Jonsson S, Babu RP, Zhu B, Odqvist J. Materials Science & Engineering A Influence of tension and compression dwell on the creep-fatigue properties of the austenitic cast iron Ni-resist D5S 2021;814.
- [201] Wang RZ, Cheng LY, Zhu SP, Zhao PC, Miura H, Zhang XC, et al. Semi-quantitative creep-fatigue damage analysis based on diffraction-based misorientation mapping and the correlation to macroscopic damage evolutions. Int J Fatigue 2021;149:106227. https://doi.org/10.1016/j.ijfatigue.2021.106227.
- [202] Zhao L, Xu L, Han Y, Jing H. Analysis on stress-strain behavior and life prediction of P92 steel under creep-fatigue interaction conditions. Fatigue Fract Eng Mater Struct 2020;43:2731–43. https://doi.org/10.1111/ffe.13341.

- [203] Song K, Xu L, Zhao L, Han Y, Ma N, Wang K, et al. Effect of loading modes on uniaxial creep-fatigue deformation: A dislocation based viscoplastic constitutive model. Int J Plast 2024;179:104038. https://doi.org/10.1016/j.ijplas.2024.104038.
- [204] Zhang T, Wang X, Ji Y, Tang J, Jiang Y, Zhang X, et al. Cyclic deformation and damage mechanisms of 9%Cr steel under hybrid stress-strain controlled creep fatigue interaction loadings. Int J Fatigue 2021;151:106357. https://doi.org/10.1016/j.ijfatigue.2021.106357.
- [205] Zhang T, Wang X, Ji Y, Zhang W, Hassan T, Gong J. P92 steel creep-fatigue interaction responses under hybrid stress-strain controlled loading and a life prediction model. Int J Fatigue 2020;140:105837. https://doi.org/10.1016/j.ijfatigue.2020.105837.
- [206] Bhanu Sankara Rao K, Meurer HP, Schuster H. Creep-fatigue interaction of inconel 617 at 950°C in simulated nuclear reactor helium. Mater Sci Eng 1988;104:37–51. https://doi.org/10.1016/0025-5416(88)90404-1.
- [207] Srinivasan VS., Nagesha A., Valsan M., Bhanu shankara ao K., Mannan SL., Sastry DH. Effect of hold-time on low cycle fatigue behaviour of nitrogen bearing 316L stainless steel. Int J Press Vessel Pip 1999;76:863–70. https://doi.org/https://doi.org/10.1016/S0308-0161(99)00023-X.
- [208] Cabet C, Carroll L, Madland R, Wright R. Creep-Fatigue of High Temperature Materials for VHTR: Effect of Cyclic Loading and Environment. Proc ICAPP 2011:312.
- [209] Oxidation, Creep and Fatigue Synergies in Cast Materials for Exhaust Manifolds Oxidation, Creep and Fatigue Synergies in Cast Materials for Exhaust Manifolds. 2021.
- [210] Dewa RT, Park JH, Kim SJ, Lee SY. High-temperature creep-fatigue behavior of alloy 617. Metals (Basel) 2018;8. https://doi.org/10.3390/met8020103.
- [211] Zhu S-P, Yang Y-J, Huang H-Z, Zhiqiang L, Wang H-K. A unified criterion for fatigue-creep life prediction of high temperature components. Proc. Inst. Mech. Eng. Part G J. Aerosp. Eng. ,231(4), n.d. https://doi.org/10.1177/0954410016641448.
- [212] Zhu SP, Lei Q, Huang HZ, Yang YJ, Peng W. Mean stress effect correction in strain energy-based fatigue life prediction of metals. Int J Damage Mech

- 2017;26:1219-41. https://doi.org/10.1177/1056789516651920.
- [213] Coffin LF. Fatigue At High Temperature. Adv Res Strength Fract Mater 1978;1:263–92. https://doi.org/https://doi.org/10.1016/B978-0-08-022136-6.50029-9.
- [214] Agatonovic BYP. DAMAGING PROCESS IN CREEP-FATIGUE-OXIDATION ENVIRONMENT AND n.d.
- [215] Conway JB, Stentz RH, Berling JT. Fatigue, Tensile, and Relaxation behavior of stainless steels. 1975.
- [216] Ogawa F, Nakayama Y, Hiyoshi N, Hashidate R, Wakai T, Itoh T. The Multiaxial Creep–Fatigue Failure Mechanism of Mod. 9Cr-1Mo Steel Under Non-proportional Loading: Effect of Strain Energy on Failure Lives. Trans Indian Natl Acad Eng 2022;7:549–64. https://doi.org/10.1007/s41403-021-00279-y.
- [217] Zhang T, Wang X, Zhou D, Wang R, Jiang Y, Zhang X, et al. A universal constitutive model for hybrid stress-strain controlled creep-fatigue deformation. Int J Mech Sci 2022;225:107369. https://doi.org/10.1016/j.ijmecsci.2022.107369.
- [218] Halford GR. The Energy Required for Fatigue (Plastic Strain Hystersis Energy Required for Fatigue in Ferrous and Nonferrous Metals). J Mater 1966;1:3–18.
- [219] Skeleton RP. Energy criterion for high temperature low cycle fatigue failure. J Mater Sci Technol 1991;7:421–39.
- [220] Ellyin F, Kujawski D. Plastic Strain Energy in Fatigue Failure. J Press Vessel Technol 1984;106(4):342–7. https://doi.org/https://doi.org/10. 1115/1.3264362.
- [221] Tung HM, Stubbins JF. Incipient oxidation kinetics of alloy 617 and residual stress of the oxide scale formed in air at temperatures between 850 and 1000°C. J Nucl Mater 2012;424:23–8. https://doi.org/10.1016/j.jnucmat.2012.01.015.
- [222] Al-Hatab KA, Al-Bukhaiti MA, Krupp U. Cyclic oxidation kinetics and oxide scale morphologies developed on alloy 617. Appl Surf Sci 2014;318:275–9. https://doi.org/10.1016/j.apsusc.2014.04.199.
- [223] Gordon AP, Trexler MD, Neu RW, Sanders TJ, McDowell DL. Corrosion kinetics of a directionally solidified Ni-base superalloy. Acta Mater 2007;55:3375–85. https://doi.org/10.1016/j.actamat.2007.01.034.
- [224] Salari S, Rahman MS, Polycarpou AA, Beheshti A. Elevated temperature

- mechanical properties of Inconel 617 surface oxide using nanoindentation. Mater Sci Eng A 2020;788. https://doi.org/10.1016/j.msea.2020.139539.
- [225] Fournier B. FATIGUE-FLUAGE DES ACIERS MARTENSITIQUES A 9-12%Cr: COMPORTEMENT ET ENDOMMAGEMENT. Mines Paris Tech, 2007.
- [226] Sohrabi MJ, Naghizadeh M, Mirzadeh H. Deformation-induced martensite in austenitic stainless steels: A review. Arch Civ Mech Eng 2020;20:1–24. https://doi.org/10.1007/s43452-020-00130-1.
- [227] Wang Z, Liu J, Huang F, Bi YJ, Zhang SQ. Hydrogen Diffusion and Its Effect on Hydrogen Embrittlement in DP Steels With Different Martensite Content. Front Mater 2020;7:1–12. https://doi.org/10.3389/fmats.2020.620000.
- [228] Hu X, Koyanagi T, Fukuda M, Kumar NAPK, Snead LL, Wirth BD, et al. Irradiation hardening of pure tungsten exposed to neutron irradiation. J Nucl Mater 2016;480:235–43. https://doi.org/10.1016/j.jnucmat.2016.08.024.
- [229] Zheng Y, Shirani Bidabadi MH, Wang G, Zhang C, Chen H, Yang Z. Coordination of Pre-oxidation Time and Temperature for a Better Corrosion Resistance to CO 2 at 550 °C. Oxid Met 2019;91:657–75. https://doi.org/10.1007/s11085-019-09901-5.
- [230] Tung HM, Stubbins JF. Incipient oxidation kinetics and residual stress of the oxide scale grown on Haynes 230 at high temperatures. Mater Sci Eng A 2012;538:1–6. https://doi.org/10.1016/j.msea.2011.10.114.
- [231] Costa GCC, Jacobson NS, Lukco D, Hunter GW, Nakley L, Radoman-Shaw BG, et al. Oxidation behavior of stainless steels 304 and 316 under the Venus atmospheric surface conditions. Corros Sci 2018;132:260–71. https://doi.org/10.1016/j.corsci.2018.01.002.
- [232] Arnold K. High Temperature Oxidation Behaviour of Nickel-Base Superalloys 2016:295.
- [233] Chen X, Yang Z, Sokolov MA, Erdman DL, Mo K, Stubbins JF. Effect of creep and oxidation on reduced fatigue life of Ni-based alloy 617 at 850 °c. J Nucl Mater 2014;444:393–403. https://doi.org/10.1016/j.jnucmat.2013.09.030.
- [234] Zhao J, Qiu F, Xu C. Review of Creep-Thermomechanical Fatigue Behavior of Austenitic Stainless Steel. Crystals 2023;13.

- https://doi.org/10.3390/cryst13010070.
- [235] Fournier B, Sauzay M, Caës C, Noblecourt M, Mottot M, Bougault A, et al. Creepfatigue-oxidation interactions in a 9Cr-1Mo martensitic steel. Part I: Effect of tensile holding period on fatigue lifetime. Int J Fatigue 2008;30:649–62. https://doi.org/10.1016/j.ijfatigue.2007.05.007.
- [236] Kang G. Ratchetting: Recent progresses in phenomenon observation, constitutive modeling and application. Int J Fatigue 2008;30:1448–72. https://doi.org/10.1016/j.ijfatigue.2007.10.002.
- [237] Malinin NN, Khadjinsky GM. Theory of creep with anisotropic hardening. Int J Mech Sci 1972;14:235–46. https://doi.org/10.1016/0020-7403(72)90065-3.
- [238] Yaguchi M, Yamamoto M, Ogata T. A viscoplastic constitutive model for nickel-base superalloy, part 1: Kinematic hardening rule of anisotropic dynamic recovery. Int J Plast 2002;18:1083–109. https://doi.org/10.1016/S0749-6419(01)00029-8.
- [239] Barrett RA, O'Donoghue PE, Leen SB. An improved unified viscoplastic constitutive model for strain-rate sensitivity in high temperature fatigue. Int J Fatigue 2013;48:192–204. https://doi.org/10.1016/j.ijfatigue.2012.11.001.
- [240] Chen W, Kitamura T, Feng M. Creep and fatigue behavior of 316L stainless steel at room temperature: Experiments and a revisit of a uni fi ed viscoplasticity model. Int J Fatigue 2018;112:70–7. https://doi.org/10.1016/j.ijfatigue.2018.03.010.
- [241] Goswami T. Low cycle fatigue—dwell effects and damage mechanisms 1 1999;21:55–76.
- [242] Li B, Zheng Y, Shi S, Liu Y, Li Y, Chen X. Microcrack initiation mechanisms of 316LN austenitic stainless steel under in-phase thermomechanical fatigue loading. Mater Sci Eng A 2019;752:1–14. https://doi.org/10.1016/j.msea.2019.02.077.
- [243] Zhao J, Li B, Zheng Y, Azadi M, Chen X. Cyclic Deformation Behavior and Failure Mechanism of 316LN Stainless Steel under Creep-Fatigue Loading at 550
 C. J Mater Eng Perform 2022;31:8314–26. https://doi.org/10.1007/s11665-022-06859-5.
- [244] Wareing J. Creep-fatigue behaviour of four casts of Type 316 stainless steel. 1981;4:131–45.
- [245] Holdsworth S. Creep-fatigue failure diagnosis. Materials (Basel) 2015;8:7757–69.

- https://doi.org/10.3390/ma8115418.
- [246] Levaillant C, Grattier J, Mottot M, Pineau A. Creep and creep-fatigue intergranular damage in austenitic stainless steels: discussion of the creep-dominated regime. Low cycle fatigue. ASTM Int., 1988.
- [247] Xiao Q, Wang X, Chen D, Zhou X, Liu X, Yang W. A new nonlinear fatigue cumulative damage model based on load interaction and strength degradation. Int J Fatigue 2025;191:108709. https://doi.org/10.1016/j.ijfatigue.2024.108709.
- [248] Liu D, Pons DJ, Wong E. The Unified Creep-Fatigue Equation for Stainless 2016:1–18. https://doi.org/10.3390/met6090219.
- [249] Hectors K. Cumulative Damage and Life Prediction Models for High-Cycle Fatigue of Metals: A Review 2021:1–32.
- [250] Aeran A, Siriwardane SC, Mikkelsen O, Langen I. A new nonlinear fatigue damage model based only on S-N curve parameters. Int J Fatigue 2017;103:327–41. https://doi.org/10.1016/j.ijfatigue.2017.06.017.
- [251] Sun L, Liu L, Wang R, Wang X, Tan J, Guo S, et al. A modified damage-coupled viscoplastic constitutive model for capturing the asymmetric behavior of a nickel-based superalloy under wide creep-fatigue loadings. Int J Fatigue 2022;164:107160. https://doi.org/10.1016/j.ijfatigue.2022.107160.
- [252] Perera R, Gómez S, Alarcón E. A fatigue damage model for seismic response of RC structures. Comput Struct 2000:293–302.
- [253] Xie XF, Jiang W, Chen J, Zhang X, Tu ST. Cyclic hardening/softening behavior of 316L stainless steel at elevated temperature including strain-rate and strain-range dependence: Experimental and damage-coupled constitutive modeling. Int J Plast 2019;114:196–214. https://doi.org/10.1016/j.ijplas.2018.11.001.